



Charles University in Prague, Faculty of Science

Institute of Hydrogeology, Engineering Geology and Applied Geophysics

Jan Valenta

# **New approaches in high-resolution shallow seismic prospection**

submitted for the degree of Philosophiae Doctor

Supervisor: RNDr., PhDr. Jiří Dohnal

Consultant: RNDr. Jiří Málek, PhD.

Prague, 11th October 2007



This dissertation describes my original work except where acknowledgement is made in the text. It is not substantially the same as any work that has been, or is being submitted to any other university for any degree, diploma or any other qualification.

Jan Valenta  
11th October 2007





MEPHISTOPHELES: Gray, my friend, is every theory,  
and green alone life's golden tree.

*Johann Wolfgang von Goethe, Faust*





---

## Summary

This work deals with the application of seismic methods in high-resolution near-surface prospection. Two topics are covered in this text. The first one describes processing and application of 3D shallow seismic refraction, while the second one deals with possible methods of identification and filtration of S-waves.

The processing of the 3D seismic refraction data is currently carried out mainly by means of the seismic tomography. Because the tomography method usually works with the gradient model of the subsurface, an approach to the layer-based model was sought. The solution was found in a modification of the time-term method. The time-term method was modified to handle also the lateral variations of velocity in highly heterogeneous media. REFRACT3D computer program for data processing using the time-term method was developed. The modified time-term method was successfully tested during the archaeological prospection of the Děvín Castle and during the prospection of the shallow subsurface of the Ostaš seismic station. The results from the time-term method were compared with the results obtained by the first arrival travel time tomography. In the case of the Děvín Castle the time-term results surpass the tomography one, while at the locality of Ostaš the tomography results are better.

The imaging of subsurface using the S-waves is a very good supplement to the conventional P-wave surveys. However, problems with the identification of S-wave onsets and S-wave wave forms make it a very demanding task. Usually, a special S-wave source is needed for the S-wave survey. Unfortunately, the S-waves sources suffers from a very low generated energy or are heavy, clumsy and expensive. Even though conventional P-wave sources also produce sufficient amount of S-waves, their usage in S-wave prospection is limited due to the problems with onset identification. In this work two methods of S-wave identification are presented. The first one is a modification, or elaboration, of the classical method – polarity reversals. It was modified in such a way, that it enables separation of SH and SV waves. The second method tries to identify S-waves according to the similarity of waveforms on the neighbouring records and thus can use also the simple P-wave sources, like sledgehammer. The latter one was used in the prospection of the subsurface of the Nečtiny seismic station and its results are presented in this text.





---

# Foreword

This text is intended as a contribution to the widely developed area of the near-surface geophysics. Because the near-surface geophysics is a very broad discipline, involving assortment of different methods and processing procedures, only a small part of the methods used in shallow seismic is presented here.

From the wide range of geophysical methods the seismic methods were selected because they represent broad spectra of highly elaborated methods very powerful in imaging of the subsurface and hence solving a wide range of different applications.

This work is focused on two particular problems of seismic prospection in the near-surface applications. The first one is the high-resolution 3D prospection of sites with abrupt lateral velocity changes, which is often the case of archaeological localities. The second main topic is the prospection using S-waves, where two methods of S-wave identification are described and elaborated.

The 3D seismic prospection is a method capable of producing very detailed and complex image of the subsurface. Currently, most of the 3D data processing is done by means of seismic tomography. Unfortunately, the tomography, as every method, has its limitations. The inversion in tomography is a highly non-linear process. To obtain reasonable results, the smoothest possible model is sought, which needs damping and smoothing. Otherwise we can arrive at a situation with extremely high velocities in some parts of the model compensated by very low, or even negative, values of velocities in other parts of the model to compensate the high ones (effect of inversion of an ill-conditioned matrix). The smoothing is fine when looking for large-scale geological bodies but represents a real limitation in high-resolution applications, such as archaeological prospection.

Another drawback of the tomography might be the often used gradient model of the subsurface. The advantage of the gradient model is that it can describe any particular structure, but when the edges of the structure are sharp, then this description lacks precision. An example of such a case is the layer boundary. If we are to find the depth of the boundary, we will run into problems when using the gradient model, because the boundary might be placed somewhere into a range of the gradient. And although the tomography codes enabling joint inversion of layer boundaries and velocities do exist, their application is not without problems. Moreover, for example, some archaeological features like buried walls and moats are often more easily identified as changes in the refractor depths than changes in velocities.

Therefore, another method of data processing was sought. This method should resolve the depth of layer boundaries and lateral changes of velocities. Furthermore,

the inversion procedure should be straightforward and simple, preferably linear, to produce an image with the highest possible resolution. These criteria were met in the time-term method (Scheidegger and Willmore, 1957), which was modified to handle also the lateral variations of velocities in highly heterogeneous media (see Section 1.4). The REFRACT3D computer program, based on the modified time-term method, was written to compute a layer-based model from the first arrival travel times (Chapter 5).

The modified time-term method was applied to 3D data set from archaeological survey at the Děvín Castle (Chapter 2). The results of the time-term method are compared with the results of the seismic tomography, and the time-term results surpass the tomography ones. Another application of the time-term method described here comes from the locality of Ostaš (Chapter 3) where, in contrast, the tomography yielded better results.

The shallow seismic prospecting is most often carried out using the P-waves as “illuminating” rays. It is sufficient for many cases but sometimes other information is also necessary. In hydrogeology, for instance, porosity and fracturing of rocks play the key role. In geotechnics, the stress state of the rock is of vital interest. The Lamé parameters  $\mu$  and  $\lambda$  (or the  $E$  and  $\sigma$  parameters) are used when evaluating bedrock state for constructions. For these applications, the classical P-wave velocity model has to be extended to the PS-waves model. Unfortunately, problems with reliable identification of S-wave onsets keep S-waves away from routine prospecting.

Over the years, many different techniques for S-wave identification were developed. They are based either on special sources for S-wave generation, or on post processing data from conventional sources. None of these methods is perfect, as illustrated by the increasing popularity of S-wave velocity profile determinations from surface waves (SASW, MASW). However, even the determination from surface waves has its own problems and thus this work presents two more methods for the identification of S-wave onsets (Chapter 4).

The first method is a traditional method of polarity reversals – reversals of polarity of S-waves with reversals of direction of the source. This method has been further elaborated to differentiate also the SV- and SH-waves.

The second method is based on comparing records from neighbouring geophones on the profile and tries to filter the waves based on the similarity in their waveforms. This method is illustrated on the field example from the Nečtiny seismic station.

And at the end of the foreword, it is my pleasure to thank all, who helped with this work and this text. I especially wish to thank my supervisor Jiří Dohnal and my consultant Jiří Málek. Then, I thank Zdeněk Jáně and my co-workers from the Institute of Rock Structure and Mechanics, Academy of Sciences of the Czech Republic, who enabled all the field work. Then, I express my thanks to Roman Živor from the Institute of Geology, Academy of Sciences of the Czech Republic, for ultrasonic laboratory measurements of samples. Many thanks to Isaac Flecha and David Martí from the Institut de Ciències de la Terra “Jaume Almera”, CSIC, for introduction into the overwhelming world of seismic tomography. Many thanks to Marie Prcinová, the librarian, for her help with my hunt for information. And many thanks to Jiří Adamovič from the Institute of Geology, Academy of Sciences of the Czech Republic and to Lucie Medová, for their help with the English version of this manuscript.

---

# Processing and interpretation of shallow seismic refraction data

The seismic exploration methods can be divided into number of groups based on the type of waves used for the measurements. The main wave types used for research are the reflected and refracted waves (either the P- and S-waves) and in the last few decades also the surface waves.

Probably the most widely used group of methods are those utilising reflected waves, and the whole petroleum industry is heavily dependent on seismic reflection prospecting. The seismic reflection method brings a relatively high-resolution image of the subsurface with low lateral range. The main target of the seismic reflection method is to resolve the reflecting interfaces, which are the key components for consequent interpretation process.

The refraction method, on the other hand, comes with a broader spatial range and lower resolution than the reflection one. This determines the refraction method for use in the research of deep parts of crust and mantle on long transcontinental profiles. As a kind of supplement to these global measurements, very small-scale research is being conducted in the upper-most part of the soil and rock media under the surface. The refraction method provides interpreters with distribution of velocities of seismic waves in the geological environment, as opposed to interfaces of the reflection method.

The oldest extensive usage of seismic refraction was the *fan-shooting*. The geophones were distributed along a fan in different directions from the source. Travel times were recorded only by few geophones (usually not more than six) and seismic wave velocities were simply computed from the travel times and source–geophone distances. The apparent seismic wave velocities obtained from individual geophones were compared, and differences were interpreted as a changes in depth of seismic interface. This type of measurement was common in early stages of seismic prospecting and ended after World War II, when it was replaced with profile measurements.

*Profile measurements* usually employ a higher number of geophones (dozens) and sources. For the computation of velocities, differences between travel times from opposite sources might be used, thus eliminating the effects of inclined interfaces. Currently, the profile measurement mode is the most common one in the routine seismic prospection.

With the growing capabilities of computers, the exploration techniques took another step further, and first the *slalom line* – a 2.5D measurements and finally the *3D measurements* were developed.

The evolution, however, did not stop at the three-dimension prospection. Currently also the 4D measurements are carried out. It is essentially a 3D prospection, where

the fourth component is the time. It means that this type of prospection is looking for changes of geological environment in time. It is used mainly in the petroleum industry for monitoring the oil deposits. However some attempts to apply it to hydrogeology have been also made. The 4D prospection is also used for waste disposal sites leakage monitoring, only the seismic methods are replaced with geoelectrical ones, mainly with the ground penetrating radar.

As the time passed, many more or less sophisticated techniques of data processing of profile measurements were developed. They can be divided into four main groups depending on the wave type and geological model they use.

The oldest group employed *layered earth model* and head waves. This is the easiest type of processing. The layer-based model consists of an arbitrary number of layers with different velocities. The velocities in individual layers may be constant or vary in lateral direction. Methods from this group were used from the beginnings of the seismic refraction. There is a wide assortment of these methods described in textbooks, and their complexity vary on the order of a magnitude, however, most of these methods could be realised without a computer only with a pen, paper and a calculator (or graphically). The simplest methods, for example the ABC method (Sheriff and Geldart, 1995), are not commonly used nowadays as they can handle only a limited subset of information contained in the measured dataset. More elaborated methods, for example, the reciprocal methods, can in some incarnations handle also the gradient of velocities in individual layers. And some methods of this group can be easily used in three dimensions, for example, the time-term method.

The second group is characterised by the *earth model with a gradient of velocity* where the velocities may change smoothly in the lateral and vertical directions, often without sharp interfaces, and is employs turning rays. This group is represented by the seismic tomography, currently one of the most widely used techniques in seismic refraction. The seismic tomography method is also well suited for the processing of three-dimensional data.

Then, there is a group of intermediate methods, mixing both types of models and all ray types, capable of simultaneous inversion of seismic velocities and layer interfaces. Modifications of seismic tomography represent the methods in this group.

And, finally, the most sophisticated technique, the Holy Grail and a golden calf, which still has not been satisfactorily implemented, is the full waveform inversion. This method, when successfully implemented, should handle a mix of arbitrary distribution of velocities and layer interfaces well determined by the whole amount of recorded data.

In this chapter, we will go briefly through selected commonly used data processing methods used in seismic refraction (reciprocal methods and seismic tomography). It is meant to be a brief overview, we will not derive equations as these can be found in seismic processing textbooks. And in the last section of this chapter we will discuss the time-term method, and modify it to handle lateral changes of velocities. But first, we ought to make a step aside and mention a ray approximation and the 1<sup>st</sup> Fresnel zone.

*The wavelength of several metres is encountered in the near-surface geophysics, where (relatively) high-frequency waves are used. In contrast, the global seismology works also with low frequency waves with periods of several minutes, where the wavelength is on the order of hundreds of kilometres.*

## 1.1 The ray approximation and the Fresnel zone

Many of seismic processing methods (e.g. the tomography method) use a ray approximation (or, better, the zero-order approximation of the ray theory) of propagation of the seismic energy. This means that the seismic wave is considered to have an infinite frequency and can be therefore described using the laws of the ray optics. In the real world, the seismic waves usually have relatively low frequencies (on the orders of tens or ones of Hz, or even less), and the wavelength becomes a parameter which should be taken into consideration. As the wavelength is several metres, it may limit the resolution of subtle near-surface features. This fact is not of such importance in



refraction surveys as in the seismic reflection, where the frequency limitations are more obvious. The ray must be considered to be of some thickness – a region surrounding the ray path, which is sampled by the ray – the 1<sup>st</sup> Fresnel zone. The radius  $F_r$  of the 1<sup>st</sup> Fresnel zone is:

$$F_r = \sqrt{\frac{\lambda d_1 d_2}{d_1 + d_2}}, \quad (1.1)$$

where  $F_r$  is the radius of the 1<sup>st</sup> Fresnel zone in metres,  $\lambda$  is the wavelength of the ray and  $d_1$  and  $d_2$  are the distances from one end and from the other end respectively. In case of homogeneous media the 1<sup>st</sup> Fresnel zone forms an ellipsoid around the source and receiver with the maximum diameter half-way between the source and the receiver. The wavelength of the seismic wave can be easily obtained from its frequency and velocity of propagation:

$$\lambda = \frac{v}{f}, \quad (1.2)$$

where  $v$  is the velocity of seismic wave and  $f$  is its frequency.

The question is, how large part of the 1<sup>st</sup> Fresnel zone should be considered significantly influenced by the media. The Fresnel zone is traditionally used in the reflection seismics to determine the horizontal resolution of the seismic waves. The 1<sup>st</sup> Fresnel zone is considered to be the smallest zone, that can be resolved. Or, in other words, inhomogeneity smaller than the 1<sup>st</sup> Fresnel zone can not be detected. And consequently, the inhomogeneities located besides the seismic ray path have also *some* amount of influence on the seismic wave. The problem lies in the determination of the *some* – how far from the ray must the inhomogeneity be to consider its effect negligible? How large part of the Fresnel zone has a substantial effect on the whole seismic ray? Many attempts have been done in order to illustrate the influence of the Fresnel zone (e.g. Sheriff, 1996; Thore and Juliard, 1999; Yoshizawa and Kennett, 2002) but it is difficult to estimate it precisely. For example, the Yoshizawa and Kennett (2002) defined the width of the influenced zone as an area where the phase change of the (Rayleigh) wave is less than 10 %. They showed that this area is about one-third of the 1<sup>st</sup> Fresnel zone. We will adopt this estimate and consider it to be valid also for the body waves.

## 1.2 Layer-based methods of seismic refraction data processing

In this section we will go through the two often used processing techniques using the layered model – the reciprocal methods.

All the simple layer-interpreting techniques are derived from the equation of a head wave in a layer over a half-space:

$$t = \frac{2h \cos \theta}{v_0} + \frac{x \sin(\theta + \varphi)}{v_0}, \quad (1.3)$$

where  $t$  is the travel-time,  $h$  is the depth to the bottom layer,  $\theta$  is the critical angle,  $x$  is the offset,  $\varphi$  is the dip of the refracting boundary,  $v_0$  is the velocity of the upper layer. The background theory and derivation of this equation can be found e.g. in Sheriff and Geldart (1995), Palmer (1980) and others. It is usually assumed, that the dip of the boundary is negligible (less than 10°) and the

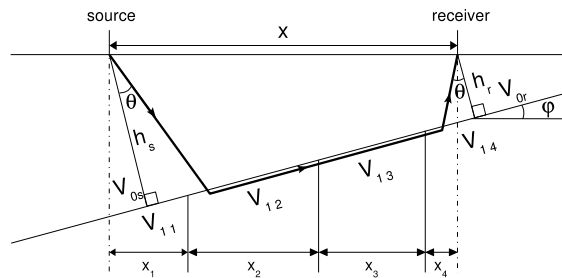


Figure 1.1: A ray path along a dipping refractor. See the text for explanation.

According to the ray theory, there are no head waves on the seismograms. The zero-order approximation of the ray theory does not know anything about the head waves. The head waves appear in the first approximation. However, waves in the first approximation are attenuated exponentially and thus should be undetectable. In other words, the ray theory suggests us, that we are not using head waves but rather refracted waves. Anyway, the head wave proved to be a good approximation of the real wave travelling along the interface – reasonably accurate and with a simple mathematical representation. Thus we will adopt it for further discussion without any consideration about its essence.

$\varphi$  term is omitted. The equation then simplifies:

$$t = \frac{2h \cos \theta}{v_0} + \frac{x}{v_1}, \quad (1.4)$$

where  $v_1$  is the velocity in the bottom layer. When the depth beneath the source and receiver differs, then the term containing the depth splits into source and receiver parts:

$$t = \frac{h_s \cos \theta}{v_0} + \frac{h_r \cos \theta}{v_0} + \frac{x}{v_1}, \quad (1.5)$$

where the  $h_s$  and  $h_r$  are the depths beneath the source and the receiver, respectively.

These equations assume that the velocities are constant in individual layers. However, this condition is hardly ever encountered in a real media. Therefore we should rather count for velocity changes. We divide layers into  $n$  cells where the velocities can be considered constant with the desired precision. A modified equation is then:

$$t = \frac{h_s \cos \theta}{v_{0s}} + \frac{h_r \cos \theta}{v_{0r}} + \sum_{i=1}^n \frac{x_i}{v_{1i}}, \quad (1.6)$$

where the  $v_{0s}$  and  $v_{0r}$  denote velocities in the upper layer beneath the source and the receiver, respectively,  $x_i$  is a length of a path of refracted wave in a cell with a constant velocity  $v_i$ . The sum of all lengths  $x_i$  gives the total length of the raypath along the refracting boundary  $x$  (see Fig. 1.1). The problem of raypaths are further discussed in Section 1.4.1.

### 1.2.1 Reciprocal methods

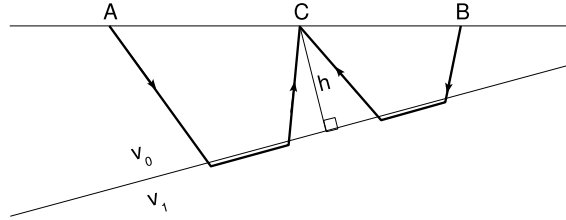


Figure 1.2: Reciprocal raypaths in the Hagedoorn's plus-minus method. Sources are at points A and B, normal depth ( $h_s$ ) and velocity of the refractor ( $v_1$ ) are determined for point C.

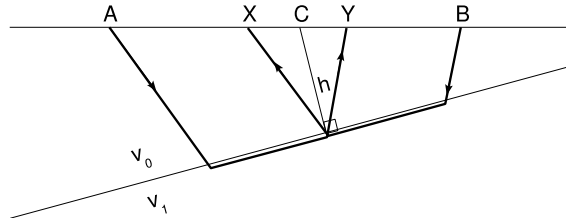


Figure 1.3: Raypaths in the generalised reciprocal method. The rays from reciprocal sources are emerging from the same point on the interface.

The reciprocal methods (plus-minus method and generalised reciprocal method) are one of the most widely layered-based interpretation methods used in the shallow refraction seismology – the Hagedoorn's plus-minus method and the Palmer's generalised reciprocal method. Reciprocal methods use reverse shots (thus reciprocal) for the determination of depths and velocities of seismic layers, and are therefore capable of resolving changes of velocities and depths of layer interfaces – 2D models. The fact that they are specifically adapted for reverse shots makes serious difficulties when adapting them to 3D surveys, although attempts have already been done (Palmer, 2001).

The Hagedoorn's plus-minus method is derived from the wavefronts, and data processing using this method can be done also graphically (Hagedoorn, 1959). This method determines normal depth to the interface and velocity at the

boundary under each geophone from the spread. The procedure is based on equation (1.6) applied to reverse shots. Being A and B shots on each end of the spread, depth at point C on the profile (Fig. 1.2) is determined from the “plus” term  $t_0$ :

$$t_0 = t_{AC} + t_{BC} - t_{AB}, \quad (1.7)$$

where  $t_{AC}$  is travel time from A to C,  $t_{BC}$  travel time from B to C and  $t_{AB}$  is the reciprocal time (from A to B). Velocity at this point is determined from the “minus” term  $\Theta$ :

$$\Theta = t_{AC} + t_{AB} - t_{BC}. \quad (1.8)$$

Substituting (1.6) into (1.7) and (1.8), we obtain the terms for the velocity of the refractor in the area of point C:

$$v_1 = 2 \frac{\Delta x}{\Delta \Theta}, \quad (1.9)$$

and normal depth at point C:

$$h = \frac{v_0 t_0}{2 \cos \theta}, \quad (1.10)$$

where the velocity  $v_0$  is the velocity of the overlying layer and  $\theta$  is the critical angle.

The plus-minus method is well suited for processing 2D refraction datasets in the case, that the refractor is not highly irregular and the slope of the refractor is not too steep. Its main advantage is, that it is able to resolve lateral variations in velocities and depths of the refractor as it gives values of refractor depth and velocities under each geophone of the spread.

We have stated that the plus-minus method is not suitable for highly irregular interfaces. When we have to deal with such a case, we may use the *generalised reciprocal method* (GRM) by Derecke Palmer (Palmer, 1980). The GRM is similar to the plus-minus method in some aspects, but may be used under a wider range of conditions. It is capable of resolving dips of up to 20 %, while the plus-minus method is considered to be reliable only for dips of max. 10 %.

The data processing technique resembles the plus-minus method as it also uses a kind of plus and minus terms. The “minus” term is called a velocity analysis function  $T_V$  and the “plus” term is called a time-depth function  $T_G$ . However, the computation of parameters under point C is based on times measured at points X and Y chosen so that the reciprocal rays emerged from the refractor at the same point (see Fig. 1.3 and compare it with Fig. 1.2). To simplify computations, distances XC and CY are considered to be equal. The determination of the XY distance will be mentioned later. For detailed information about generalised reciprocal method and derivation of equations consult the Palmer’s book describing this method (Palmer, 1980).

The processing starts with the computation of  $T_V$  and  $T_G$ :

$$T_V = \frac{t_{AY} - t_{XB} + t_{AB}}{2}, \quad (1.11)$$

$$T_G = \frac{t_{AY} + t_{XB} - \left( t_{AB} + \frac{XY}{V'_N} \right)}{2}, \quad (1.12)$$

where  $V'_N$  is the apparent velocity:

$$\frac{dT_V}{dx} = \frac{1}{V'_N}. \quad (1.13)$$

The apparent velocity is usually taken as the correct one. If we know the slope of the interface  $\varphi$ , then the estimate can be improved:

$$\frac{dT_V}{dx} \simeq \frac{\cos \varphi}{V_N}, \quad (1.14)$$

where  $V_N$  is the real velocity. Combining equations (1.13) and (1.14) we get the relation between the real and the apparent velocities:

$$V_N \simeq V'_N \cos \varphi. \quad (1.15)$$

The time-depth function describes the changes in refractor depths along the profile and therefore corresponds to the one-way travel time-depth function known from the reflection methods. To convert it to the real depths of the interface, we have to find the depth conversion factor  $V_{jn}$ , which, when the dip angles are ignored, is approximated:

$$V_{jn} \simeq \frac{V'_n V'_j}{\sqrt{V'^2_n - V'^2_j}}, \quad (1.16)$$

where  $V'_n$  and  $V'_j$  are apparent velocities in layers underlying and overlying the refractor determined from equations (1.13) or (1.14).

The main problem with the generalised reciprocal method is the determination of the XY distance. Palmer (1980) describes a number of possible approaches:

1. For horizontal layering (or for small dips) the XY is:

$$XY = \sum 2h_{jC} \tan \theta_j, \quad (1.17)$$

where  $h_{jC}$  is the thickness of the  $j$ -th layer under the point  $C$  and  $\theta_j$  is the critical angle in this layer.

2. The XY value can be determined from the separation of distinctive features on the travel time curves.
3. Several  $T_V$  and  $T_G$  functions for different values of XY are plotted. Optimum XY value has the  $T_V$ ,  $T_G$  pair, where the velocity analysis curve is the most smoothed while the time depth function is the most detailed one.
4. The XY value is the distance where critical reflection occurs.

The XY value can also be used for the determination of *hidden layers* in the data set. Hidden layer is a layer from which the refractions do not come to the surface as first arrivals since usually only the first arrivals are processed. This can be, e. g., a thin low-velocity layer over a high-velocity layer. As the velocities and thicknesses of the hidden layers cannot be calculated, velocities and thicknesses of all possible underlying layers are determined with an error.

Another source of errors are *velocity inversions*, where a low-velocity layer underlies a high velocity one. Critically refracted rays are not produced on this interface, and the low velocity layer is not registered.

However, the presence of hidden layers or velocity inversions can be detected using the XY value. The XY value is primarily inferred from the analysis of  $T_G$  and  $T_V$  curves or by other described methods. Then, the depth section is computed. Now, the XY value can be determined from the depth section using equation (1.17). These two XY values must agree. If the observed XY value is greater than the calculated one, then the higher-velocity layers may be thicker, the layer velocities may be higher, or a blind zone may occur. If the observed XY value is lower than the calculated one, then the low-velocity layers may be thicker, layer velocities may be lower, or a velocity inversion may occur (Palmer, 1980).

### 1.3 Seismic tomography

Tomography, from Greek word *tomos* meaning “a section” or “a cutting”, is a technique for imaging of opaque solid materials by sections. It was developed in medicine for

imaging human body interior by means of X-rays. The concept was further developed in many other sciences – archaeology, biology, geology, materials science. And as every science has its own modification of the tomography concept to suit its needs, every incarnation of tomography differs. In geophysics, the most common type of tomography is the seismic tomography, which uses seismic rays to explore the Earth's interior.

Seismic tomography is currently one of the most widely used seismic processing tools. It is used for all types of seismic data acquisition – refraction, reflection, global seismology, surface waves. Tomography is a very versatile tool, which allows the use of various types of models to represent the studied geological structures. Its drawback is that, especially in 3D studies, the tomography is computationally very expensive.

In general, the tomography consists of three basic steps. The first one is the model parametrisation. The traditional velocity model for tomography is a single-layer model composed of small cells with arbitrary velocities. It enables only modelling of gradient media and refracted waves as illuminating rays. However, the technique was further developed to incorporate also interfaces, thus also other ray types – reflections and converted waves. The model parametrisation determines the model received from the tomography, its uncertainties and its spatial resolution, which are the most important. It is therefore necessary to give the model parametrisation the full attention as the parametrisation affects all other parts of tomography, as well as its results, and cannot be changed later during the inversion process.

The second step is the forward modelling. The input-parametrised model is taken, locations of sources and receivers are projected into the model, and seismic rays from sources to receivers are found. The ray tracing is a complex procedure and will be discussed further in Section 1.3.1. When the rays are traced, it is possible to compute travel times needed for a ray in the model to travel from a source to a receiver.

In the third step, the inversion, travel times obtained from forward modelling are compared with the measured travel times, and relevant corrections to the input model are applied. The forward modelling and inversion steps are then repeated until satisfactory differences between the measured and synthetic travel times are found, and, simultaneously, the revealed structure seems to be realistic.

In the following two sections we will go briefly through the tomography procedure. The basics of the forward modelling and inversion procedures will be outlined. The sections do not cover the whole area of seismic tomography. Neither are all the used methods and schemes presented. This is meant to be only a short summary for the readers so that they could see the main differences between the tomography and simple interpretation procedures mentioned before, and understand why the tomography results are (usually) as smoothed as they are.

### 1.3.1 Forward modelling

Forward modelling in seismic tomography can be reduced to the ray tracing. We have locations of sources and receivers and we need to know through which parts of the model (which cells) the ray travels and how long is the trajectory in individual cells. The ray tracing, especially in 3D media, is generally a complex problem, and a number of ray tracing techniques were developed. They can be divided into two categories: waveform methods and analytical or numerical solutions to the eikonal equation. The waveform methods are seeking numerical solution of the elastic wave equations, which leads to the propagation of seismic waves in the media. The eikonal is an approximation of the elastic wave equations describing spatial variations in amplitude and phases of the wave field. For more details on the two-point ray tracing see, e.g., the work of Hobro (1999), parts of which are cited here to outline the tomography procedure and document its pitfalls.

The ray tracing is usually implemented by computing the travel time field by finite-difference algorithm or by two-point ray tracing.

The concept of computing the travel time field was introduced by Hole (1992) and Hole, Clowes and Ellis (1992). The finite-difference code is used to compute the travel time field for every source in the dataset. The rays are then found by “backprojection” from the receiver to the source utilising the principle that rays are perpendicular to the isochrons. In other words, the raypaths can be found by travelling backwards from the receiver to the source, perpendicular to the isochrons (in a direction of the highest gradient of the travel time field). When the cell size of the model is small, the precision of this ray tracing is sufficient. This type of ray tracing is very stable, the raypaths are always found and therefore also the inversion performs extremely well. Moreover, this ray tracing technique is also very fast, especially in 3D media. The disadvantage is that this type of ray tracing is capable only of modelling of the first arrivals – direct, refracted, diffracted and head waves. However, Hole and Zelt (1995) introduced a concept of how to use this method in the computation of reflection travel times. The basic idea is that the wavefield and the ray are computed downwards to the reflector. The reflecting point then is considered to be a source and a new wavefield from this source is computed and the ray is traced up to the surface. With the increasing number of different wave types, however, the complexity of the code also increases. Hence the wave field calculations are not used for complex datasets, although being number one choice for the first arrival tomography.

When the processed dataset consists of different wave types – refracted, reflected, converted waves – and we want to use a layer-interface model, then we might consider using the ray formulation of the eikonal equation and two-point ray tracing. The procedure of two-point ray tracing is briefly outlined here to show its complexity. It can be seen that, for a complex model, the ray tracing becomes very complex and non-unique (it is not possible to solve the ray equations analytically), the ray trajectories cannot be determined and the whole tomography procedure fails.

We start with the *eikonal equation*:

$$(\nabla S)^2 = \frac{\alpha_0^2}{\alpha^2}, \quad (1.18)$$

*To denote velocity of P-waves as  $\alpha$  is a tradition when deriving the wave equations. Therefore it is used here as well to be consistent with the literature. On all other places in this text the velocity is denoted as  $v$ .*

where  $\alpha$  is the wave speed and  $\alpha_0$  the reference wave speed. The Function  $S$  is a part of an eikonal describing the spatial variations of the phase within a general wavefield. The ray is the path of the wave packet through the medium, being at all times perpendicular to the wavefront with the unit vector:

$$\hat{\mathbf{p}} = \frac{\alpha}{\alpha_0} \nabla S. \quad (1.19)$$

It can be shown (e.g., Hobro, 1999) that a combination of equations (1.18) and (1.19) can produce the ray equations:

$$\frac{d\mathbf{x}}{ds} = v\hat{\mathbf{p}} \quad \text{and} \quad \frac{d\hat{\mathbf{p}}}{ds} = \nabla \left( \frac{1}{v} \right), \quad (1.20)$$

where  $\mathbf{x}(s)$  is a function describing the ray path and  $s$  is the curvilinear distance from a reference point along the ray path,  $v(\mathbf{x})$  is the wave speed. These differential equations with appropriate boundary conditions can be used to trace the trajectory of the ray. Knowing the trajectory, we can obtain the travel times by integrating the eikonal equation along the ray path:

$$T = \int_{\text{ray path}} |\nabla T| ds = \int_{\text{ray path}} \left( \frac{1}{v(\mathbf{x}(s))} \right) ds. \quad (1.21)$$

The needed boundary conditions are (Hobro, 1999):

1. Source position and direction of propagation are specified – find the position at which the ray returns to the surface and the travel time;

2. Source position and direction of propagation are specified – find the position in the model at which the travel time is reached;
3. Start and end point are specified – find all rays which join the two together and their travel times.

The easiest to solve are the conditions 1 and 2. The ray equation is integrated through the given model where the starting position and slowness vector are known. Then, the ray is traced until it reaches the surface or leaves the model (condition 1) or until the given travel time is reached (condition 2).

Condition 3, the *two-point problem*, is the most difficult to solve. In a simple model, it is possible to find analytical solution but the problem becomes too complex and non-unique for real models. If we have to find a set of synthetic travel times for a given model and source-receiver geometry, this is the condition we need to solve. Possible approaches to solve the two-point problem are:

1. Ray bending methods – the trial ray path is refined until it meets the two-point boundary conditions. This method is efficient and relatively stable, however, it does not always converge to the shortest travel time and may not correctly identify a situation for which a solution does not exist.
2. Shooting methods – they begin with series of solutions to condition 1, and then use the results to obtain a set of two-point solutions. Shooting methods are able to find multiple solutions to the two-point problem and are efficient for a small number of sources and a large number of receivers.
3. Shortest path methods – they form a dense and simple parametrisation of the medium and then apply the network theory to find the shortest path ray solution. These methods are efficient when a high degree of accuracy is not needed, and only the shortest path is sought.

The forward modelling problem is much more complex than it was outlined here and in its full coverage is beyond the scope of this text. For more details see, e.g., the work of Hobro (1999). We should mention here only the Fréchet derivative which, for a ray segment within a single cell, relates the travel time to each of the model parameters defining the velocity within this cell. In other words, it measures sensitivity between the travel times and the model:

$$a_{ij} = \frac{\partial t_i}{\partial m_j}, \quad (1.22)$$

where  $a_{ij}$  is the Fréchet derivative relating time  $t_i$  to model parameter  $m_j$ . All terms  $a_{ij}$  form the matrix of Fréchet derivatives  $\mathbf{A}$ .

### 1.3.2 The inversion

This is the final step of each iteration of the tomography procedure. We have computed the synthetic travel times  $\mathbf{t}$  from the current model, and now we have to compare them with the measured travel times  $\mathbf{t}_{\text{real}}$ . The difference (residual vector)  $\mathbf{r}$  between these measures the “quality” of the current model, its fitness:

$$\mathbf{r} = \mathbf{t}_{\text{real}} - \mathbf{t}. \quad (1.23)$$

Whenever the difference between the synthetic and measured travel times decreases, the model should be closer to the real structure. We have to minimise  $\mathbf{r}$ . It can be shown that the relationship between small perturbations in model parameter and the resulting perturbation in the synthetic travel time can be approximated by a linear equation. Or, from the other side, small changes in the synthetic travel time vector

$\partial \mathbf{t}$  are related to small changes in model parameters  $\partial \mathbf{m}$  via the matrix of Fréchet derivatives  $\mathbf{A}$  by the equation:

$$\partial \mathbf{t} = \mathbf{A} \partial \mathbf{m}. \quad (1.24)$$

This equation is valid in the region where we can approximate the relationship between the perturbation in travel times and perturbation in model parameters to be linear. We are looking for the perturbation which improves the model to better fit the data, but small enough to stay in the region of linearity.

After combining equations (1.23) and (1.24), we obtain a system of linear equations:

$$\mathbf{t}_{\text{real}} - \mathbf{t} = \mathbf{A} \partial \mathbf{m}, \quad (1.25)$$

which can be solved by simple matrix inversion if the problem is well-constrained:

$$\partial \mathbf{m} = (\mathbf{A}^t \mathbf{A})^{-1} \mathbf{A}^t (\mathbf{t}_{\text{real}} - \mathbf{t}). \quad (1.26)$$

The tomography problem, however, is hardly ever well-constrained as the 2D tomography (from the surface) has usually about a half of the model unattended, and thus unconstrained, by the rays, and the seismic rays in 3D tomography usually constrain only about one-third of the model cells. Matrix  $\mathbf{A}$  is often ill-conditioned because of the non-uniqueness of the problem – there is more than one way how to improve the model to better fit the data. Even if most of these ways are physically unrealistic (e.g., negative velocity values). All this implies that we need an inversion scheme which would enable the use of *a priori* information to make the model develop only in a well-constrained area and to make the level and the nature of the developed structure somehow fit the expectations based on the knowledge of possible structure, experiment geometry and possible constraints of data. All these requirements are usually incorporated in the inversion process by applying smoothing constraints to the model during the inversion.

To measure the size of the residual vector  $\mathbf{r}$  (difference between the synthetic and measured travel times), a suitable norm must be selected. The most often used norm is the  $l_2$  norm and sometimes also the  $l_1$  norm.

The  $l_2$  norm means that size of the vector is a sum of its squared components:

$$\|x\|_2 = \sqrt{(x_1^2 + x_2^2 + \dots + x_N^2)}. \quad (1.27)$$

This norm leads to the least squares formulation of the problem. It is the most frequently used norm because the least squares theory is well developed, widely used, and many sophisticated algorithms for its solution are available. However, the least squares formulation expects data, errors and parameters to have normal (Gaussian) distribution, which is not necessarily the case of real data. Data often contain large errors, outliers, spoiling the whole inversion process.

In contrast, the  $l_1$  norm:

$$\|x\|_1 = |x_1| + |x_2| + \dots + |x_N|, \quad (1.28)$$

which leads to the least absolute deviation formulation is better suited for real data containing outliers. The least absolute deviation formulation is, however, less common as it is more complex to implement and less developed. When implemented, it is usually called “robust inversion”. More information about norms and their applications can be found, e.g., in the Tarantola’s book (2005), or in Press *et al.* (1994).

We have stated, that the most common is the least squares formulation, despite its negatives. Here we can choose from an assortment of well developed methods. One of the easiest to use and therefore very common is the damped least squares method. However, this method is generally not recommended as its smoothing effect is not consistent, may fail and is dependent on the used parameter density (Hobro, 1999). A



possible alternative to this method is to use the regularised least-squares method and control the step towards the minimum of the objective function using the conjugate gradient method. A detailed description of regularised least squares and conjugate gradients was given by Hobro (1999).

## 1.4 Time-term method

The time-term method is a simple layer-based method of seismic refraction data analysis. It was originally designed by Scheidegger and Willmore (1957) to interpret sparse 3D seismology data. Due to the sparse data, the inversion process was limited to a model of a layer over a half-space with constant velocity. The resolved parameters were the depths of the interface and the velocity of the half-space. The method is derived from equation (1.5) for travel time of the head wave on the horizontal plane. Then, for a set of travel times it is possible to build a set of linear equations, which gives the depths to the refractor and the refractor velocity.

The original version of the time-term method does not enable computation of lateral changes of velocities which is of crucial importance in the near-surface geophysics. Therefore we have modified the method in a manner that it enables computation of lateral velocity changes along the refractor. This is similar to the method described by Hearn and Clayton (1986). However, we do not use the velocity depth profiles for station and event delays because this is not common in shallow seismics. Vertical velocity changes, if necessary, can be expressed by a higher number of layers. The lateral velocity changes of the overlying layer are determined from the direct wave. The solution of the obtained system of linear equations also differs from the solution described by Hearn and Clayton (1986). In order to stabilise the inversion process we introduce an a priori information to the equations and solve the system using the singular value decomposition. This is necessary for applying this method to highly heterogeneous media (Valenta and Dohnal, 2007).

We divide the refractor into  $n \times m$  cells, each with a constant velocity. There are  $X, Y, Z$  coordinates of the  $p$  sources and  $q$  receivers. Now we have to find the ray path for each source–receiver pair along the refractor. The ray tracing in three dimensions is generally a complex problem. To keep the computations simple, we avoid ray tracing by assuming straight raypaths, although we are aware of bringing an error into the dataset. The gain is the simplicity and computational speed. Moreover, the error might not be as large as it may seem (see Section 1.4.1). The modified equation is then similar to equation (1.6):

$$t_{ij} = \frac{h_{si} \cos \theta_{si}}{v_{0si}} + \frac{h_{rj} \cos \theta_{rj}}{v_{0rj}} + \sum_{k=1}^m \sum_{l=1}^n \frac{\Delta_{kl}}{v_{1kl}}, \quad (1.29)$$

where  $t_{ij}$  is the travel time between  $i$ -th source and  $j$ -th receiver,  $h_{si}$  is the depth beneath the  $i$ -th source,  $h_{rj}$  is the depth beneath the  $j$ -th receiver,  $\theta_{si}$ ,  $\theta_{rj}$  are the critical angles in the areas of  $i$ -th source or  $j$ -th receiver, respectively,  $v_{0si}$ ,  $v_{0rj}$  are velocities in the upper layer beneath the  $i$ -th source and  $j$ -th receiver,  $\Delta_{kl}$  is the length of the ray path in the  $kl$ -th cell of the refractor and, finally,  $v_{1kl}$  is the velocity of the  $kl$ -th cell of the refractor. The velocities in the upper layer can be determined directly from the travel time curves. The velocities of the refractor cells and depths to the refractor beneath the sources and receivers are the unknowns.

We substitute slownesses  $s$ , the velocities reciprocals, for velocities  $v$ . Finally, for the whole dataset we obtain a system of  $p \times q$  linear equations with  $p + q + n \times m$  unknowns – depths  $h$  and slownesses of the refractor  $s$ . The system can be expressed in the form:

$$\mathbf{t} = \mathbf{A}\mathbf{x} \quad (1.30)$$

where  $\mathbf{t}$  is the column vector of measured travel times,  $\mathbf{x}$  is the vector of unknowns, and  $\mathbf{A}$  is the matrix of coefficients (equation (1.31)).

Critical angle  $\theta$  is in principal unknown, as we do not know the velocity of the underlying layer. This can be bypassed by assigning an *a priori* value of velocity to the refractor and solving the system. Then, the computed velocities can be used for the computation of  $\theta$  in a low number of iterations.

Solution of this linear system gives directly the searched depths and slownesses. However, this system is usually ill-determined, and some kind of regularisation is necessary. A suitable approach to the regularisation is to add an *a priori* information. This was well described by Tarantola (2005). We added a vector of *a priori* information (depths under sources and receivers and slownesses of the refractor)  $\mathbf{m}_{\text{pr}}$ :

$$\mathbf{m}_{\text{pr}} = \begin{pmatrix} HA_{pr\ 1} & \dots & HA_{pr\ p} & HB_{pr\ 1} & \dots & HB_{pr\ q} & s_{2\ 11} & \dots & s_{21mn} \end{pmatrix}, \quad (1.32)$$

covariance matrix of uncertainties  $\sigma_d$  of measured data  $\mathbf{C}_D$ :

$$\mathbf{C}_D = \begin{pmatrix} \sigma_{d\ 11}^2 & 0 & \dots & 0 \\ 0 & \sigma_{d\ 12}^2 & \dots & 0 \\ \vdots & \vdots & \ddots & \vdots \\ 0 & 0 & \dots & \sigma_{d\ pq}^2 \end{pmatrix} \quad (1.33)$$

and covariance matrix of uncertainties of *a priori* values  $\mathbf{C}_M$ , created in the same manner as the  $\mathbf{C}_D$  but with  $\sigma_{mpr}$  for every coefficient of vector  $\mathbf{m}_{\text{pr}}$ .

With *a priori* information, the system is (Tarantola, 2005):

$$\mathbf{x} = \mathbf{m}_{\text{pr}} + (\mathbf{A}^t \mathbf{C}_D^{-1} \mathbf{A} + \mathbf{C}_M^{-1})^{-1} \mathbf{A}^t \mathbf{C}_D^{-1} (\mathbf{t} - \mathbf{A} \mathbf{m}_{\text{pr}}), \quad (1.34)$$

where  $\mathbf{M}^t$  denotes transpose of matrix  $\mathbf{M}$  and  $\mathbf{M}^{-1}$  denotes inversion of matrix  $\mathbf{M}$ .

Solution of the equation, e.g., using the singular value decomposition method, gives the vector of unknowns  $\mathbf{x}$ . It is desirable to have an idea about how precisely resolved is each individual unknown. This can be achieved using the covariance operator  $\tilde{\mathbf{C}}_M$ :

$$\tilde{\mathbf{C}}_M = (\mathbf{A}^t \mathbf{C}_D^{-1} \mathbf{A} + \mathbf{C}_M^{-1})^{-1}. \quad (1.35)$$

Standard deviations  $\sigma$  of the resolved parameters are square roots of diagonal elements of the covariance operator  $\tilde{\mathbf{C}}_M$ .

The only problem might be in supplying *a priori* information, but series of tests showed that the method is not too sensitive to slightly wrong parameters.

The described method can be extended to a simultaneous use of S-wave arrivals. The matrix of S-slownesses of each refractor will be appended. Depths for the S-wave boundaries may be the same as for the P-wave structure or different thereby increasing the number of unknown parameters, what should be more appropriate for particular geological settings.

Reliability of this method was tested by comparing computed results with those from the plus-minus method and by adding artificial noise to the data (see Chapter 2). The usability evaluation of this method was executed by comparing it with 3D seismic tomography on two field examples. The first example comes from an archaeological site (Chapter 2), where the time-term method gave better results than the tomography. In the second example, focused on the detection of fracture systems (Chapter 3), the tomography provided better results and the time-term method lost.

#### 1.4.1 Realistic or straight raypaths?

Simple equations for a head wave on the interface (1.3), (1.4), (1.5), (1.6) and (1.29) can be used either for 2D or 3D configurations, because the only parameter depending

$$\mathbf{A} = \begin{pmatrix} \cos\theta_s 1s_{0s} 1 & 0 & \dots & 0 & \cos\theta_r 1s_{0r} 1 & 0 & \dots & \Delta_{11}s_{11} 11 & \dots & \Delta_{mn}s_{1mn} \\ 0 & \cos\theta_s 2s_{0s} 2 & \dots & 0 & \cos\theta_r 1s_{0r} 1 & 0 & \dots & \Delta_{11}s_{11} 11 & \dots & \Delta_{mn}s_{1mn} \\ 0 & 0 & \dots & \cos\theta_s p s_{0s} p & \cos\theta_r 1s_{0r} 1 & 0 & \dots & \Delta_{11}s_{11} 11 & \dots & \Delta_{mn}s_{1mn} \\ \cos\theta_s 1s_{0s} 1 & 0 & \dots & 0 & 0 & \cos\theta_r 2s_{0r} 2 & \dots & \Delta_{11}s_{11} 11 & \dots & \Delta_{mn}s_{1mn} \\ 0 & \cos\theta_s 2s_{0s} 2 & \dots & 0 & 0 & \cos\theta_r 2s_{0r} 2 & \dots & \Delta_{11}s_{11} 11 & \dots & \Delta_{mn}s_{1mn} \\ \vdots & \vdots & \vdots & \vdots & \vdots & \vdots & \vdots & \vdots & \vdots & \vdots \\ 0 & 0 & \dots & \cos\theta_s p s_{0s} p & 0 & 0 & \dots & \Delta_{11}s_{11} 11 & \dots & \Delta_{mn}s_{1mn} \end{pmatrix}. \quad (1.31)$$

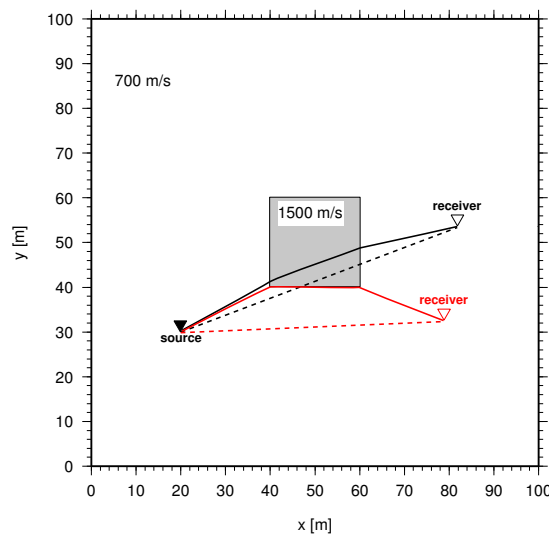


Figure 1.4: A comparison between the length of real – minimum time (solid line) and straight – minimum distance (broken line) raypath. An idealised model of horizontal refractor (P-wave velocity  $700 \text{ ms}^{-1}$ ) containing a high velocity anomaly ( $1500 \text{ ms}^{-1}$ ). The real raypath bends towards the high velocity anomaly. Two receiver positions are plotted here. One “common”, plotted in black and one “extreme”, plotted in red. The lengths of the rays are very close. The “common” case – the straight raypath is 66.019 metres long while the real one is 66.144 metres long. The “extreme” case – the straight raypath is 58.825 metres long and the real one is 61.813 metres long, which makes difference of 5 %. The real raypaths were derived from the travel time field computed with a finite difference code – `sufdmod2` program from the Seismic Unix package (Cohen and Stockwell, 2007).

on the geometry is the distance  $x$ . The distance can be computed along the realistic irregular curved ray-path (minimum time path) accounting for the bending of the ray, diffraction etc., or along the straight path (minimum distance path) assuming we are aware of an error introduced into the dataset. This error, however, may not be as fatal as it might look when we take into account the size of the Fresnel zone and work with small distances (metres and tens of metres which is the case of near-surface prospection) as demonstrated in Figure 1.4 and discussed further. The curved raypath is used mainly in the seismic tomography where accounting the ray curvature is essential (the rays start at the source and end at the receiver and there is no other information about their path in the dataset). In contrast, simple refraction inversion schemes often utilise straight raypaths to simplify the whole process. In this case, the source and the receiver positions are known, and also information on which refractors the ray travelled must be derived from data as an input parameter for inversion.

An idealised horizontal refractor with a high-velocity anomaly is presented in Figure 1.4. The seismic wave velocity of the refractor is  $700 \text{ ms}^{-1}$  and the velocity of the anomaly is  $1500 \text{ ms}^{-1}$ . The time field from the source was computed using the finite difference code `sufdmod2` from the Seismic Unix package (Cohen and Stockwell, 2007). Isochrons near the source are inaccurate due to computational errors and should form circles, however, this is of small importance for this example. Two cases are shown in the figure. The first one for a “common” orientation of the source and the receiver (plotted in black), and the second one for an “extreme” case where differences are the largest (plotted in red). For the “common” case, the straight raypath, taken as the shortest distance between the source and the receiver is 66.019 metres long, while the real raypath (minimal time according to the isochrons) is 66.144 metres long. It is obvious that the difference in length between these two raypaths is negligible. The “extreme” case has the straight raypath 58.825 metres long and the real raypath 61.813 metres long. This makes a difference of 5 %, which is often considered the highest acceptable error in many measurements.

The main difference between the real and straight raypaths is in the points (or cells) “sampled” by the rays. However, it is not as simple as it may look like. The

1<sup>st</sup> Fresnel zone must be taken into account. The peak frequency in the wavelet was 50 Hz. Using equations (1.1) and (1.2), the radius of the Fresnel zone can be estimated, e.g., in its maximum radius in the middle of the ray (33 metres from the source). In the slower part of the refractor, the radius is approximately 15 metres while in the faster part it is 22 metres wide. The question is, what portion of the 1<sup>st</sup> Fresnel zone should be considered significantly influenced by the media. In Section 1.1 we have adopted the one-third of the 1<sup>st</sup> Fresnel zone as the influence zone. Thus we get an influence zone of five metres for the slower part and seven metres for the faster part of the refractor. Both raypaths (real and straight) will be influenced by almost the same structure in many cases and the information contained in both of these rays should be therefore roughly identical. The negative aspect of this approach becomes obvious if we compute the inversion with a dense parametrisation of the refractor. If the real and straight raypaths do not cross the same cells, we will assign the computed velocities to wrong cells in the case of straight rays. Even if these wrong cells neighbour the correct cells, as is often the case, we will blur the resolved image. Anyway, this is an inevitable consequence of any simplification. The gain is the computational speed and simplicity of implementation (no need for ray tracing). Finally, the density of the parametrisation should coincide with the density of measured data (rays). When the ray coverage is sufficiently high, then the blurring effect is partly compensated by the rays travelling in perpendicular directions.

From the previous considerations, it can be derived that:

1. It is not essential to use minimum-time raypaths (for the head wave travelling along the refractor) due to the minimum difference in lengths of the real and straight raypaths and due to the influence zone.
2. In the case of dense parametrisation of the refractor, computed velocities might be assigned to wrong (mostly neighbouring) cells during the inversion process. This will lead to blurring of the resolved anomalies.



## Comparison of the time-term method and tomography – a field example from the Děvín Castle

The 3D seismic prospection is still not very common in routine shallow seismic investigations. This fact can be ascribed to a number of reasons, one of which is the complexity of data processing. However, in the case of a highly heterogeneous environment, like at archaeological sites, the benefits of 3D prospection highly exceed the negatives.

The most common technique in the processing of 3D refraction data sets is the travel time tomography. This method is based on the concept that the media, where the seismic waves propagate, have a velocity gradient. This implies the main drawback of tomography methods. If the geological environment is closer to the layered model than to the gradient one and layer boundaries are to be obtained, the gradient model might be problematic. Even if the algorithms combining the tomography and interface inversion do exist, their application is not without problems. The second disadvantage of the tomography methods is the complexity of ray tracing in 3D media and the consequent very long computational times. The latter was overcome by introducing the back-projection method (Hole, 1992), where the time field is computed using the finite-difference algorithm and ray tracing is performed backwards from the receiver to the source perpendicular to the isochrons of the time field. This ray tracing is fast and stable as the appropriate raypath is always found. And the third main drawback of tomography method is the smoothing applied to the computed model. Even if the grade of smoothing is usually selectable, there is always some smoothing present in order to stabilise the inversion process.

The smoothing applied in tomography might be the most important limitation of this method in archaeology. The smooth models are adequate for the deep seismic investigation of the crust, where the frequencies of seismic waves are low and thus their resolution is limited. In the near surface geophysics higher frequencies and small distances are used and therefore also more subtle details may be resolved. Whilst in the regional seismology even the smooth models might be too complicated to be reasonably explained, in archaeological prospection, where the media is highly heterogeneous and any subtle change in depth or velocity might be substantial it is essential to keep the level of smoothing as low as possible.

Another important claim on archaeological survey is to determine layer interfaces, because remnants of walls and moats are often better resolved from the changes in depth of interface than from changes in velocities.

Therefore we should look for some method which is able to handle layer interfaces and use as low amount of smoothing as possible or even does not apply smoothing

*The frequencies common in the global “earthquake” seismology are of magnitude of 0.X–X Hz and on the regional refraction profiles frequencies up to the 20 Hz might be encountered in the vicinity of the source. In the near surface seismics with impact source the frequencies are usually about 40–60 Hz. The difference is not high, but still substantial.*

at all. The method of choice may be some highly sophisticated tomography method, which can resolve the layer velocities and interfaces simultaneously. However, such tomography methods are quite complicated and need very high ray coverage to converge successfully. The author has chosen the time-term method by Scheidegger and Willmore (1957) and adapted it to handle lateral variations and a heterogeneous media (Valenta and Dohnal, 2007). The time-term method fits the layer boundaries into the data using the least-squares criterion. The raypaths are considered to be straight (see Section 1.4.1) and thus the computations are fast and simple, but still reasonably accurate. Description of this method can be found in the Section 1.4.

As an accompanying method the conventional 3D tomography method using a gradient media without interfaces was applied.

## 2.1 History, geological and geophysical settings

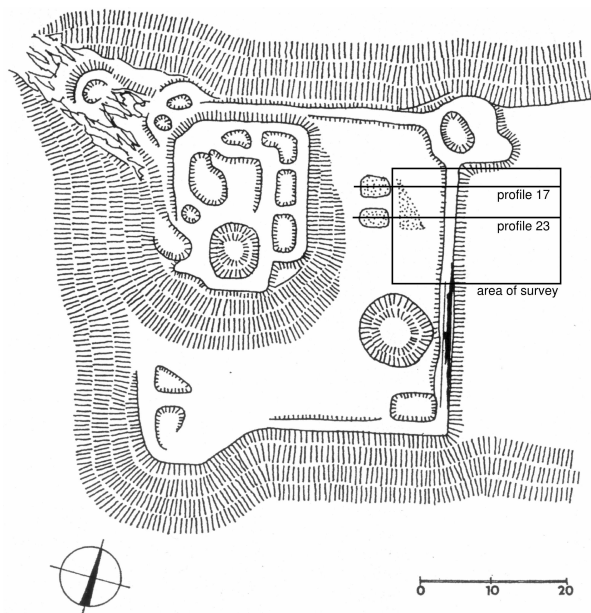


Figure 2.1: A map of remnants of the Děvín Castle according to the archaeological prospection (Durdík, 1999). Plotted is the area of geophysical research – rectangular area of the 3D measurements and two seismic profiles.

The Děvín Castle was a small 14<sup>th</sup> century fortification built on top of an elevation upon the Vltava River in the southern part of Prague. However, the place was settled long time before the castle was built. Some remnants of older fortified settlement, probably Slavonic, can be found in the vicinity. The date of origin of this fortification is not known, and neither is the time of its destruction. In the second half of the 11<sup>th</sup> century, it was already in ruins. And already then, nobody had known nothing about its genesis, rise or fall.

For some four centuries, the place remained unsettled, and was a property of the Czech king. In the early 14<sup>th</sup> century it was exchanged in return for the Tetín manor. Its new owner, Štěpán of Tetín, built the castle here some time before the

year 1338. The castle was probably destroyed and abandoned during the Hussite Wars in the first half of the 15<sup>th</sup> century. In the early 16<sup>th</sup> century, the remnants were used as a military target for testing guns (Sedláček, 2000). Even after this, the remnants were still apparent until the early 19<sup>th</sup> century when they were totally destroyed, probably exploited as building stones. Only parts of the castle are apparent in the present terrain morphology.

The geological bedrock is formed by Devonian limestones and micritic limestones, weathered in a near-surface zone. The limestones are covered with Quaternary loess, the thickness of which does not exceed 1.5 m over the whole site. Velocities of the highest parts of the bedrock are hard to estimate because they highly depend on the degree of weathering and usually ranges between 1000 and 4000 m/s (the latter for highly compact limestones). The micritic limestones at the locality can be expected to have velocities between 1700–3500 m/s.



The soil mantle of this locality have velocities ranging roughly between 300 and 500 m/s, which are frequently encountered velocities for the soil mantle.

Velocities in walls are probably similar to the velocities in the bedrock, but not necessarily. Velocities of substance in the moat are hard to estimate as they depend on the filling of the moat.

## 2.2 Data acquisition

The part of the castle where relics of a rampart were apparent from the topography (Fig. 2.1) was selected for the test survey. Shallow seismic refraction was chosen, among other geophysical methods (DC tomography, gravity survey), to reveal remnants of the castle here.

Two 2D profiles crossing the assumed rampart were measured and a 3D seismic refraction was carried out in this area. Seismic data from both sources were processed by picking arrival times and computing the gradient and layered models. The gradient models were derived using the tomography technique. The 2D layered models were obtained using the plus-minus method. The 3D layered model was computed by a linear least-squares fitting of a refractor boundary to the data – a modification of the original time-term method. This method is described in Section 1.4.

The 2D profiles were 34.5 metres long, and were measured using a 1.5 metre distance between geophones. The profiles were located on the x-coordinates 17 and 23 metres of the 3D grid. 3D data were obtained in a grid, where the geophones were deployed in a 4×4 metres mesh interlaced with the same mesh of sources, thus both together created a mesh of 2×2 metres. Moreover, additional shots were deployed on all four sides of the grid at a distance of five metres. In total, 24 geophones and 64 shots were used.

For all seismic measurements on this locality the 24-channel Geode seismograph from the Geometrics company was used.

## 2.3 Processing of 3D data sets

The aim of the survey was to find possible relics of ramparts and moat of the medieval castle. Parts of the ramparts could be distinguished in the terrain morphology, but most of the ramparts and position of the moat could not be determined this way.

The relics of ramparts and moats can usually be detected as elevations and depressions of the cover–bedrock interface. Foundations of ramparts are usually dug into the bedrock and high-velocity ramparts are usually detected as a sharp bedrock elevations. Ramparts might also be detected as a high-velocity anomalies, however their detection as velocity anomalies is not as reliable as changes in the depths. In contrast, the moat, also usually dug into the bedrock, forms distinctive depression. The velocities in the area of former moat might be higher or lower than in the surrounding media. It depends on the filling of the moat. On one hand, if the moat was slowly filled with the soil flushed away from the neighbourhood – slow decay of the castle – then the area of moat forms low-velocity anomaly. On the other hand, if the moat was filled by ruins of collapsed bulwark, than the moat forms high-velocity anomaly.

The data processing was, therefore, primarily aimed at resolving of cover–bedrock interface depths. To achieve this aim a layer-based interpretation method was necessary. The time-term method was selected and modified for this task (for description of this method see Section 1.4).

*The filling of the moat is hard to estimate, because number of different types of filling are encountered. When the moat is filled with remnants of walls, then the values of velocities are approaching values encountered in walls, depending on the degree of decay of the remnants. If the moat is filled with soil flushed from neighbourhood, then the velocities are similar to velocities in soil mantle. But most often encountered filling of the moat is a mixture of remnants of masonry, flushed soil, organic material and rubbish from our ancestors. The velocity in this mixture may take an almost arbitrary value between the value of velocity in soil and in the walls.*

*The relics of bulwarks and moats are more often detected as changes in the refractor depth rather than in refractor velocities, even when the velocity contrast is usually substantial. It might be due to the fact, that velocities in the near-surface layers are changing very rapidly in both, vertical and lateral, directions and thus making a detection of subtle velocity anomalies difficult. Also computation of depths is often more precise than that of velocities (when using classical layer-based techniques like the plus-minus method).*

### 2.3.1 Time-term method

The time-term method was applied because it is a layer-based interpretation method. This method has only few of user-adjustable parameters, the main important being the size of the velocity cell of the refractor. The data were processed using the `refract3d` program (see Chapter 5) for four cell sizes – 0.5, 1, 2 and 3 metres. Then the optimal cell size of 1 meter was selected (Fig. 2.2). For effect of different cell sizes see Fig. 2.3 and 2.4.

Selection of optimal cell size is important to get the best from the method. If the cells are large, then the ray coverage in cells is sufficiently high (the system of linear equations (1.30) is well determined) and velocities in individual cells are reliably computed. The drawback is, that the resolved velocity image lacks details. In contrast, if the cells are small, then the system of equations is ill-determined and computed depths and velocities are thus not reliable. The cell size determination may be done by trial and error method by computing depths and velocities for number of different cell sizes and finally select that one, where the depths and velocities form acceptable structures with reasonable number of details. Moreover, the cell size should correspond to the step of geophones and sources. These cell size considerations are analogous to that ones involved in the tomography.

Before making any attempts on interpretation of time-term results we should check how reliable these results might be. We can test the reliability of this method by adding artificial noise to the data and by comparing computed results with those from the plus-minus method.

The first test was to compare results for the measured dataset and for the same dataset with an error of 10 % added to the travel times. This error is quite large, and such a noisy dataset would not be usually accepted as a reliable one. The results (Figures 2.2, 2.5) show that the computed depths of the interface are affected to only a negligible degree. Velocities of the refracting boundary are affected to a higher degree, however, the main archaeological features are still apparent.

The depths are affected less than the velocities, because they are better determined in the equations (see the matrix of coefficients  $A$  in the equation (1.31)). The depth beneath every source is determined by all equations, where this source is used (similarly also the depth beneath receivers). In contrast, not every velocity cell may be sampled by sufficient number of rays. Therefore the noisy datasets (or sparse datasets) should need more velocity damping or larger size of velocity cells.

### 2.3.2 Comparison of results of time-term and plus-minus methods

Results of 2D profiles and 3D time-term method are compared in Figure 2.7. The depths to the interface show very good overall correlation with the exception that the time-term method's interface is less smooth. This is, among others, caused by the fact that the plus-minus method involves some amount of smoothing (the velocities of the refractor are computed using a moving window). This may or may not be the benefit of the time-term method. It can be considered beneficial in this case because the trace of a moat is visible also on profile 17, in contrast with the plus-minus method. The velocities reasonably correlate in areas where the ray coverage is sufficiently high – in the centre of the area.

Now we will focus on the possible archaeological features resolved by these methods. An elevation of bedrock is visible at stations 62–63, where a possible rampart might be located. It is apparent on outputs from both methods, although very smoothed on profile 17 using the plus-minus method. The depression of bedrock around station 70 may be caused by a buried moat. It is well apparent on outputs from both methods on profile 23; however, it has a different shape. Time-term results indicate only a hint of the moat on profile 17; but this might be also due to the fact that the moat is

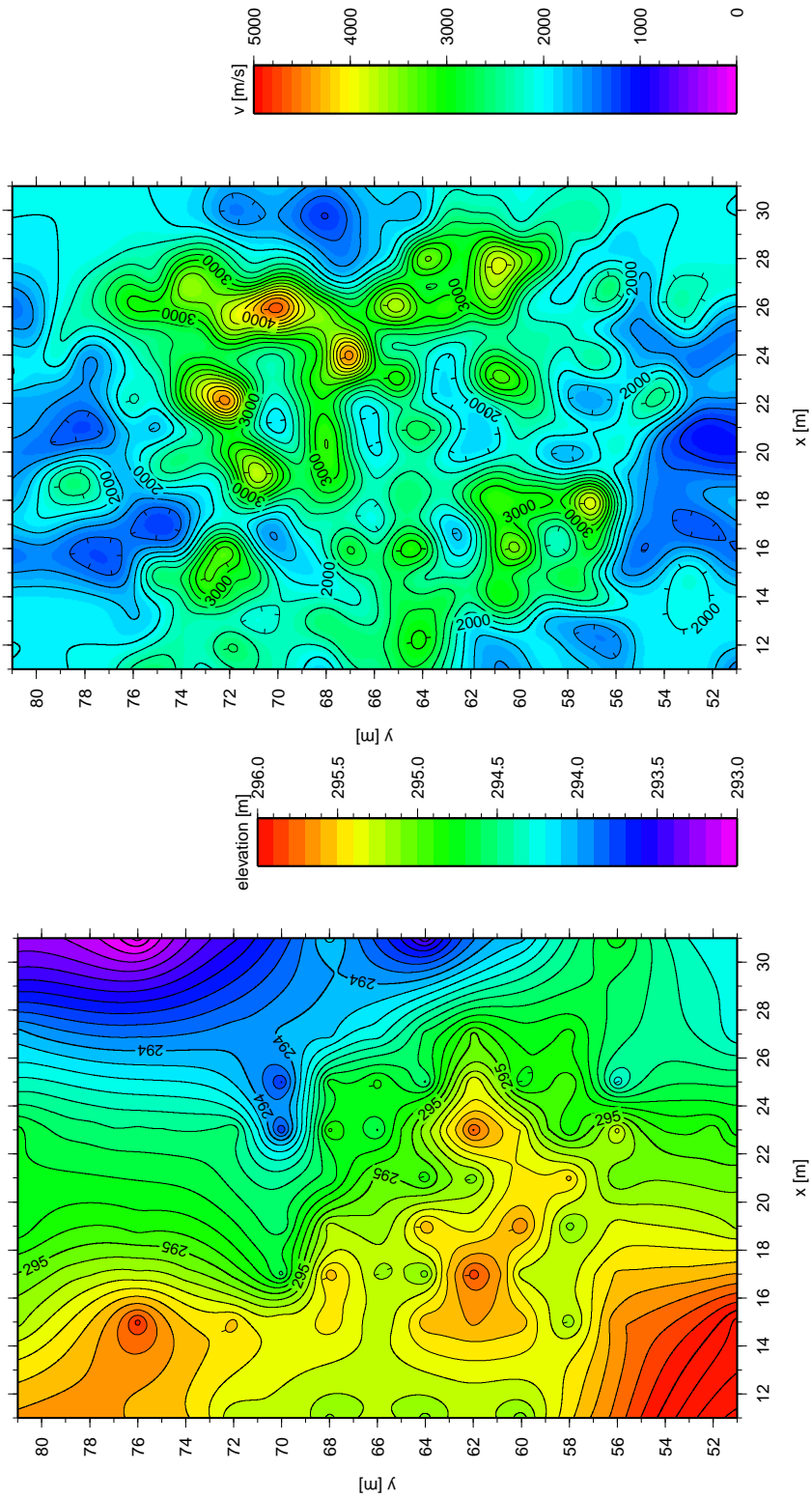


Figure 2.2: Depths of the bedrock interface and interface velocities resolved by the time-term method. The cell size was 1 meter. The anomalies form acceptable detailed structures while the scattering of velocities remains reasonably low.

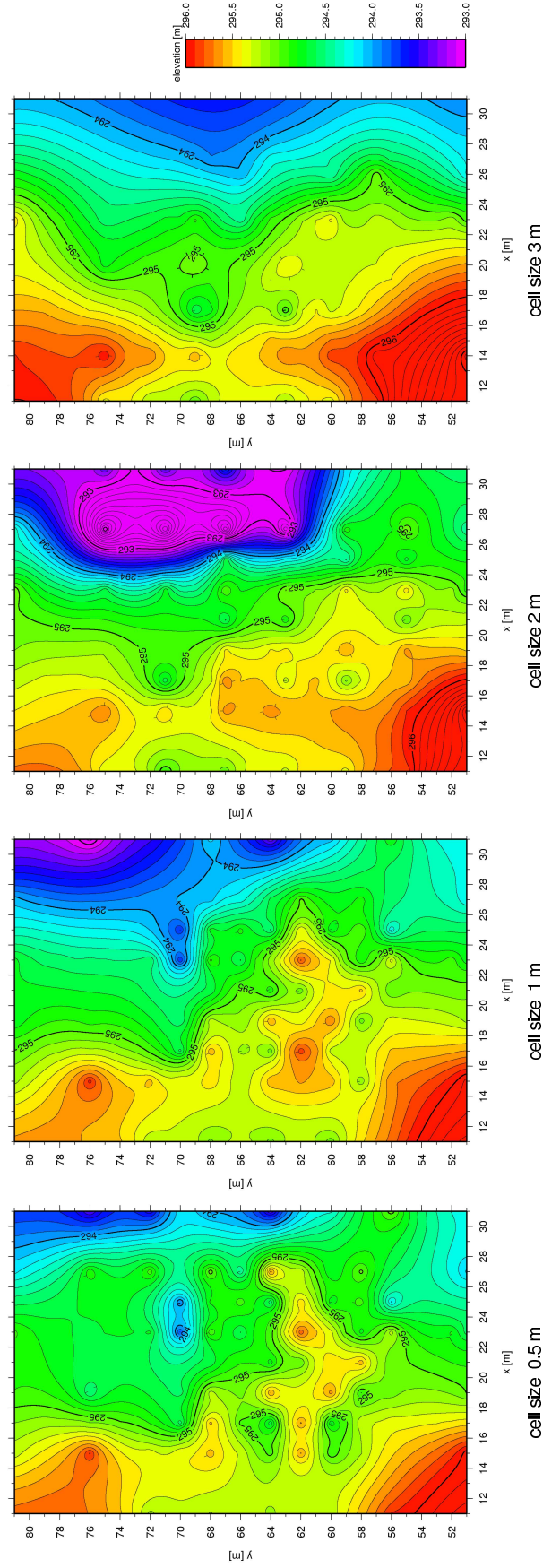


Figure 2.3: Comparison of influence of the cell size on results of the time-term method. Depths of the cover-bedrock interface are plotted here. Optimal cell size (determined by the density of rays) in this survey is 1 meter. It is the size, where the resulting image contains the largest amount of details whereas the computational errors due to the ill-determined system of equations (1.30) are sufficiently low. The cell size 0.5 meters is too small and the depths are too scattered. The cell sizes 2 meters and 3 meters are too large and the resolved interface lacks details.

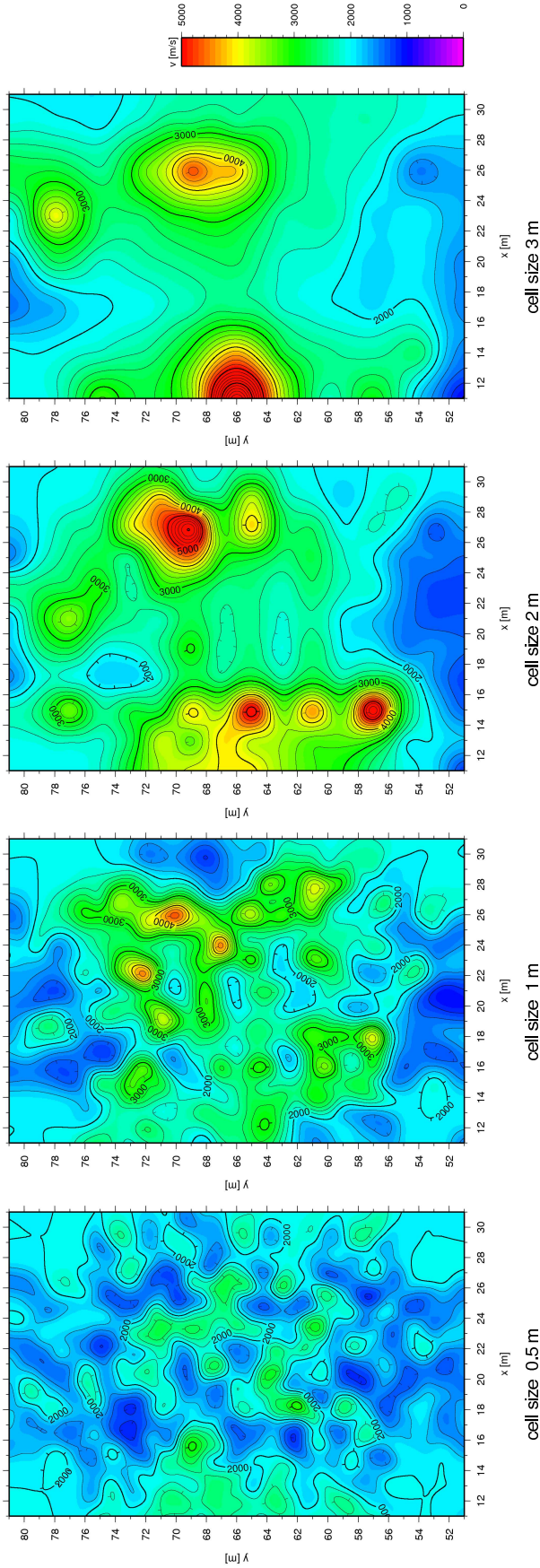


Figure 2.4: Comparison of influence of the cell size on results of the time-term method. Velocities on the top of the bedrock are plotted here. Optimal cell size (determined by the density of rays) in this survey is 1 meter. It is the size, where the resulting image contains the largest amount of details whereas the computational errors due to the ill-determined matrix of coefficients **A** are sufficiently low. The velocities are more affected by the cell size as they are computed in the grid whilst the depths to the interface are computed only under sources and receivers. The cell size 0.5 meters is too small and the velocities are of nonsense values due to the ill-determined system of equations. The cell size 1 meter is optimal here. Even if the velocity image is fragmented, it seems to be reasonable. The cell sizes 2 meters and 3 meters are too large and the resolved interface velocities lacks desired details.



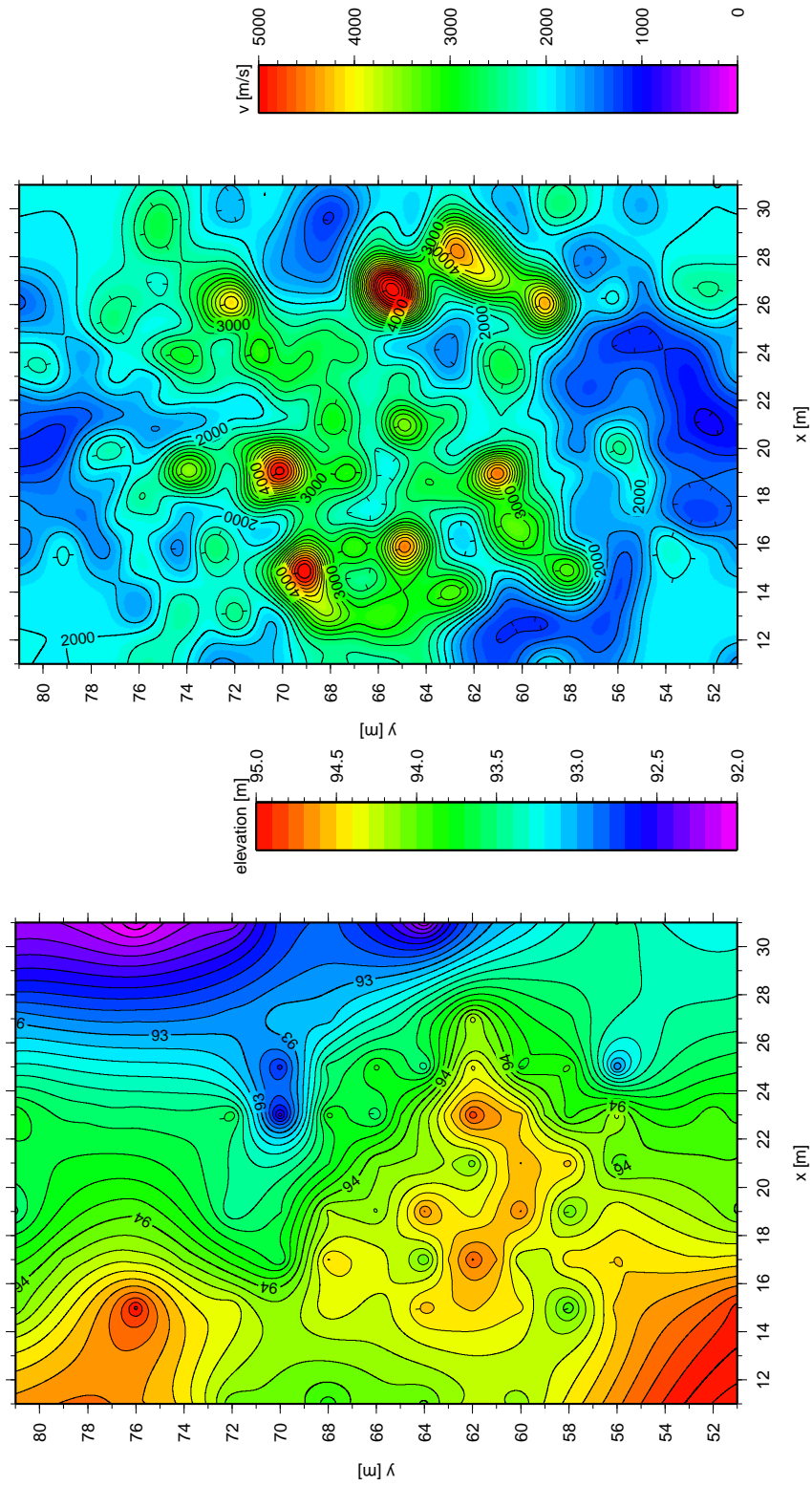


Figure 2.5: Elevation of refracting boundary and refracting boundary velocities for data set with an error of 10 % added. The computed depths are affected to only a negligible degree. Velocities of the refracting boundary are affected to a higher degree, however, the main archaeological features are still apparent.

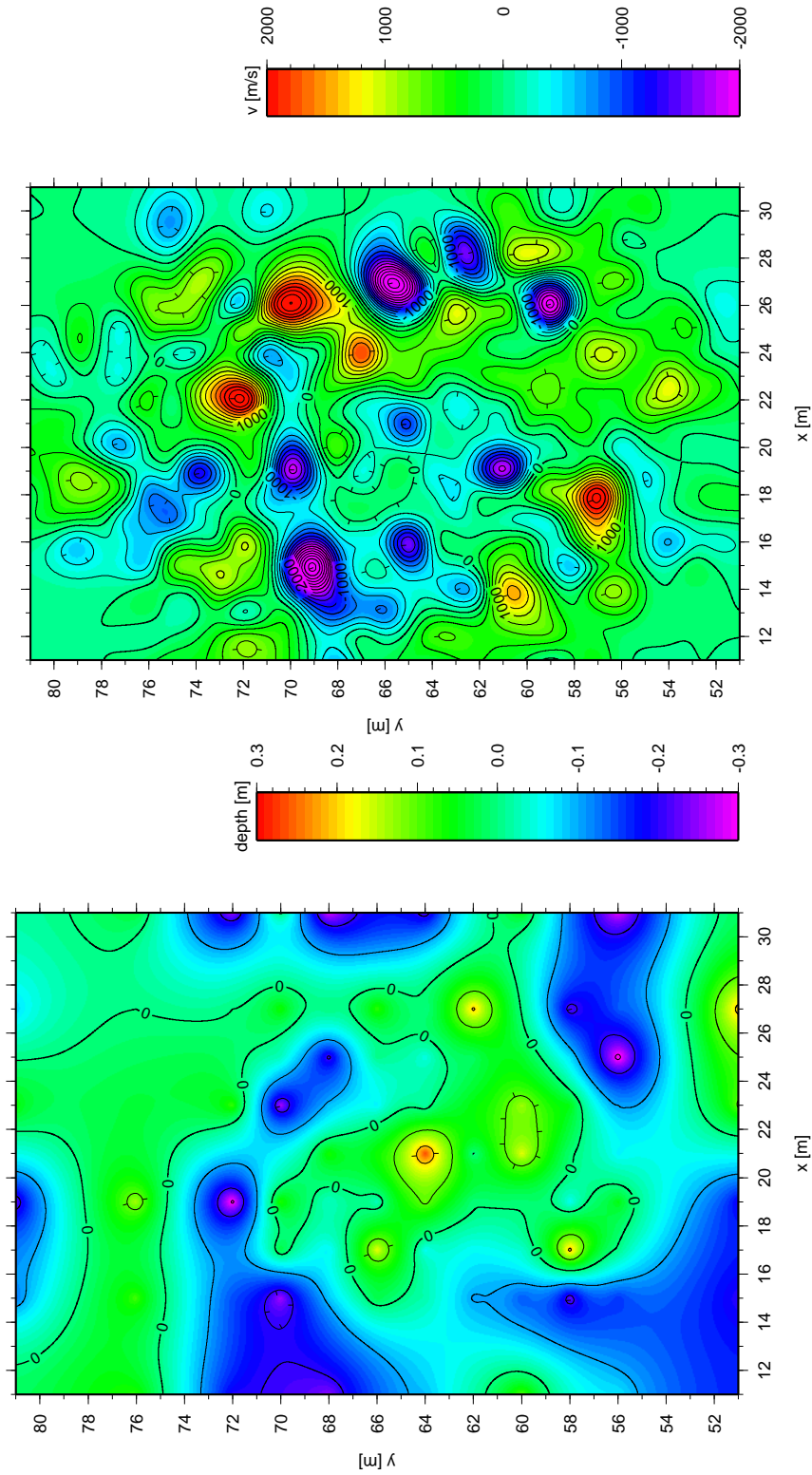


Figure 2.6: Differences in refractor depths and velocities between the original data and data with 10% error.

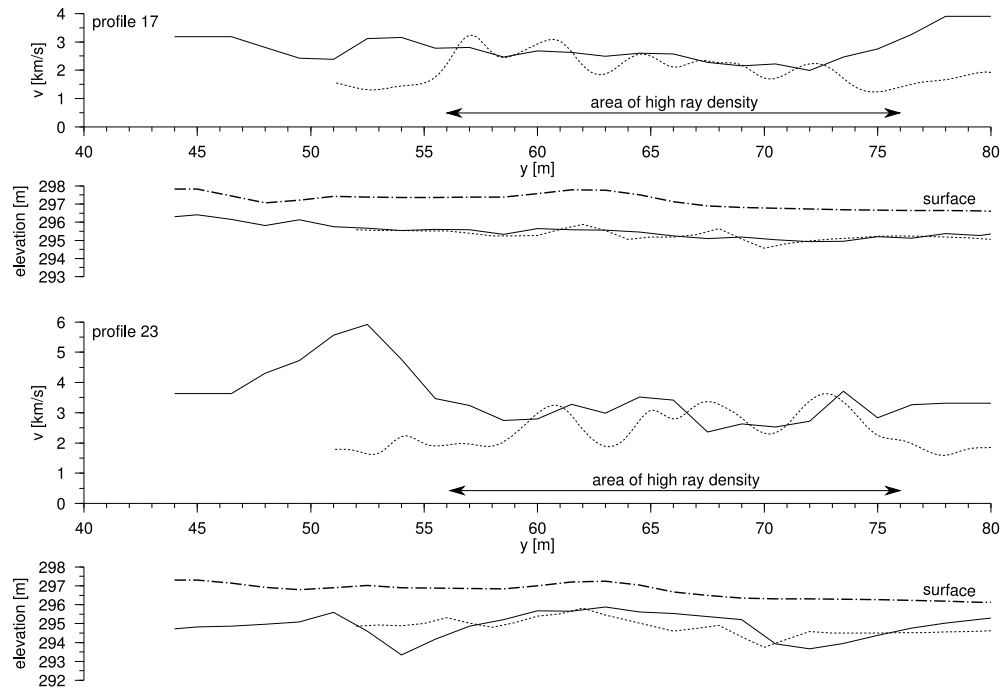


Figure 2.7: A comparison between the results of the time-term and plus-minus methods. The results of the plus-minus method are plotted in a solid line, time-term results in a broken line. A dotted line denotes the present surface. The plus-minus method was applied on a 2D measured profiles 17 and 23, the time-term method results are extracted from the gridded results of 3D survey. The depths have a good overall coincidence, the velocities coincide in the centre of the surveyed area, where the density of rays is the highest. It can be seen that the depth profiles from the time-term method are less smooth and may contain a higher number of details than the depth profiles from the plus-minus method. The high velocities around the  $y$ -coordinate 52 on profile 23 at results from the plus-minus method are most likely caused by an error.

probably ending near this place. A large depression on profile 23 around station 54 and the corresponding high velocities visualised on the plus-minus method results seem to be an error. The RMS errors for the plus-minus method are 1.444 ms for profile 17 and 1.775 ms for profile 23. The RMS error of the time-term method is 0.670 ms for the whole dataset. The complete results of the time-term method are shown in Figure 2.2.

### 2.3.3 Tomography method

PStomo\_eq algorithm by Ari Tryggvason was used for the seismic tomography (Tryggvason *et al.*, 2002; Tryggvason and Linde, 2006). This program uses finite difference calculations for travel time and time field computations (Tryggvason and Bergman, 2006). The ray tracing is performed “backwards” perpendicular to the isochrons of the time field (see Section 1.3.1). The advantage of this method is that an appropriate raypath is always found. The computations and subsequent ray tracing are thus very stable. As no S-waves were measured in this case, the input for PStomo\_eq consists only of P-wave arrival times. Smoothing during the inversion was kept as low as possible. Lower smoothing values would produce nonsensical (chaotic) models or even negative values of velocities. The RMS error of the travel time tomography is 0.930 ms, while of the time-term method it is 0.670 ms. The results of travel time tomography are shown in Figures 2.8 and 2.9.



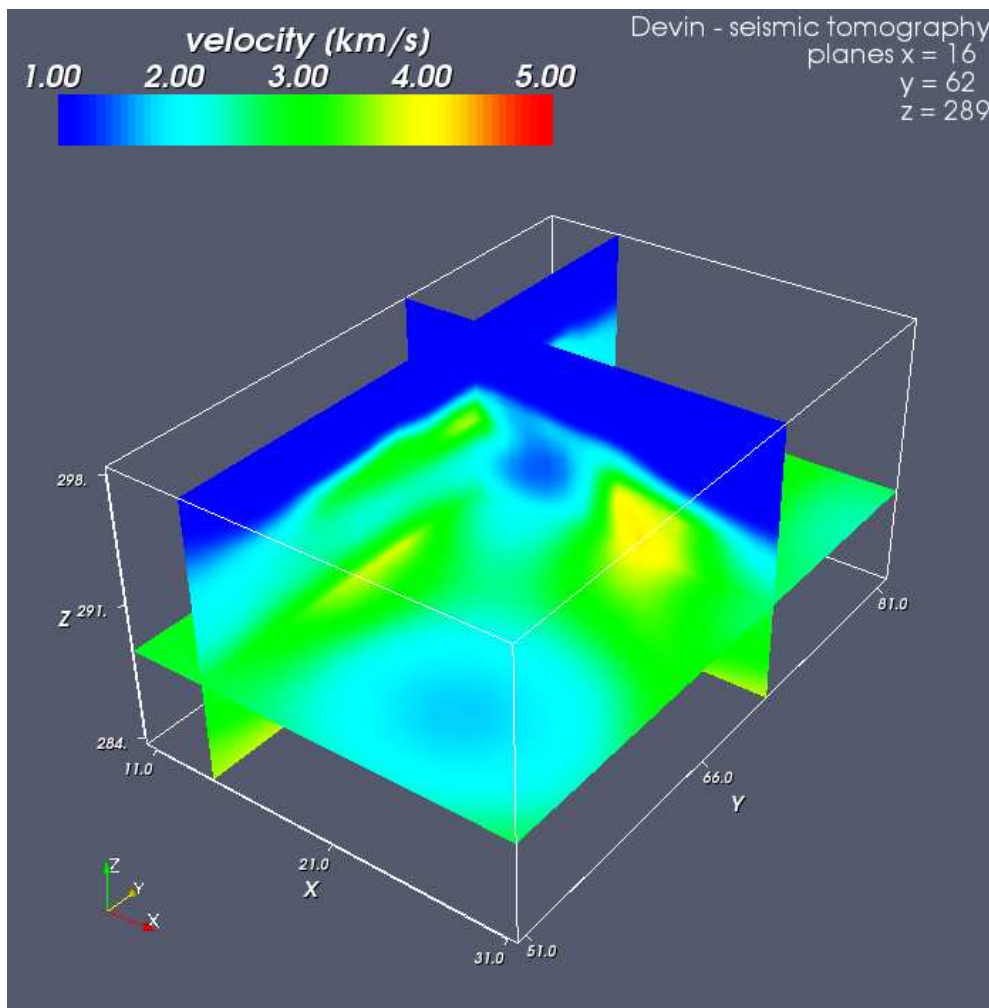


Figure 2.8: Seismic tomography – velocities of seismic waves in selected planes. High velocity anomalies represent relics of masonry, while the low velocity anomalies are most likely depressions in bedrock filled with low velocity material – soil or debris from the walls.

## 2.4 Archaeological interpretation

The interpreted ground-plan is based mainly on the time-term data processing because it offered a better resolution than the tomography method. For example, the interpreted walls are not clearly seen on the tomograms with the exception of the strengthened area at the gate. The moat, however, which is a larger structure, is clearly visible also on the tomograms.

The tomograms, on the other hand, can be used for exploring the position of the castle on the former terrain. It seems that the castle was built on a small elevation and the ramparts stood on its edge. At the place where the ramparts were built, the elevation gain was about one metre and was further rising towards the centre of the castle. The moat was already outside this elevation. The position of this elevation was probably controlled by the presence of a more resistant, less weathered part of limestones.

The interpreted ground plan of the castle and the cross-section are plotted in Figures 2.10 and 2.11. Rests of the wall with a gate and a moat are visible. The moat was about six metres wide and, according to the tomography method, three

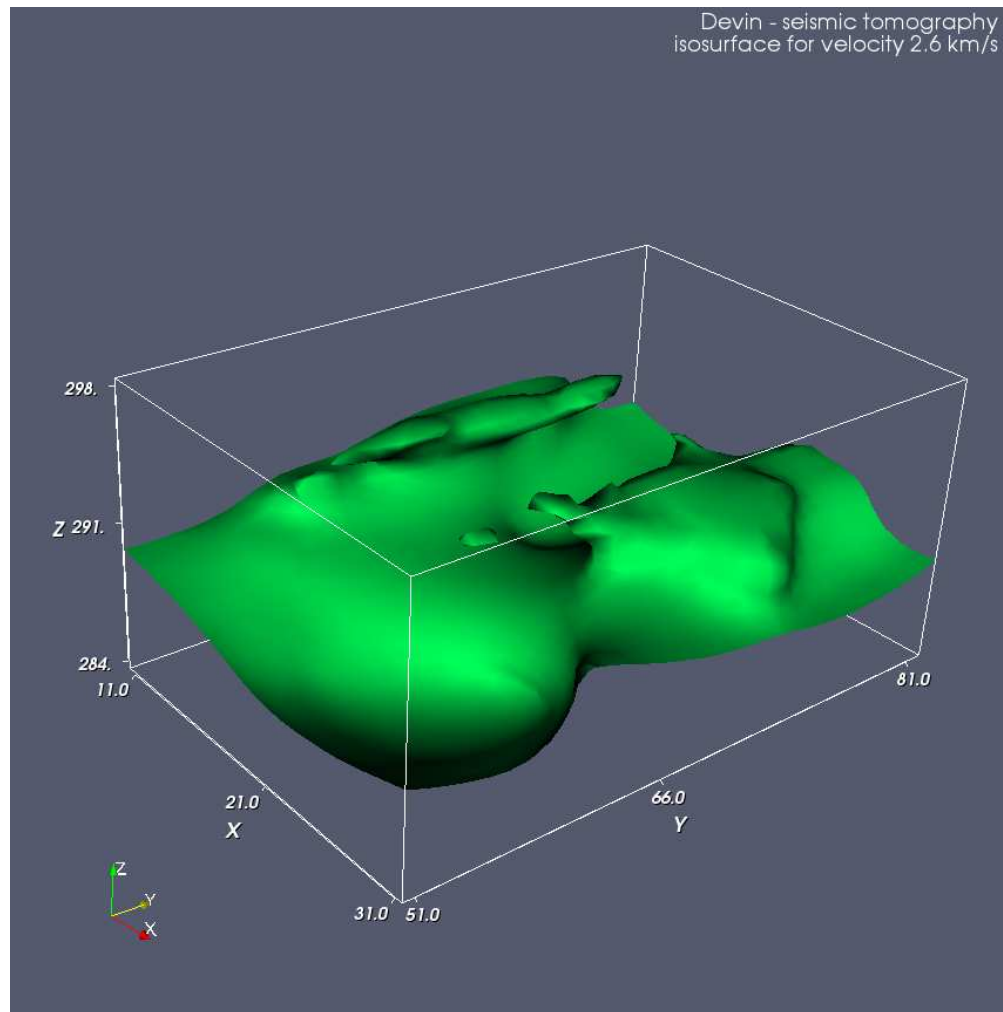


Figure 2.9: Seismic tomography – isosurface for the velocity of  $2600 \text{ ms}^{-1}$ . Elevations of the isosurface probably represent relics of walls.

metres deep. The velocities of seismic waves in the area of the moat are high (around  $3000 \text{ ms}^{-1}$ ), and this may be caused by the fact that it is filled with relics of former ramparts. It is located 5 metres ahead of the castle walls. The moat seems to have ended near the x-coordinate of 16 m, probably due to the anticipated tower the remnants of which are visible to the north of the surveyed area.

The ramparts are expressed as an elevation of the refractor, and have higher velocities than their surroundings. They were two metres thick and further strengthened on both sides of the gate. The interpreted base of the ramparts lies two metres below the former surface. A depression in the refractor and a velocity decrease were observed in the area of the gate. This may be due to the pit used to further defend the gate.

## 2.5 Comparison of time-term method and tomography

To compare between the time-term (or other layered model-based interpretation) and tomography (gradient model) methods is not easy. Pros and cons of these methods

depend mainly on geological settings at each particular locality and on the type of model needed.

The tomography method usually seeks the smoothest possible model in order to stabilise the inversion process. This might be a limitation when we are looking for subtle structures, which is the case of archaeological prospection. On the other hand, it gives a better overview of larger structures where no details are desired.

The time-term method does not need any restrictions on smoothness of the model as the inversion process is linear. Therefore, even the subtle structures can be resolved, but the price is that the resulting values might oscillate and some amount of smoothing might then be necessary. Another benefit of the time-term method is its simplicity and speed. The results are computed on the order of minutes, compared to hours needed for tomography methods.

The time-term method (or other layered-model method) should be chosen when the depth of the interface is to be resolved, because looking for interfaces in the tomography gradient model is not much precise. It also gives a better spatial resolution. The tomography, in contrast, gives information about larger part of the “cube” below the measured area. The best option is to combine both methods because they perfectly complement one another.

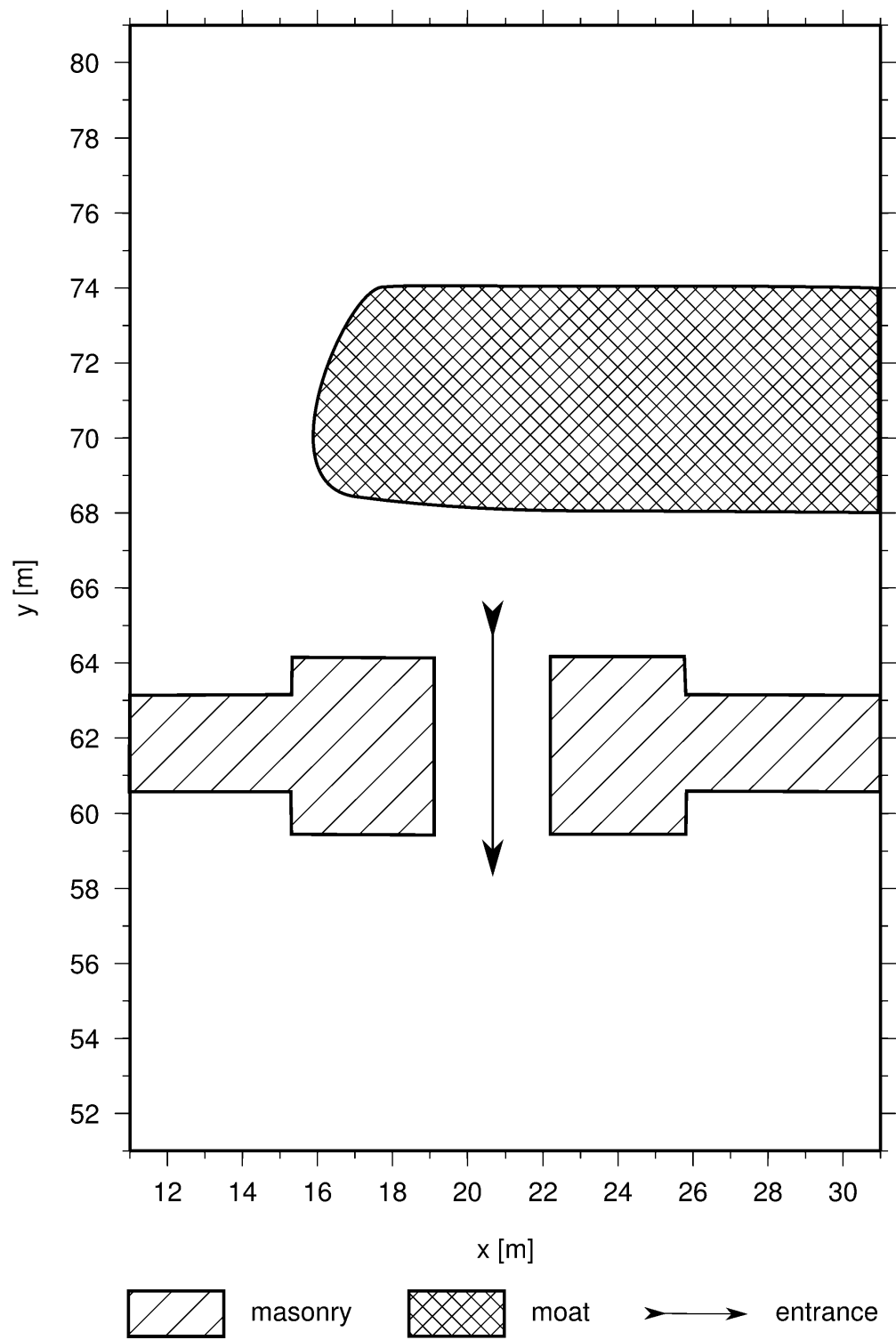


Figure 2.10: The interpreted ground-plan of the entrance to the castle Dĕvín based on all applied seismic methods.

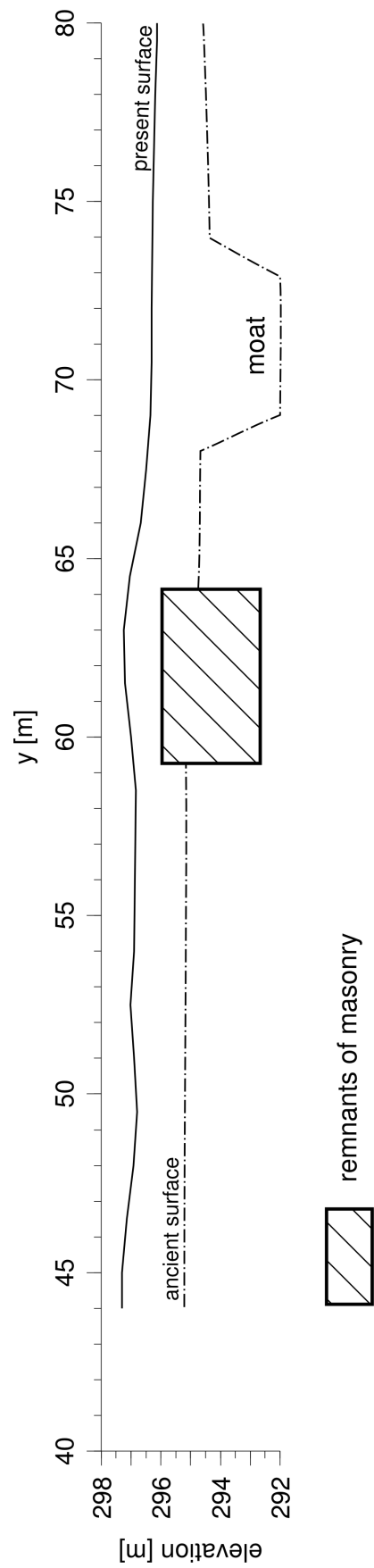


Figure 2.11: The interpreted cross-section along profile 23 based on all applied seismic methods. Plotted is the thickened base of a rampart at the side of the gate, a three metres deep moat and a possible surface from the time, when the castle was built. Note the small terrain elevation (about one metre) where the castle was built. This elevation is further rising to the centre of the castle.



---

## Fracture detection with 3D seismic refraction – Ostař Hill

The detection of fractures, their direction, density, depth of penetration and “intensity of fracturing” are the problems often tackled by near-surface geophysics. Many geophysical methods were successfully applied to solve this problem, often utilising azimuthal change in certain physical parameter. For example, a common technique in shallow seismic refraction is measurement along the profiles in different orientations. Changes of velocities of seismic waves along individual profiles allow to estimate profiles which are parallel (faster) or perpendicular (slower) to strike of the fracture system (e.g. Přikryl *et al.* 2004).

A more sophisticated methods of fracture system estimation is represented by researches based on the shear wave splitting, which is a consequence of S-wave anisotropy. This phenomenon was investigated in detail by Crampin (1985, 1999), Holmes *et al.* (2000), Vavryčuk *et al.* (2004), Vavryčuk (2005), Bates and Phillips (2000) and many others.

Recently, when the 3D resistivity tomography devices became more common, also attempts on fracture monitoring using this technique also appeared (Samouëlian *et al.* 2004; Tabbagh *et al.* 2007). However these studies are currently more or less sporadic and only in a stage of research work. The advantage of the DC tomography over the seismic tomography is in better spatial resolution of the resistivity method and hence the possibility to map also such subtle details as are the density and shape of the fracture.

In this chapter we will try to solve this problem by means of the 3D seismic refraction. The advantage of this method is, unlike methods specialised in fracture detection (some of the shear wave splitting methods), that this one also brings a detailed model of the underlying geological structure (similarly to the 3D DC tomography). In the following text, we will determine fracture orientations from the results of the 3D seismic refraction obtained by the time-term and tomography methods and compare their contributions to solving this problem.

Fractures form inhomogeneities in the rock massif, which might be further accentuated by increased grade of weathering in the near-surface zone. The weathering process essentially decreases velocities of seismic waves in the rock. If the fractures form the whole fracture systems and are oriented in certain direction (as in the case of fractures controlled by tectonic stress) then they are responsible for anisotropy of seismic waves. It should be emphasised that the wavelength of seismic waves and also the geophone step are much larger than the size of the fractures and hence the individual fractures can not be determined, as opposed to the DC tomography.

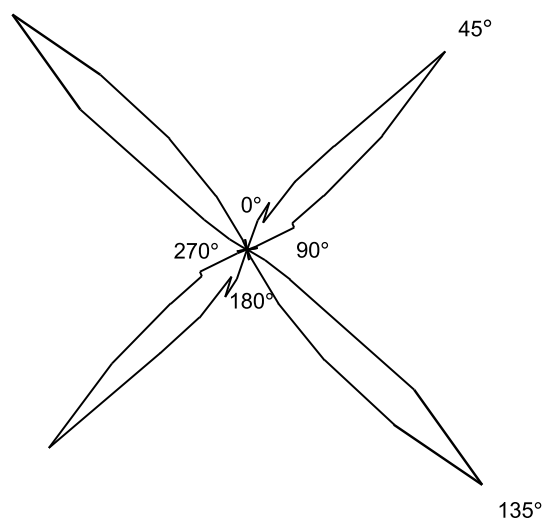


Figure 3.1: Orientation of fractures measured at the Ostaš – Kočičí skály locality. The rose diagram is based on 200 measurements. Clearly visible are the two main tectonic directions in the area – the NW–SE and the SW–NE direction. The NW–SE direction appears to be dominant. Diagram by Vladimír Stejskal, unpublished.

In case, when the fractures are localised in certain predetermined zones (e. g. zones with different mineralogical composition, structure, different parts of folds etc.) and these zones are sufficiently large (compared to the size of mesh of a seismic inversion method applied), then they can be detected directly by seismic methods. The mechanical disintegration followed by increased grade of weathering decreases velocities of seismic waves and the zones would appear as an elongated low velocity zones.

In contrast, if the zones are too small (again compared to the size of mesh of the seismic inversion) to be resolved directly, we again end up with low and high velocity zones, but as a consequence of low resolution these resolved zones might not necessarily be identical with the real ones.

### 3.1 Study area

The measured area is located in the Broumov Highland, on a plateau close to the foot of the Ostaš Hill.

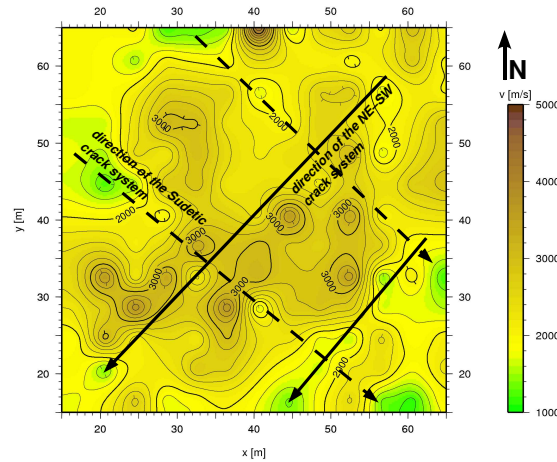
The geological environment is formed by Upper Cretaceous sediments – strata of Middle Turonian sandstones, siltstones and marlstones. Marlstones in this area lie at the top. The marlstones are overlain by quartzose sandstones forming the cliff of Ostaš and Adršpach. The strata are almost horizontal, with the maximum dip of less than  $10^\circ$ . There are two main directions of fault systems in this area, conforming with the main fault directions in the Bohemian Massif. The first one strikes NW–SE direction, while the second one is perpendicular – SW–NE. These directions also corresponds with main fracture orientations in the area. As the highland was formed mainly by tectonic stresses oriented SW–NE, faults of this strike prevail. The main fracture strikes measured in the area (Fig. 3.1) are  $135^\circ$  (NW–SE) and  $45^\circ$  (SW–NE), where the NW–SE strike, again, dominates.

### 3.2 Data acquisition and processing

The seismic receivers were distributed along two concentric circles with the diameters of 30 and 60 metres, and a sledgehammer was used as a source of seismic energy. For recording of seismic waves the three-component BR3 seismographs were used (Brož, 2000), however only the P-waves were processed in this case. The sites of the “shots” were identical with the locations of geophones and additional “shots” were deployed outside of the outer circle and inside of the inner circle. In total 13 seismographs and



Figure 3.2: Refractor velocities obtained by the time-term method. The refractor was found to be subhorizontal at depths of about 3 metres. The main joint directions are marked by arrows. At this depth, the NE–SW crack system (plotted with a solid line) is dominant and overlaps the NW–SE system (marked by a dashed line).



21 shots were deployed. This configuration enabled to reach the effective depth of the survey down to 15 metres.

Data were processed by the first arrival picking. The maximum error of reciprocal travel times was less than 5%. The picks were processed by two techniques. The first one was the travel time tomography using the FAST package by Colin Zelt (Zelt and Barton, 1998). This program uses finite difference calculations for travel time and time field computations. The ray tracing is performed “backwards”, perpendicular to the isochrons of the time field. The program uses smoothness and flatness constraints, thus seeking the smoothest and flattest model. The size of an inversion cell was 2 metres, which was the smallest cell size producing reasonable results – different starting models lead to the similar final models, the final models did not have unrealistically high or low values of velocities, etc.

The second one was the time-term method refurbished to resolve lateral distribution of velocities on the refracting interface (see Section 1.4).

### 3.3 Interpretation

The orientation of fracture systems was expected to reveal itself in the form of elongated zones of lowered velocities of seismic waves in the direction of the fractures. In contrast, in measurements of azimuthal changes of velocities, the orientation of fracture systems is indicated by azimuth with increased values of velocities of seismic waves.

From the results of the time-term method, the refractor was determined to be subhorizontal at a depth of about 3 metres. This boundary is interpreted as a layer interface between the marlstones and siltstones. The velocities on the interface (Fig. 3.2) show possible directions of low-velocity zones in NE–SW direction. The perpendicular NW–SE direction is also visible but not as distinct as the NE–SW one. It can be stated, that at the depth of approximately three metres the fractures striking NE–SW predominates and overlap the NW–SE fractures.

The seismic tomography is better suited for this type of survey, as it computes velocities in the large part of the model, in contrast with refractor depths and velocities of the time-term method. Hence also the lateral and vertical changes in the “fracture zones” can be tracked – e.g. the fading out or possible changes in direction. The cross-sections through the computed model are given in Figures 3.3, 3.4 and 3.5. The low-velocity zones, again, depict zones weakened by fracturing.

The slices (Fig. 3.5) clearly illustrates vertical changes in the fracture systems. Both fracture systems are subvertical. The NE–SW fracture system is shallow and predominates in the near-surface zone but fades out quickly with depth. It is apparent

*The geology on this locality is uncomplicated – subhorizontal layers (more or less homogeneous) of Cretaceous sediments. Thus the zones of lowered velocities can be associated with fracture systems and are probably not consequences of changes in the composition of rocks.*

*Even if it may seem that the 3D tomography computes velocities in bulk of the model, well constrained (sufficiently sampled by rays) is usually only one-third of the model. For more details see Section 1.3.*

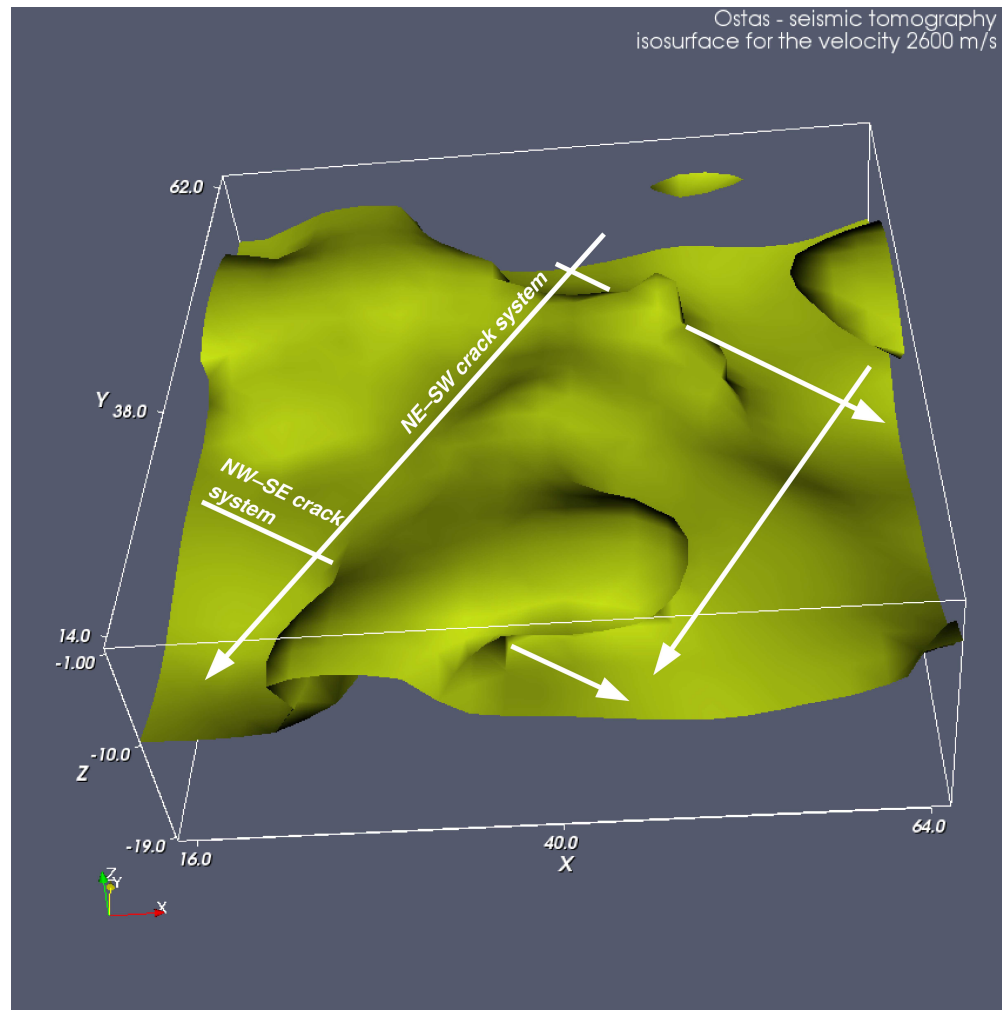


Figure 3.3: Travel time tomography – isosurface for velocity  $2600 \text{ ms}^{-1}$ . Weakened zones of individual fracture systems appear as low-velocity zones – depressions in velocity surface. It can be easily seen that the NW–SE crack system forms deeper “valleys”, and thus penetrating deeper than the NE–SW system, which, in contrast, overlaps the Sudetic system in the uppermost parts of the model.

*The velocity changes in the tomography models are rather high. They are due to low smoothing and small cell size selected for the inversion. The consequence is, that the velocity changes are easily visible but the values of velocities may not be always realistic. This is a common ambiguity between the resolution and reliability and one has to be aware of it when interpreting the results.*

down to the depth of approximately 9 metres. In the deeper parts of the model, it is overridden by the Sudetic NW–SE fracture system.

Moreover, the seismic tomography provides us also with a detailed model of the subsurface in addition to the fracture information emphasised here. For example, in this particular survey, the velocities in the uppermost zone are relatively high – reaching  $1000 \text{ ms}^{-1}$  at the depth of one metre without the presence of a steep velocity gradient. Such situation usually occurs when chemical weathering of rocks is not present or is weak and the rock is a subject to disintegration by frost action or other mechanical processes. The predominance of mechanical disintegration over chemical weathering also well corresponds with the composition of sediments and climate of the locality.

To test the correctness of these results we can utilise an already mentioned method of measurements along profiles with different orientations and look for the seismic anisotropy as another proof of the presence of fracture systems. We can benefit from the fact that the refractor was found to be subhorizontal. Therefore the values of apparent velocities are significantly affected only by changes of seismic velocities of the

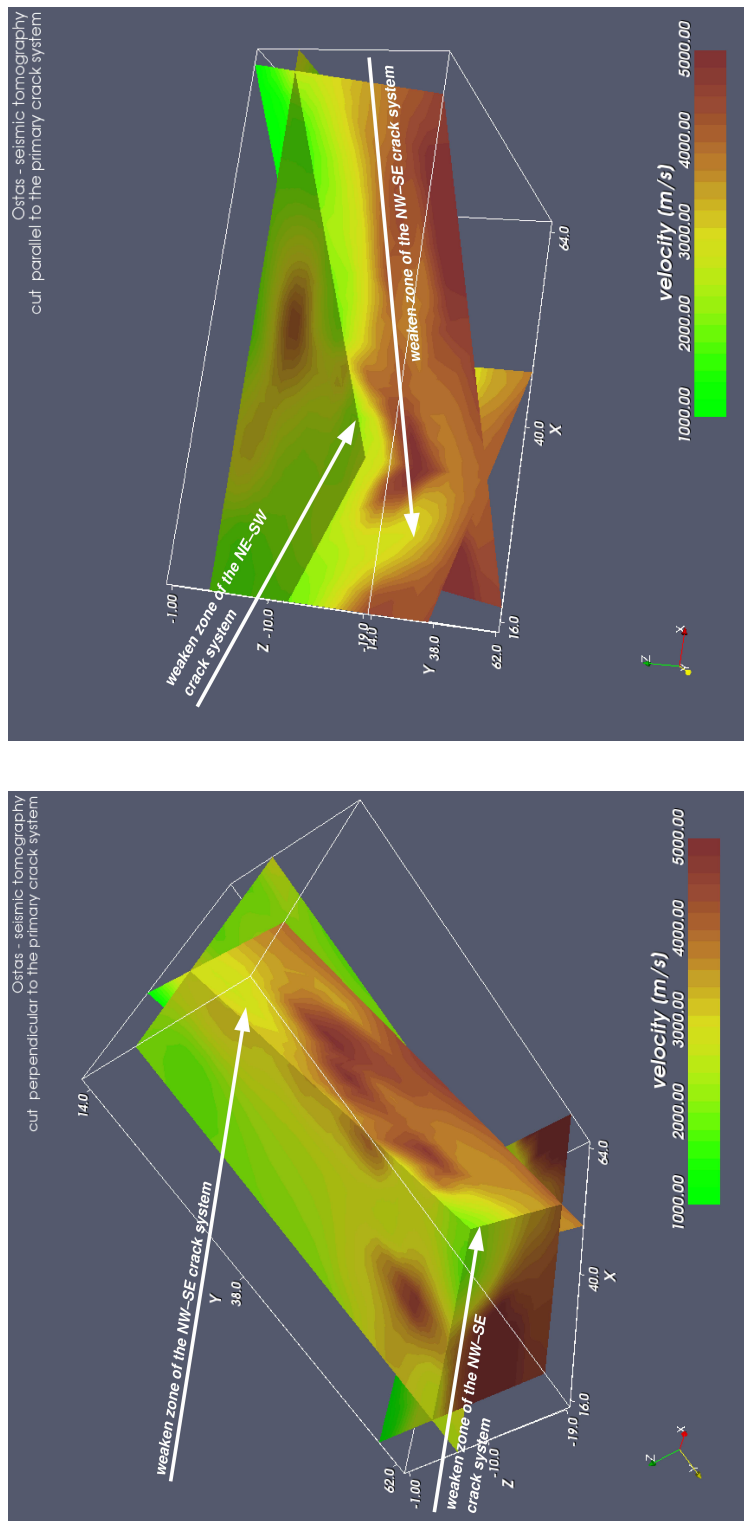


Figure 3.4: Travel time tomography – weakened zones of individual fracture systems. The NE-SW fracture system is considerable only near the surface. But it has a low depth reach and significantly penetrates only to a depth of 7–9 metres. The primary NW-SE fracture system penetrates deeper, at least to the depth of 15 metres, which is the effective depth of this survey.

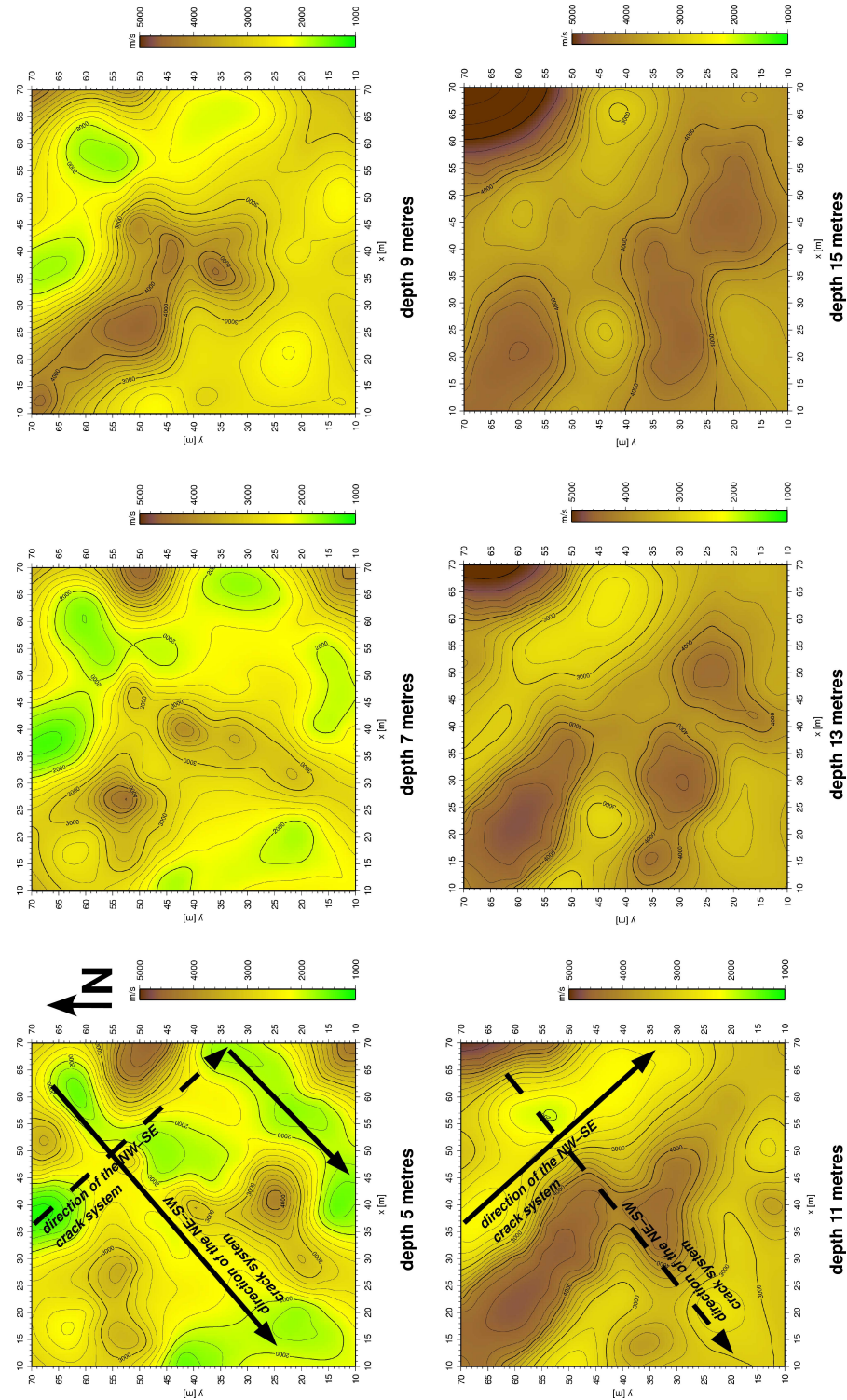


Figure 3.5: Travel time tomography. Slices at different depths. It can be clearly seen that both fracture systems are subvertical. The NE-SW fracture system fades out with depth, but overrides the NW-SE fracture system at shallow depths.

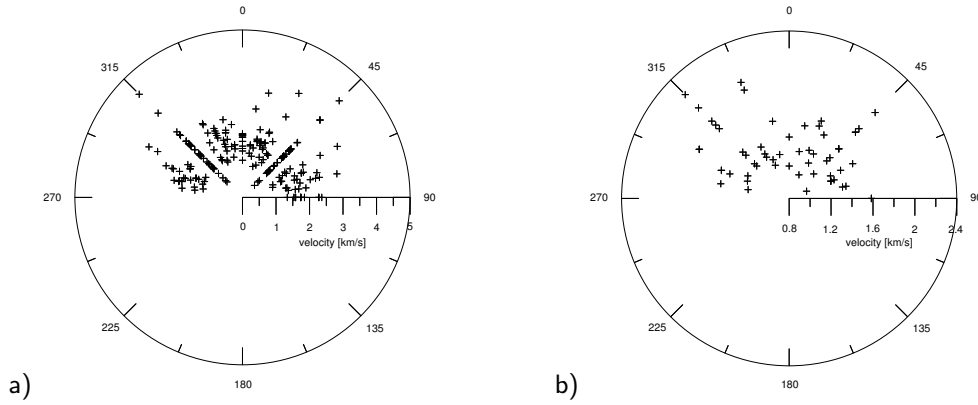


Figure 3.6: Azimuthal distribution of apparent velocities: a) apparent velocities for all source-receiver pairs and for the source-receiver pairs, b) where the source-receiver distance ranges between 20 and 30 metres. Both graphs show two directions of increased velocities –  $45^\circ$  (NE–SE) and  $315^\circ$  (NW–SE).

media and not by the changes in slope of the interfaces. Thus we can use the azimuthal changes of apparent velocities as an indicator of seismic anisotropy, similarly to the measurements along profiles with different orientations.

The apparent velocities for all source-receiver pairs were computed and are plotted in Figure 3.6 a). The figure clearly depicts two directions with increased values of apparent velocities –  $45^\circ$  (NE–SE) and  $315^\circ$  (NW–SE). These directions corresponds to the directions of fractures measured on outcrops (Fig. 3.1).

Because the rays involved in Figure 3.6 a) travel through different depth levels in the media, the source-receiver pairs where the source-receiver distance ranges between the 20 and 30 metres were selected and are plotted in Figure 3.6 b). The rays connecting source-receiver pairs in the latter figure are affected by structures in roughly the same depths and thus corresponding apparent velocities should be comparable. Figure 3.6 b) again clearly depicts the same faster directions –  $45^\circ$  (NE–SE) and  $315^\circ$  (NW–SE) which is in a good agreement with results derived from the 3D interpretations.

### 3.4 Conclusion

The 3D seismic tomography was proved to be able to map fracture systems (or better, the weakened zones) in the near-surface zone, even if two overlapping fracture systems are involved. The mapping of fracture systems can be carried out even without *a priori* information about the fracture orientations. However, it is necessary to respect the limited resolution of seismic waves and hence the limitation of the whole survey, as is discussed at the beginning of this chapter.

It is clear, that specialised techniques, e.g. those based on anisotropy measurements, can give more precise and detailed information about the structure of the fractures. On the other hand, the 3D refraction, without any additional measurements, can also produce a detailed model of the geological structure, which is also a valuable piece of information.



---

## Determination of S-waves

Up to this point, we only considered P-waves to enter into the interpretation process. However, the P-waves form only a small part of the field records. And with more information entering the inversion process, we can obtain more accurate results. This is vital mainly in a global seismology, where relatively low amount of data is available to resolve large portions of the Earth structure. The seismic record is analysed into the smallest details (like reflections from different interfaces, P/S waves conversions etc.), and all these data enter the inversion process simultaneously. Usually, there is no need for such a detailed analysis in the near surface geophysics, as the data collecting is relatively easy and thus a sufficient amount of data is usually available. Therefore, the data processing is usually reduced to first arrival picking and P-wave interpretation.

However, there are many applications where the more detailed information about rock massif (and not solely P-velocity model) is needed. In hydrogeology, for instance, a porosity and fracturing of rocks play the key role. In geotechnics, the stress state of the rocks is of significant importance. The Lamé parameters  $\mu$  and  $\lambda$  (or the  $E$  and  $\sigma$  parameters) are used when evaluating bedrock state for constructions. For these applications, the classical P-wave velocity model have to be extended to the PS-waves model.

The ratio of the P-wave and the S-wave velocities is a very important parameter. For example, the depth of the water table can be observed as a change in the velocities ratio: the velocity of P waves increase in water-saturated rocks, while the shear wave velocity remains nearly the same in such rocks. This ratio can also help in the determination of fluid saturation in porous media, clay content and a number of other parameters. However, even if the joint interpretation of the P- and S-waves gives generally more accurate results than the interpretation of P-waves solely, it is not routinely used, because it is not easy to identify S-waves on the near-surface records. This problem arise due to the short source-receiver distance and, consequently, too small time separation of different wave types there. Even the unusually high P/S velocity ratio (2 and more) in the uppermost layers do not have sufficient effect on the P- and S-wave separation. What appeared easy in the global seismology, where the S-waves were easily identified on the seismograms, is not possible here.

A lot of techniques for separation of different wave types was developed mainly in the “oil seismics”; the majority of them are based on the polarisation analysis of multicomponent records. However, the polarisation analysis is not always successful with the near surface data. Moreover, some of these methods need *a priori* information

*It is a rather often encountered problem (the present author not being an exception), that methods used with success in a deeper seismics (oil prospection) for a long periods of time fail unexpectedly in a near surface seismics. The author believes that the reasons for such a common failure are twofold: first, in a near surface data, the wave types are divided by too a small time separations and, second, the near-surface seismograms often encounter way more of a high-frequency noise than deeper seismograms. In consequence, the polarisation analysis is unable to “distinguish” individual overlapping waves.*



about the geological environment, or, alternatively, they are restricted to certain wave types.

One of the first who tried to separate different wave types was Flinn (1965): he used statistical methods to carry out the polarisation analysis – extracting ellipticity and directionality from multicomponent records. Ellipticity represents a surface of an ellipsoid, which is an approximation of the particle motion trajectory in a certain time window. Ellipticity, in combination with a directionality (direction of the particle motion with respect to the desired arrival angle), can be used for filtering of different wave types. A polarisation analysis has been further developed by many others; for a neat summarisation see Perelberg and Hornbostel (1994).

Dankbaar (1985) introduced a filter in the  $f$ - $k$  domain for the separation of P- and SV-waves registered by a two-component geophone. However, this filter requires corrections for geophone receiving characteristics, which are influenced by Poisson's ratios. The receiving characteristics are independent of frequency; they are determined by P- and S-wave velocities only. On the other hand, the necessity of the estimation of P- and S-wave velocities and a need to know the receiving characteristics of a particular geophone are the drawbacks of this method.

By comparison, the advantage of the method proposed by Cho and Spencer (1992) is that one does not need any *a priori* information. The individual parameters (polarisation angle, apparent slowness and phase difference between the receiver components) can vary with frequency. However, as pointed out by Richwalski, Kabir and Jaap (2000), the application of this method is not straightforward.

In current research, there seem to be two methods for determination of S-wave velocities in near-surface seismics. The first one is based on identifying the S-waves arrivals and then – using the same methods as in the P-wave – the consequent determination of the velocity profile. The second method, often called SASW (single component analysis of surface waves) or MASW (multicomponent analysis of surface waves), is based on extraction of surface waves (most often the Rayleigh ones), determination of the dispersion curves and inversion of dispersion curves to obtain S-wave velocities (e.g. Gaždová and Vilhelm, 2006; Kolínský and Brokešová, 2007; Turesson, 2007; Villaseñor *et al.*, 2001 and many others).

The former method (identification of the S-waves on seismograms) is older and it suffers from all the problems common to the S-waves identification methods mentioned above. On the other hand, the methodology for determination the velocity profiles is well developed and even joint inversion of P- and S-waves is possible. The data processing can be done in 1D, 2D, 3D, or even in four dimensions.

The latter method, in contrast (multicomponent analysis of surface waves) does not suffer from problematic identification of S-wave onsets. The surface waves are the strongest waves on the seismograms, they are well generated by all used source types and in the case of Rayleigh waves, even single component vertical geophones can be used for detection. This is the reason of the increasing popularity of this method in the engineering geophysics in the current research. Still, nothing is only black or white, so, this method has its limitations as well. The major drawback in my opinion is the fact that the data processing is, at least in the near-surface prospection, carried out only in one dimension for the transversally isotropic media. The lateral changes of velocities are often solved by higher number of 1D models. Even if a global 3D velocity models from the surface waves are presented by Ritzwoller (e.g. Ritzwoller *et al.*, 2001), the important considerations about the depth of penetration of the particular frequencies of surface waves are simplified. Moreover, this approach did not find its way into the near-surface geophysics. Furthermore, the determination of the dispersion curves might be difficult.

More importantly, these two methods do not provide corresponding results. It is clear that both wave types (surface waves and S-waves) travel through the media differently and hence they “see” different features and, consequently, the velocities



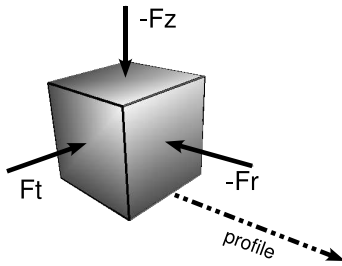


Figure 4.1: Layout of elementary forces. Vertical ( $Fz$ ), radial ( $Fr$ ) and tangential ( $Ft$ ) forces. The minus sign indicates reversed orientation of the force with respect to the coordinate direction.

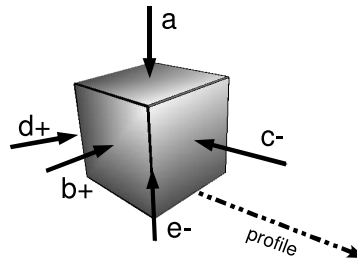


Figure 4.2: Orientation of possible hammer strikes. The letters  $a$  to  $e$  denotes seismograms generated by relevant strike. Strikes for seismograms  $a$ ,  $b$  and  $c$  coincide with the directions  $Fz$ ,  $Ft$  and  $Fr$ . Strikes of general orientations generates seismograms  $d$  and  $e$ .

determined by these methods must vary. But the resulting profiles should be – at least – similar or consistent in resolved structures. However, as can be seen e. g. from results published by Anita Turesson (2007), this is not the case, or, at best, not necessarily the case. Unfortunately, the mentioned article does not offer neither a discussion, nor a possible explanation of this phenomena.

In the following text, we will concentrate on the first method of S-wave velocities determination: the direct identification of the first arrivals of the S-waves. Furthermore, two methods of S-wave extraction will be discussed here. The first one is a traditional method of oriented sources, or polarity reversals – reversal of polarity of S-waves with simultaneous reversion of the direction of the source. The second one is a method of filtering an individual wave type based on their similarity on the neighbouring records. Finally, a field example of S-wave separation will be presented.

## 4.1 Oriented sources – SH and SV-wave separation

There is a classical method for S-waves registration used for few past decades based on polarity reversal of S-waves with reversing the direction of the source (e. g. Schenk and Růžek, 1981; Sheriff and Geldart, 1995). In the near-surface geophysics, this is accomplished by striking a horizontal bar with a sledgehammer from opposite sides. This generates S-waves with reversed polarity, while the polarity of P-waves remains the same. Consequently, a simple sum and subtraction of seismograms allows to separate P- and S-waves. This method may also be used with explosive sources or vibrators. However, the use of oriented sources – usually more expensive and more time consuming than the usage of simple sources – is simultaneously a main drawback of this method. Moreover, in the case of near-surface geophysics which utilises hammer blows, the oriented source produce considerably lower energy than the conventional one.

In the original version of this method, the goal was to identify S waves irrespective of their type. For the studies of anisotropy, it is essential to determine also the wave type – to distinguish between SV and SH waves. Even if the original version theoretically enabled determination of SV and SH waves, it needed high accuracy in orientation of hammer strikes, which is not always easy to accomplish. However, we have extended the method and now the lower accuracy can be compensated by higher number of measurements. To compensate for errors in strike orientation, higher number of strikes in different directions are needed. The error in orientation is then reduced by averaging. The side effect of this method is also the noise reduction.

*The discrepancies found in the results produced by surface waves and body waves method can be, in author's opinion, a consequence of the seismic anisotropy which, in the near-surface conditions, can reach the order of tens of percents, but which is often neglected.*

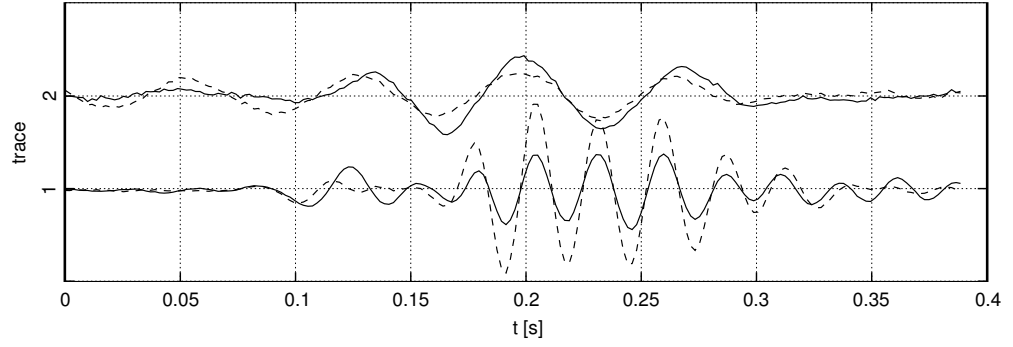


Figure 4.3: Comparison between traces obtained by summation of seismograms from strikes of opposite directions ( $c^+ - c^-$ ) in a dashed line and of strikes of six different orientations ( $c^+ - c^-$ ,  $d^+ - e^-$ ,  $d^- - e^+$ ) in a solid line. Trace 1 depicts a case of good S/N ratio and a proper orientation of initial forces. The difference in S-wave amplitudes is not substantial in this case (at least for the first arrival determination). Trace 2 depicts a case where less favourable conditions are encountered; still, the summation of more seismograms leads to usable results.

Force of any hammer strike can be decomposed to elementary forces in the directions of principal axes. Let us call these elementary forces  $Fz$ ,  $Fr$  and  $Ft$  for vertical, radial and horizontal axes force respectively (Fig. 4.1). The profile forms the  $y$  axis of the coordinate system, the  $z$  axis vertical pointing upwards and the  $x$  axis perpendicular to the profile forming the right-handed coordinate system. The force oriented in the direction of the coordinate system, where the profile is one of its principal axes, is denoted with the “+” sign. The force with opposite directions with respect to the coordinate system, is denoted with the “-” sign. In a laterally homogeneous media in the far-field in the direction of profile, the  $Fz$  generates P-waves and SV-waves,  $Ft$  produces SH-waves and  $Fr$  produces SV-waves and P-waves (Aki and Richards, 1980). However, a laterally homogeneous media is only rarely found in the field and thus – due to an inhomogeneity of the media and a coupling between the modes – there will be a motion on all the ZNE components of the receiver for any direction of the source. In the following text, it is always assumed that the Z component of the receiver is vertical, the N component is horizontal and in the direction of profile, and the E component is horizontal and perpendicular to the profile.

The seismograms with possible directions of hammer strikes are denoted by letters from  $a$  to  $e$  in Figure 4.2. Seismograms  $a$  to  $c$  are caused by the strikes in direction of elementary forces. Seismograms  $d$  and  $e$  represent strikes with general orientations. The “+” and “-” signs have the same meaning as in the case of the forces. It is clear, that any strike force can be expressed as a vector sum of elementary forces  $Fz$ ,  $Fr$  and  $Ft$ . Then, any seismogram can be expressed as a sum of “elementary” seismograms generated by elementary forces. This can be written as a set of equations:

$$\begin{aligned}
 a^+ &= k_{11} g(Fz) + k_{12} g(Ft) + k_{13} g(Fr), \\
 b^+ &= k_{21} g(Fz) + k_{22} g(Ft) + k_{23} g(Fr), \\
 b^- &= k_{31} g(Fz) - k_{32} g(Ft) - k_{33} g(Fr), \\
 c^+ &= k_{41} g(Fz) + k_{42} g(Ft) + k_{43} g(Fr), \\
 c^- &= k_{51} g(Fz) - k_{52} g(Ft) - k_{53} g(Fr), \\
 d^+ &= k_{61} g(Fz) + \sin \alpha k_{62} g(Ft) + \cos \alpha k_{63} g(Fr), \\
 d^- &= k_{71} g(Fz) - \sin \alpha k_{72} g(Ft) - \cos \alpha k_{73} g(Fr), \\
 e^+ &= k_{81} g(Fz) - \sin \alpha k_{82} g(Ft) + \cos \alpha k_{83} g(Fr), \\
 e^- &= k_{91} g(Fz) + \sin \alpha k_{92} g(Ft) - \cos \alpha k_{93} g(Fr),
 \end{aligned} \tag{4.1}$$

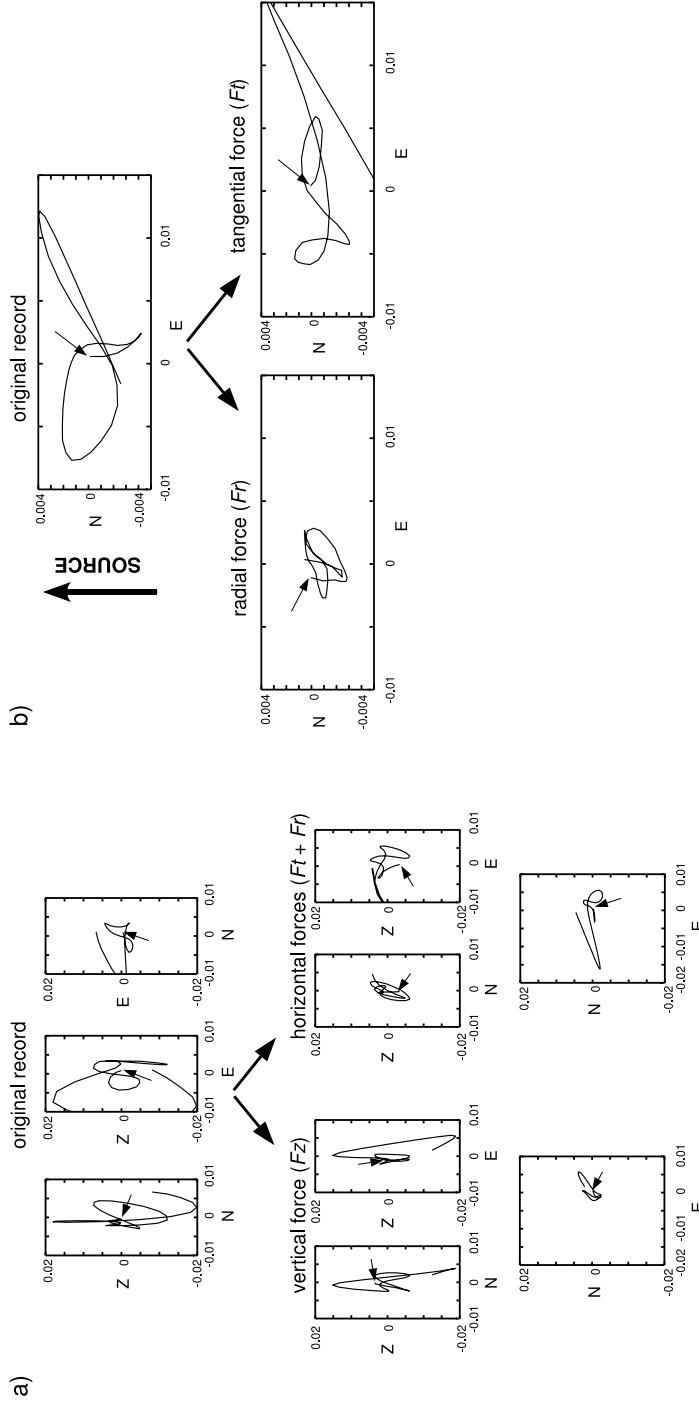


Figure 4.4: Particle motion diagrams illustrating the decomposition of a seismogram to its components caused:  
a) only by the vertical force ( $F_z$ ) and by the horizontal forces ( $F_h, F_r$ ). The N direction is oriented towards the source, thus parallel to the direction of the radial force  $F_r$ . The onset of the S wave is indicated by an arrow.  
b) by the horizontal forces ( $F_h, F_r$ ). The N direction is oriented towards the source, thus parallel to the direction of the radial force  $F_r$ . The separation to the  $F_r$  and  $F_t$  components is not absolute, but still significant. The onset of the S wave is indicated by an arrow. The data are from the locality Kobylysy.

where  $k_{ij}$  are parameters depending mainly on the strike power of individual strikes,  $\alpha$  is the angle between the strike direction and profile and  $g$  are Green functions – seismograms caused by unit force in certain directions. The parameters  $k_{ij}$  depend on the strike power, on the transfer of energy from the bar to the ground and from the ground to the geophone etc. and they are changing for every strike. Hence, it is not possible to determine them quantitatively. But after proper normalisation, when we obtain seismograms generated by the same (or similar) energy, their influence is diminished and they might be omitted. In this case, corresponding terms ( $Ft$  and  $Fr$ ) in  $b^+$  and  $b^-$ ,  $c^+$  and  $c^-$ ,  $d^+$  and  $d^-$ ,  $e^+$  and  $e^-$  are of the same value, but of an opposite sign. The underlined terms in  $b$  and  $c$  seismograms are zero in (first) a laterally homogeneous media and (second) when the orientation of a strike to a profile is absolutely accurate. The  $b$  and  $c$  are the seismograms obtained by parallel and perpendicular strikes in the original version of this method. Unfortunately, as said above, an absolute accuracy is clearly impossible, as the real strikes are more or less of general orientation.

After normalisation (when the influence of  $k_{ij}$  parameters is ignored), individual Green functions  $g(Fz)$ ,  $g(Fr)$  and  $g(Ft)$  can be obtained by summing or subtracting seismograms of individual strikes. For instance, subtracting  $e^-$  from  $d^+$  results in a seismogram generated by an  $Fr$  force and thus in SV waves. The most commonly used polarity reversals configuration – subtracting  $b^-$  from the  $b^+$  (strikes perpendicular to the profile) should cancel out the P-wave ( $Fz$  term) and leave the mixture of  $Fr$  and  $Ft$  terms, where the  $Fr$  term should be negligible. Similar considerations apply in the case of subtracting  $c^-$  from the  $c^+$ .

As should follow from the discussion, this method suffers from two basic problems. The first problem are variations of the strike power and thus variations of the parameters  $k_{ij}$ . To minimise these effects, a normalisation of seismograms reduces influence of parameters  $k_{ij}$ . After series of tests, the normalisation on “sum of the absolute values” of seismograms (the norm  $l_1$ ) appears as the best in most cases.

The other important problem is the low energy generated by horizontal strikes. To some extent, this problem can be circumvented as well by increased number of strikes; however, this method is usually applicable only in distances in order of tens of meters.

A comparison of this method with its original version is in Figure 4.3. Two seismic traces are depicted here: the first one with a good S/N ratio, the second one with a low S/N ratio. Whereas in the case of a high S/N ratio, the localisation of the S-wave onset is easy on both methods (as expected), in the case of a poor S/N ratio (trace 2), the original method (using only two opposite strikes) does not lead to acceptable results. In contrast, adding strikes in other directions as well, the S-wave onset is clearly visible at about time 0.088 seconds. This figure thus depicts both benefits of the modified method – the reduction of mistakes in an orientation of the strikes and the noise removing effects obtained by a higher number of summed shots.

A decomposition of seismograms into their  $Fz$ ,  $Fr$  and  $Ft$  components is illustrated using a particle motion diagram in Figure 4.4. Two examples from the survey at Kobylisy are provided on this picture. The first one depicts a decomposition to the P-wave and S-waves (irrespective of the type of S-waves). The P-wave (at the particle motion diagram illustrating vertical force  $Fz$ ) is well-filtered and after such a filtration, there almost is not a movement in the horizontal NE plane. The amount of vertical movements for the horizontal  $Fr$  and  $Ft$  forces is also well reduced.

The second example in Figure 4.4 depicts a decomposition of the records into individual waves generated by a single horizontal force  $Fr$  and  $Ft$ . Only diagrams for the horizontal NE plane are plotted. The radial force  $Fr$  should produce SV-waves and thus a motion in the N direction. In contrast, the tangential force  $Ft$  should produce SH-waves and a motion in the E direction. From the diagrams, the both types of S-waves seem to be well separated.

## 4.2 Generalised average for identification of S waves

Another possibility of separation of individual wave types is to filter them accordingly to their similarity on the neighbouring records. If we shift neighbouring records accordingly to the travel time curve of the desired waves and sum them, the desired wave should be amplified whilst the others weakened. When the traces are shifted correctly, the filtered wave type should be on the same time on the summed traces. When the distances between traces are not too large, the wave forms should be similar and coherent. Depending on the travel time curve used (P, SV, SH etc.), different wave types can be amplified while the others are weakened.

Alternatively, if the P- and S-wave time separation (or of any other wave type) is too low – or, possibly, the undesired wave too strong – and thus could not be filtered by shifting the desired waves into the common time, an “inverse” approach might be used. The necessary condition is that the investigated part of the seismogram must be not too complex. Looking at the first onsets of S-waves, this condition is often satisfied. The S-wave onsets are usually obscured only by some incarnations of the P-wave (refracted waves and, possibly, also direct waves, reflected waves or converted waves etc.). Hence, if we shift the seismograms in time so that the P-wave(s) sum destructively, they are filtered out. In this shift, the S-wave will not sum as destructively as the P-wave and thus will not be filtered out completely, so in the effect we would get (smoothed) S-wave. Of course, this approach cannot work for the late phases where there are many different wave types overlayed and even cancelling one of the wave types would not simplify the resulting seismogram enough. However, as pointed above, for the first onsets (which are not obscured by too many different wave types), this “inverse” approach works (see examples at the end of this chapter).

The problematic part of this approach is that we need a filter with strong filtering capabilities which, moreover, takes into account different phases of the waves. A simple linear summation – linear stacking – might be considered one of these filters. In the linear summation procedure, simple arithmetic sum (sample after sample) from all seismograms is computed. If all  $n$  seismograms contains the same signal, then this signal is emphasised  $n$ -times, while the non-coherent noise is emphasised only  $\sqrt{n}$ -times. Hence, the signal to noise ratio is  $\sqrt{n}$ -times improved.

Unfortunately, the filtering capability of a simple linear stacking is not powerful enough for our purposes. Fortunately, however, we could use the non-linear one, where every sample entering the summation is weighted according to some suitable criterion. This criterion might be based on any property where the signal and noise are different – frequency, polarisation, a shape of the signal, etc. A simple example of a non-linear summation is an application of a band-pass frequency filter to each seismogram before summing. If the frequency of a weak coherent signal fits the band of the filter, it can improve the signal to noise ratio considerably. The drawback of the non-linear summation is that it does not preserve the shape of the signal.

A possible approach to the non-linear summation might be the phase weighted stack (PWS) designed by Schimmel and Paulssen (1997) and further developed in Schimmel (1999) and Schimmel and Gallart (2003). It is based on the assumption that the instantaneous phase of the noise is different from the instantaneous phase of the signal. The computation of weights is based on a comparison of instantaneous phases of individual signals (seismograms). It is rather unfortunate, then, that even the PWS is not powerful enough for filtering of individual wave types for our purposes. But the basic idea (computation of weights based on the instantaneous phase) can be further developed and widened, so that it would involve also the amplitudes. Precisely this is the base of the generalised average of signals (GAS) method developed by Málek (Málek *et al.*, 2007). We will discuss it in details in the following section.

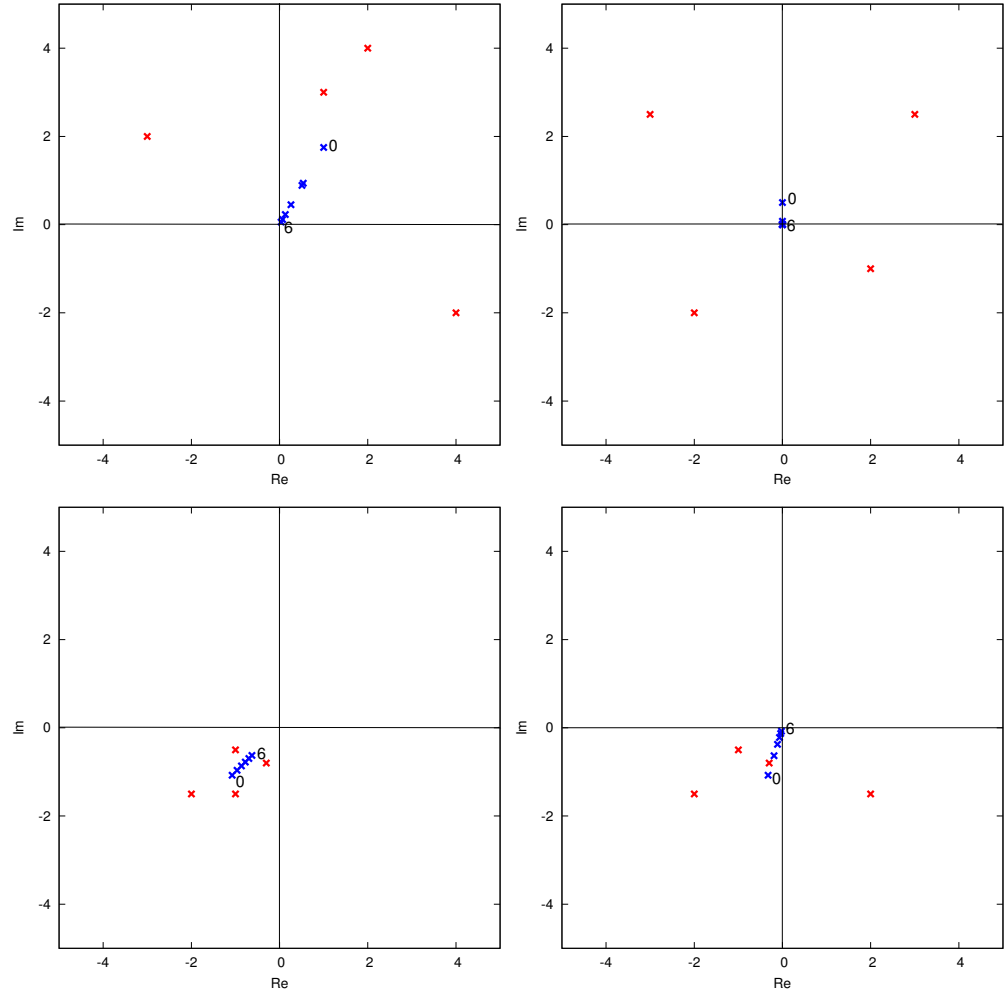


Figure 4.5: Generalised average of complex numbers (measurements). The red crosses depict the four complex numbers, while the blue ones represent generalised averages of different orders. The order  $p$  of the average increases from 0 to 6 and for the first (0) and the last value (6), it is written next to the cross. For measurements with different amplitudes and phases (noise, or erroneous measurements), an average rapidly decreases with increasing order  $p$  to 0 (the top two graphs). If the measurements are close (so they have similar phases and amplitudes), the higher orders decrease much more slowly (the bottom left graph). Finally, if we have three similar measurements and one clearly wrong (the graph in the bottom right corner), the generalised averages also “identify” and “remove” this set by reducing the average.

### 4.2.1 Generalised average of signals (GAS)

#### Generalised average of complex numbers

Let us consider  $N$  complex numbers  $x_j$ . The arithmetic average  $y_0$  is computed as:

$$y_0(x_j) = \frac{\sum_{j=1}^N x_j}{N}. \quad (4.2)$$

The generalised average of order  $p$  is defined by the formula:

$$y_p(x_j) = y_0 s^p, \quad (4.3)$$

where  $s$  is the ratio of the first and second moment:

$$s = \frac{|y_0|}{\sqrt{\frac{\sum_{j=1}^N |x_j|^2}{N}}} = \frac{\left| \sum_{j=1}^N x_j \right|}{\sqrt{N \sum_{j=1}^N |x_j|^2}}. \quad (4.4)$$

Order  $p$  is a non-negative real number. Parameter  $s$  is a real number from the interval  $\langle 0, 1 \rangle$ . The value 1 is reached only if all numbers  $x_j$  are equal. In this case, the generalised averages of all orders are equal. We can represent the averages as complex numbers:

$$y_p = A_p e^{i\varphi}. \quad (4.5)$$

If  $x_j$  are not equal, the amplitude  $A_p$  decreases with the order  $p$  and its limit is 0. The phase  $\varphi$  is independent of  $p$  (Málek *et. al.*, 2007).

Figure 4.5 illustrates the concept of generalised averages on a synthetic example of four complex numbers  $x_j$ . These numbers might represent repeated measurements of some quantity. If the measurements are erroneous or noisy (thus they show different amplitudes and phases), the average for higher orders  $p$  is close to zero and this set of measurements will be refused. If, on the other hand, the measurements are similar, then the values of successive orders of generalised average decrease much more slowly.

### Generalised average of seismograms

The generalised average can be extended to the situation when  $x_j$  are not complex numbers, but signals  $x_j(t)$  – time series represented by vectors of complex numbers. Vector  $x_j(t)$  with real numbers can represent one seismogram. The simplest possibility is to define the average seismogram as the vector of averages computed at the fixed time  $t$ :

$$\tilde{G}_p(t) = y_p(x_j(t)). \quad (4.6)$$

This definition is suitable of finding one-peak signal, but it does not fit seismograms.

If we can assume that the spectra of the signal and the noise are different, then it is advantageous to work in the frequency domain. In other words, we compute the complex spectrum of the seismogram first, then make a general average in the frequency domain and consequently convert it back to the time domain:

$$\hat{G}_p(x_j) = F^{-1}(y_p(F(x_j(t)))), \quad (4.7)$$

where  $F()$  is a symbol for the Fourier transform.

For the case of an arithmetic average (for  $p = 0$ ), formulas (4.6) and (4.7) give the same results. However, for  $p > 0$ , the results differ and monochromatic signals are amplified. Hence, the definition according to the formula (4.7) is apt mainly for large scale seismology, where we want to emphasise long-lasting signals with narrow spectrum, e.g. volcanic tremors.

For body waves, which represent relatively short signals with wide spectrum, we need a compromise between (4.6) and (4.7). According to Málek *et al.* (2007), such a compromise is achieved in three steps. The first step is to represent the signals  $x_j(t)$  by the sum of the signals shaped by moving cosine windows:

$$x_j(t) = \sum_{l=1}^L z_j^l(t), \quad (4.8)$$

$$z_j^l(t) = x_j(t)w^l(t), \quad (4.9)$$

$$w^l(t) = \frac{1}{2} \left( 1 + \cos \left( \pi \left( \frac{k - lh}{h} \right) \right) \right) \quad \text{for } k \in (lh - h, lh + h), \quad (4.10)$$

$$w^l(t) = 0 \quad \text{otherwise,}$$

where  $h$  is the half-width of the cosine window.

The second step is to apply the average to signals  $z_j^l$  (according to (4.7)). Finally, the last step prescribes to sum the signals according to the formula (4.8). Put together, the full definition of the generalised average is the following:

$$G_p(t) = \sum_{l=1}^L F^{-1} \left( y_p \left( F \left( x_j(t) w^l(t) \right) \right) \right). \quad (4.11)$$

The average is dependent on the half-width of the cosine window  $h$ . Thus, this parameter has to be tuned together with the parameter  $p$  to obtain optimal results for given application. For real signals, order  $p = 5$  is usually sufficient. The half-width of the cosine window  $h$  should be chosen according to the expected length of the filtered wave type. So, for long lasting signals (waves), the half-width of the cosine window should be large for the waves to fit into the window. Alternatively, we can use a large window if we know that the coherent signal would appear in the window only once and the rest of the signal is noise. In contrast, for filtering e.g. a small subset of the signal, we should select a small window.

In case of  $p = 0$ , the generalised average is equal to the arithmetic average of signals and it is thus equivalent to the simple stacking technique. If all signals are the same, the generalised average is equal to the signals (Málek *et al.*, 2007).

#### 4.2.2 Generalised average as a noise filter

The amplification of a coherent signal can be efficiently used in signal filtering when the repetition of the source is available. The noise-filtering capability is strong and it thus can be used even in a case when the noise and the signal have similar frequency contents (Fig. 4.6). The noise removing capabilities of the GAS are better than the results reached by the phase-weighted stack method (Schimmel and Paulssen, 1997). The better performance of the GAS is achieved, because – contrary to the PWS which consider only phases – the GAS considers the amplitudes in seismograms as well. However, in a real example, one naturally cannot expect such an impressive result: for one thing, the real signals are not absolutely coherent. In conventional shallow seismics, GAS can be used advantageously in noisy areas as well as in cases of prospection in urban areas (Fig. 4.7) instead of a simple stacking of shots. However, one has to be aware of possible distortions of the signal, in particular with a high order of the parameter  $p$ , as shown in Figure 4.6 g). On the other hand, for the order  $p$  lower than 10, the time distortion is negligible. Higher orders are usually not useful anyway: as said above, the real signal is never absolutely coherent, thus, with  $p$  of high orders any useful information would be filtered out from the record.

#### 4.2.3 Generalised average as a wave type filter

The amplification of coherent signals in GAS can be used also for the extraction of different wave types from seismograms. It benefits from the fact that different waves propagate along the profile with different velocities. Therefore, when neighbouring seismograms are shifted in time using certain time shift and then summed, wave type corresponding to the time shift is enhanced while other wave types are damped (Valenta and Málek, 2006).

An extraction can be carried out only on coherent seismograms, that is, only when the particular waveforms could be considered similar. The coherency essentially depends on three parameters: the scale of measurements, second, on the source distance



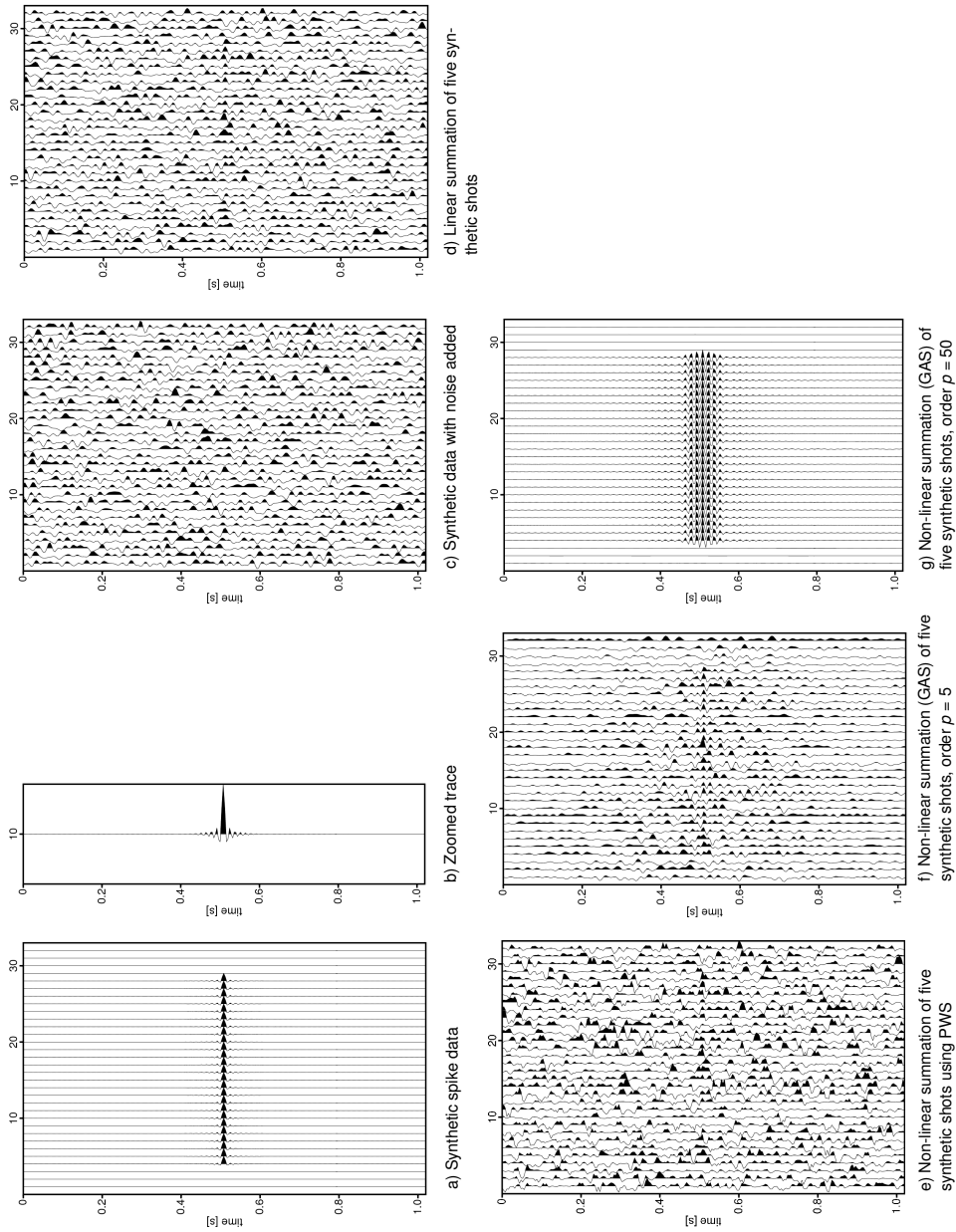


Figure 4.6: An example of GAS for noisy synthetic data. Five panels of synthetic spike data a) with frequencies of up to 70 Hz and random noise with a similar frequency range and S/N ratio 0.5 simulate five noisy seismic records c). Trace No. 10 of the spike data is zoomed in figure b). A comparison of linear (stacking) summation, non-linear summation using phase-weighted stack (PWS) and non-linear summation using generalised averages (GAS) is shown in figures d), e), f) and g). The noise is effectively removed with high values of order  $p$ , at the same time, however, the signal is blurred in time.

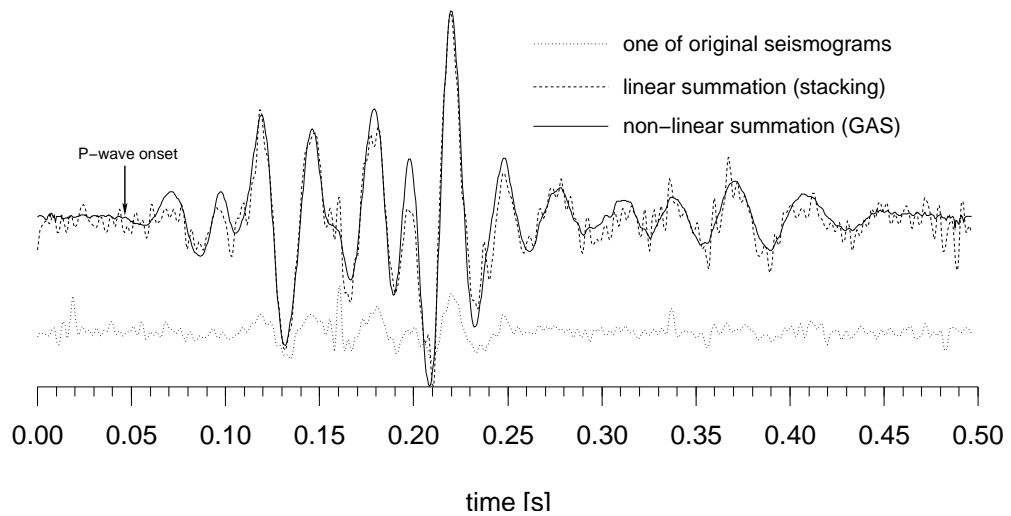


Figure 4.7: A comparison of linear summation (stacking) and non-linear summation (GAS). In this case, five real shots were summed together, with a sledgehammer as a source. Noise is effectively removed in GAS, and all important features (e.g., the onset of P waves) are clearly visible. One of the original records used for processing is plotted below for comparison. For the filtration, order  $p = 5$  was used.

(offset) and finally on the distance between geophones. Generally, the coherency increases with increasing scale of measurements and offset, and it decreases with increasing distance between sensors. Furthermore, other important factors affecting the propagating wave are frequency-dependent attenuation and heterogeneity of the medium. As for coherency, the most important parameter is the ratio between sensor spacing and wavelength of the seismic waves. Finally, the ratio between the offset and the wavelength should be considered. In shallow seismic prospecting, where the geophone spacing is in order of metres, seismograms from neighbouring geophones can be safely – for this purpose – considered coherent in offsets larger than several tens of metres.

The most demanding and confusing part of the GAS method is perhaps the estimation of an appropriate time shift. The time shift essentially depends on the velocity of the investigated wave and the distance between geophones. It can be estimated from the expected travel time curves (e.g. from the travel time curve for P-waves and some reasonable P/S velocity ratio, which is often about 2 in the near-surface prospecting). Alternatively, one can align certain distinct features, which could be considered to belong to the searched wave type (often, it might be the first minima or maxima, if they are possible to identify). As yet another alternative, the time shift can be determined by comparing the seismograms summed with different time shifts with a synthetic seismogram (or, possibly, with a coherent idea of how such a seismogram should look like). The finest similarity between the summed and synthetic seismograms gives the optimal time shift. The criteria which dictate whether the result is an optimal one are of many kinds – e.g. the sum of absolute values of amplitudes in a certain time window, the similarity of the waveform with a certain reference seismogram, or the smoothness of the filtered wave. Moreover, as this method is not oversensitive to small errors in the time-shift determination (due to the width of the cosine window), such time sensitivity might be considered as another criterion. If we shift input seismograms in time (of a small amount) from their ideal position, the filtered seismogram should not change dramatically.

In the near surface prospecting, however, the source receiver distances are usually too small for a sufficient P- and S-wave time separation. Thus, the direct filtration of these wave types is not possible (the filter window cannot be infinitely short). In these

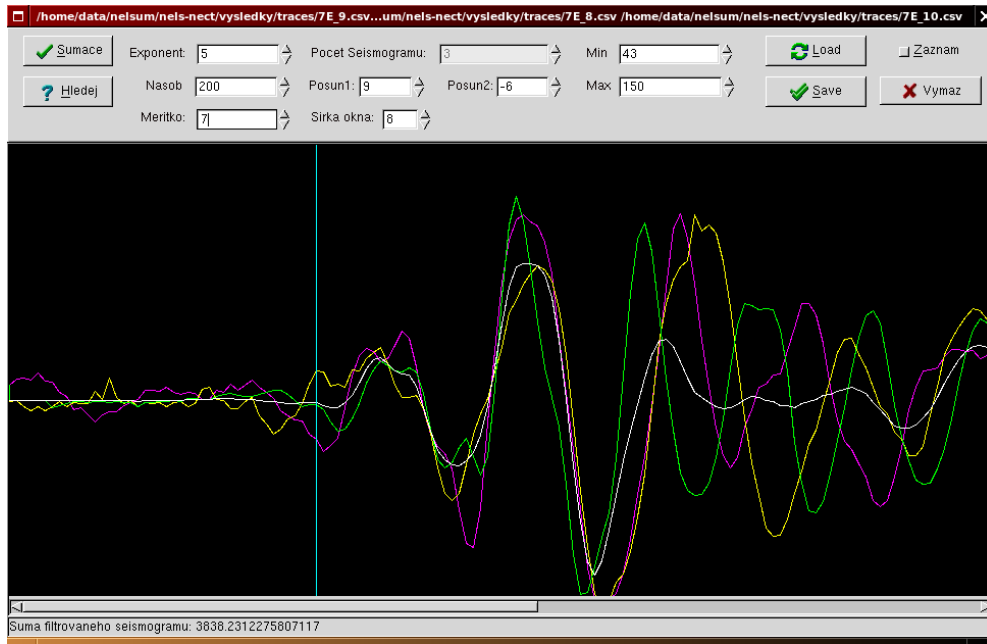


Figure 4.8: Example of S-wave filtration from the horizontal E-component (perpendicular to the profile). Three neighbouring seismograms (the yellow, magenta and green seismograms) are shifted in time and summed together using the GAS. The time shift is adequate to the S-wave, the onset of the P-wave is filtered out. The summed seismogram is plotted in white. The vertical blue marker indicates onset of the S-wave. The order  $p$  was set to 5 and the half-width of the cosine window  $h$  to 0.0156 seconds.

cases, the “inverse” filtration approach, as described in the beginning of this section, can be applied. The S-waves travel with different velocities than the P-waves, hence, the time difference between the P- and S-wave onsets differs along the profile. So, when the seismograms are shifted so that the P-waves sum destructively and are thus filtered out, as a result, the S-waves will be left on the record. Such a filtration can be done interactively with ease; the seismograms are shifted by trial and error method until the P-waves disappear and only the S-waves are left (Figure 4.8). This method produced the following examples.

The results of S-wave filtering are illustrated on a synthetic example in Figures 4.9, 4.10 and on the real seismograms in Figure 4.12. Ideally, the filtered seismograms should be as simple and smooth as possible, with reasonably localised onsets, with high amplitudes and with common features aligned.

The synthetic example simulates simple conditions of a layer over a half space. The velocity of P-waves in the upper layer is  $400 \text{ ms}^{-1}$  with the P/S velocity ratio 2. The thickness of the layer is 2 metres; the layer interface is horizontal. The velocity of P-waves in the half space is  $1200 \text{ ms}^{-1}$  and the P/S velocity ratio is 1.8. The seismograms were computed using the finite-difference method with the `sufdmod2` program from the Seismic Unix package (Cohen and Stockwell, 2007).

The complete PS seismograms were filtered using the “inverse” approach (as described above) to obtain the S-waves (Figures 4.9, 4.10). The filtered S-wave is good enough for reliable localisation of the onset. The whole filtered S-wave looks like the original seismogram with a high-cut filter applied. However, it is impossible to get the same result with a simple frequency filtering (Figure 4.11): the filtered low velocity seismogram is unable to depict the relatively sharp onset.

Figure 4.12 compares the results of the S-wave filtering using the GAS with the results of the polarity reversal method. The parameters for the GAS method were

$p = 5$  and  $h = 0.0156$  seconds. The wave types were filtered using the described criteria for the time shift: common features aligned, a reasonable P/S velocity ratio, the filtered wave is smooth and simple and finally, the small time shifts should not change the filtered seismogram by much. Furthermore, the resulting travel time curves must “be reasonable” – the reciprocal travel times must coincide, the shape of the travel time curves should be similar (the deviations from the idealised smooth curve should correspond on individual curves), etc.

The author intended to compare the GAS filtering with results of the polarisation analysis as well. However, as it was stated in the introduction to this chapter, the polarisation analysis failed. The reasons for such a dull failure might be twofold: first, the small time separation between individual wave types could be blamed and second, the level of noise in seismograms was unexpectedly high.

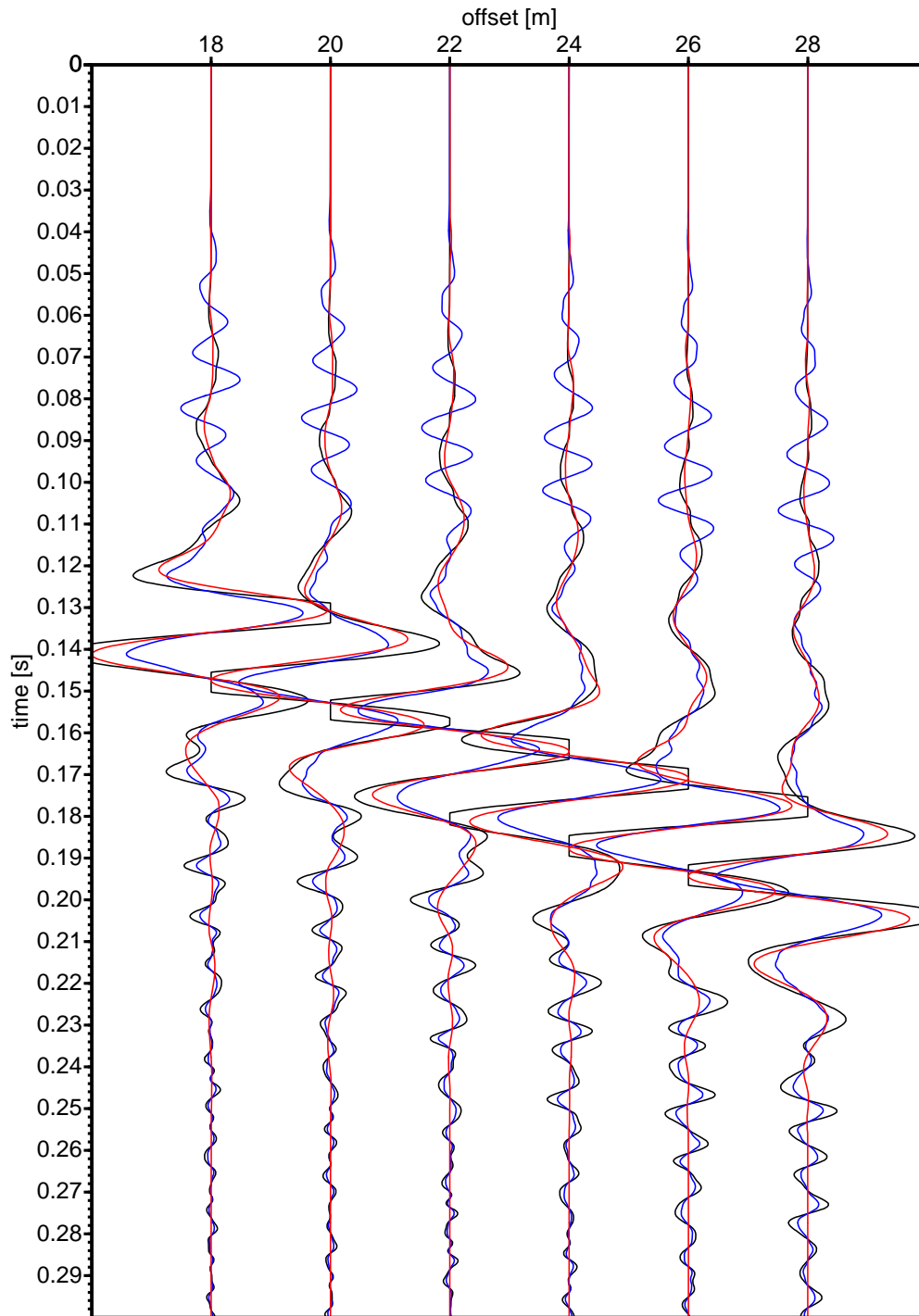


Figure 4.9: Example of S-wave onsets filtering. A synthetic seismogram was computed for the two-layered media. The thickness of the upper layer was 2 metres, velocity of P-waves was  $400 \text{ ms}^{-1}$  and the P/S velocity ratio was 2. The velocity of the P-waves in the bottom layer (half space) was  $1200 \text{ ms}^{-1}$  and the P/S velocity ratio was 1.8. The synthetic seismogram is plotted in blue, a synthetic seismogram only for the S-wave is shown in black. The filtered S-wave from the complete (blue) seismogram is plotted in red. An enlarged view of the onsets is plotted in Figure 4.10. All traces are normalised to make all the features visible.

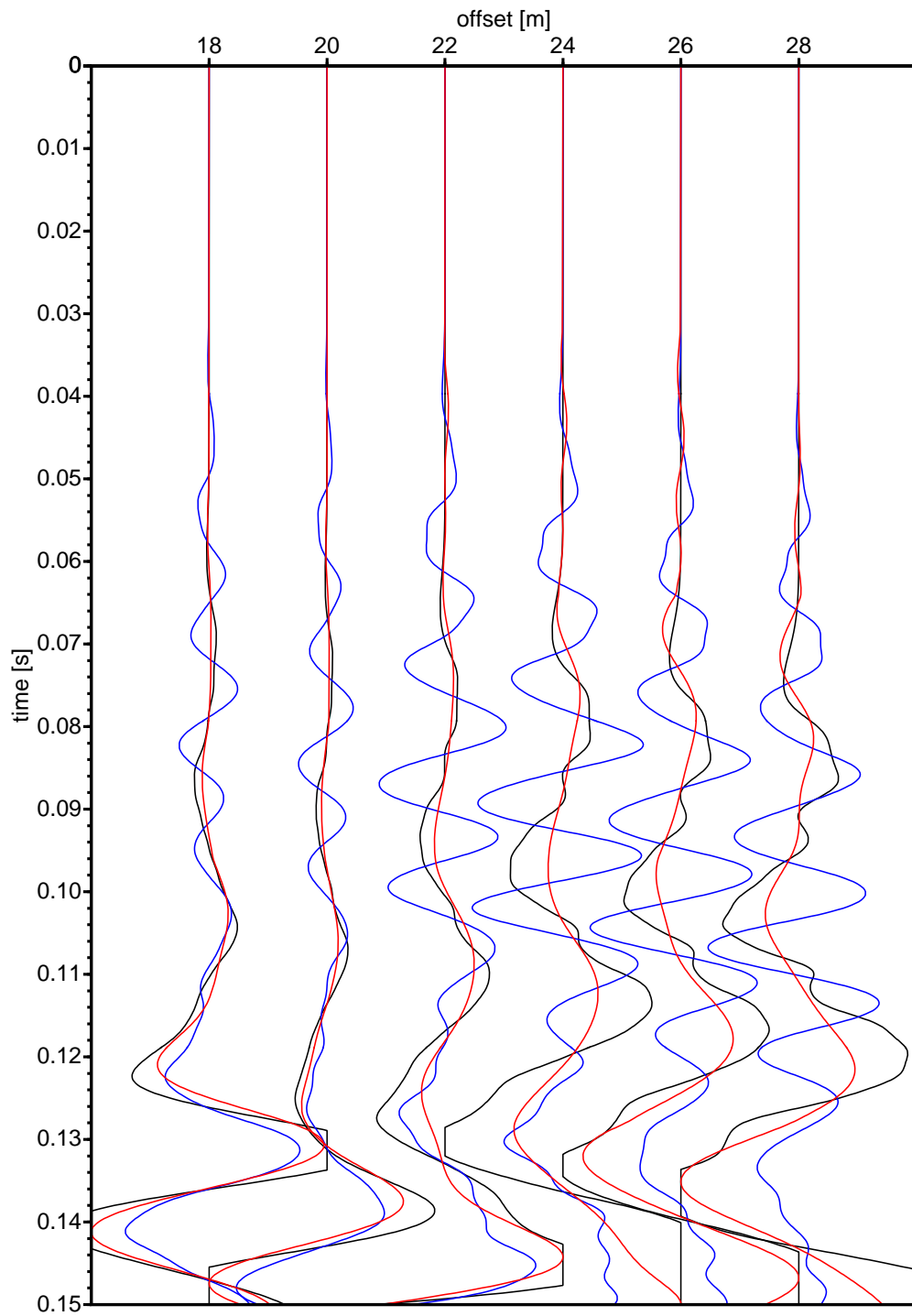


Figure 4.10: The first half of the seismograms from Figure 4.9 is enlarged, so that the onsets could be seen. The colours used in the seismograms are the same as in Figure 4.9.

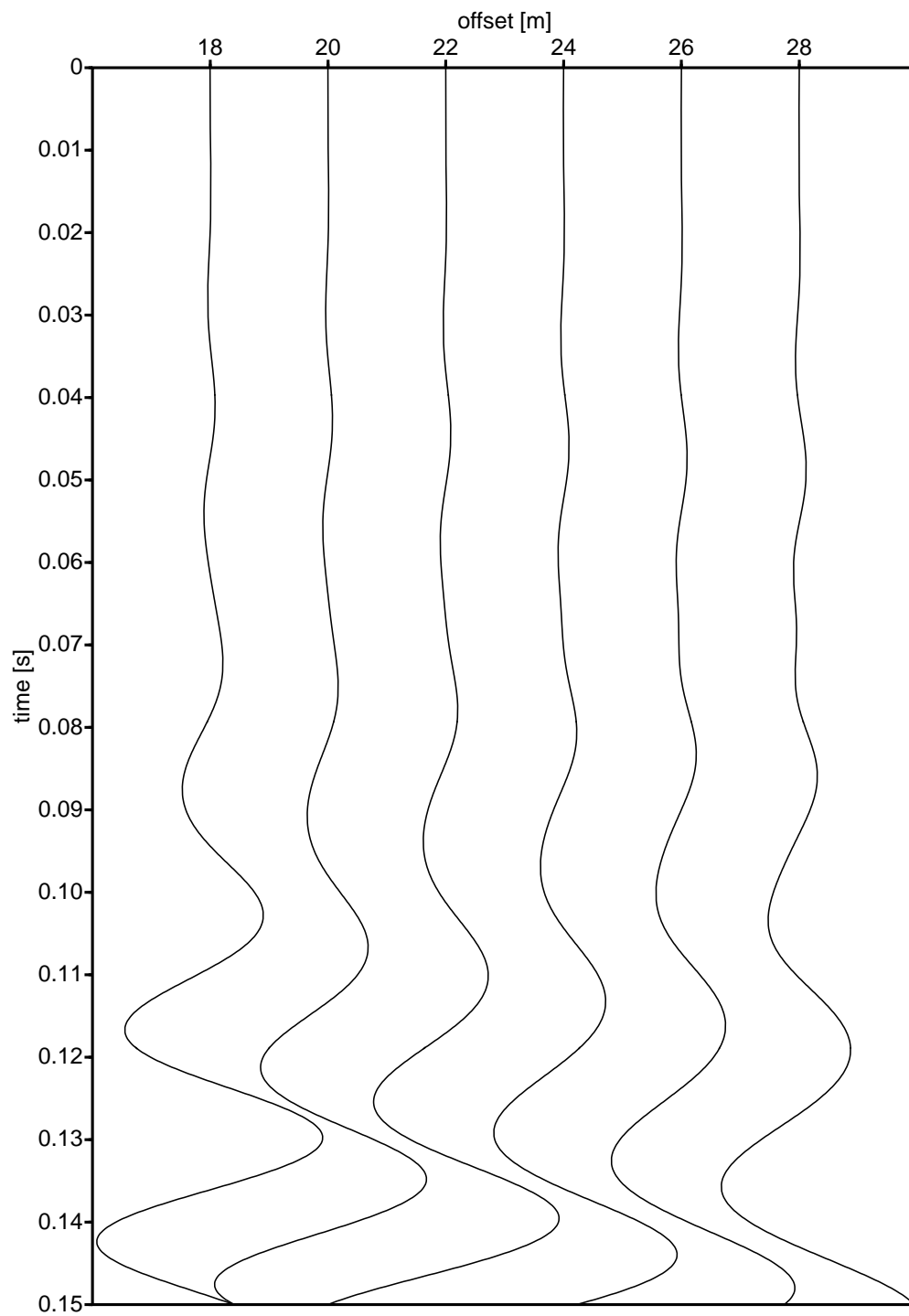


Figure 4.11: Low pass filtering of the synthetic seismograms from Figures 4.9 and 4.10. To emphasise the main frequency range of the *S*-wave, the Butterworth high-cut filter was used to filter out frequencies higher than 60 Hz. However, as expected, the filtered seismograms are not able to represent as sharp changes as the onsets should be.

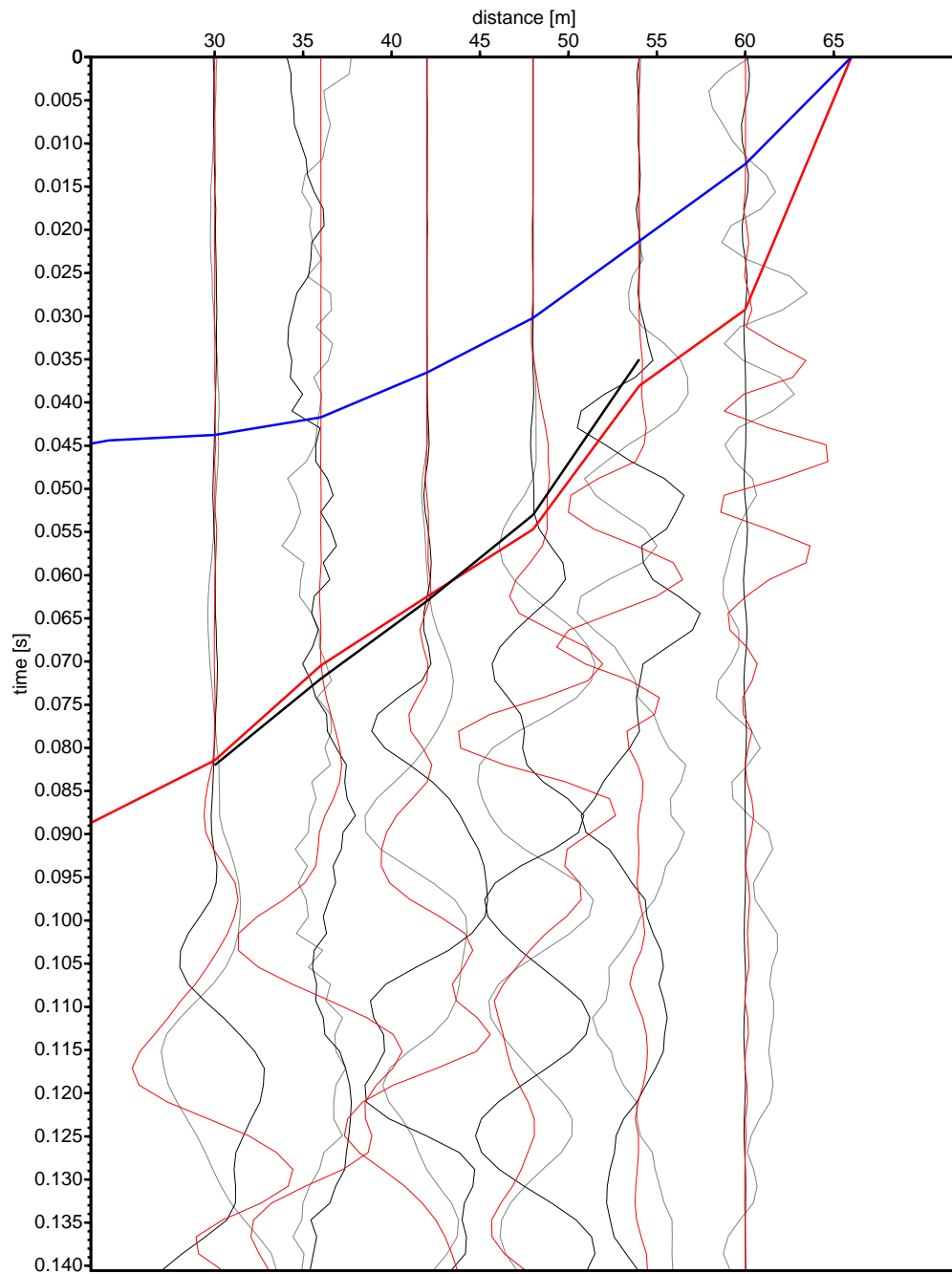


Figure 4.12: Determination of *S*-wave onsets using GAS and polarity reversal method. As a source for the GAS, vertical sledgehammer strikes were used; as a source for the polarity reversal method, strikes to a wooden bar were applied. The filtered seismogram from the GAS is plotted in red; so is the corresponding *S*-wave travel time curve. The seismograms from the method of polarity reversals (opposite strike directions) are plotted in black and grey. – the onset of *S*-wave appears as a reversals of a polarity of the seismograms. An appropriate travel time curve is plotted in black. The polarity reversal seismograms at the *x*-coordinate 60 are not usable for the onset picking. However, the *S*-wave onsets (which were possible to determine) are consistent with onsets from the GAS method. The traces are for the *E*-component and source located at the *x*-coordinate 66 metres. The rest of the travel time curves can be seen in Figure 4.14. For comparison, the *P*-wave travel time curve is plotted in blue.



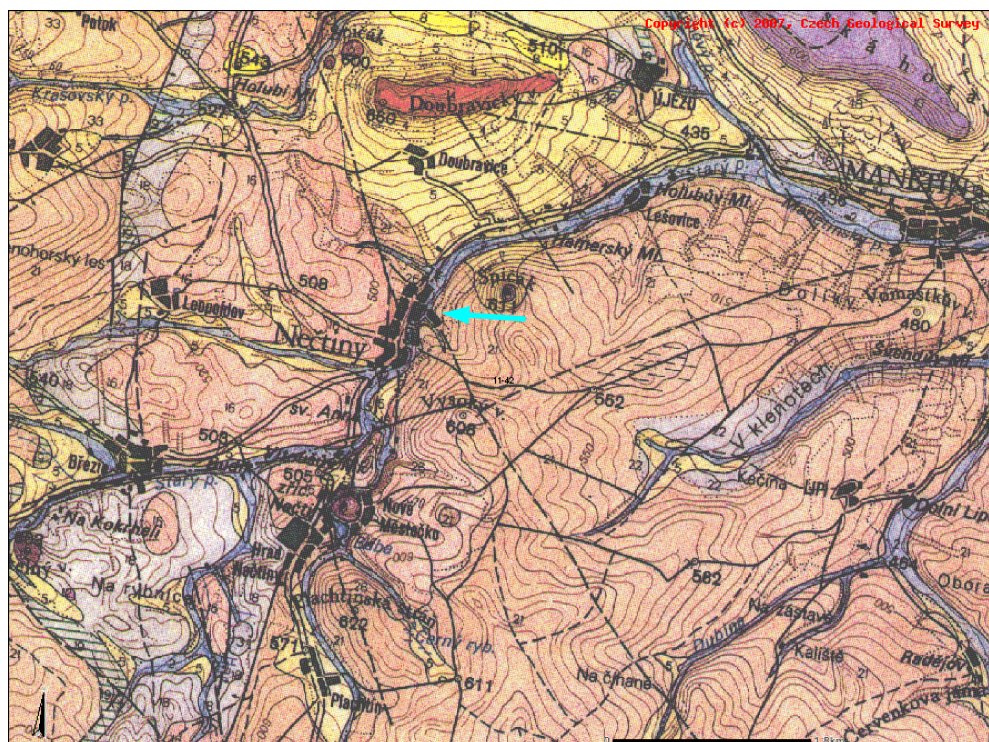


Figure 4.13: A part of the geological map 11–42 Manětín (Kopecký, 1984), showing the geological surroundings of the village of Nečtiny. Blue arrow points to the area of survey. Map legend: **Quaternary**: 2 – fluvial sediments, 5 – colluvial sediments; **Tertiary**: 10 – nepheline basanite, 14 – trachyandesite; **Permo-Carboniferous – Stephanian C–Autunian**: 16 – subarkoses and conglomerates, 18 – siltstones and subarkoses, 19 – claystones; **Carboniferous – Westphalian D–Stephanian A**: 21 – subarkoses, arkoses with layers of conglomerates; **Carboniferous – Westphalian D**: 22 – siltstones, claystones with coal beds, arkoses and conglomerates; **Upper Proterozoic**: 26 – chlorite-sericite phyllite.

### 4.3 Field example – Nečtiny

Having examined possible approaches to the S-wave separation, it is time now to provide the readers with a field example of the S-wave separation. This case study was conducted at the village Nečtiny in western Bohemia. In this village, the seismic station NEC is located. The goal of this study was to resolve the shallow structure beneath the seismic station.

Nečtiny is a small village near the city Plzeň in western Bohemia. From the geological point of view it belongs to the Central Bohemian limnic Anthracolithic system, the Manětín Basin. The geological environment of the locality is formed mainly by the Upper Carboniferous arkoses and conglomerates, Proterozoic phyllites and inevitable Quaternary sediments (Fig. 4.13). The geological setting of this area is rather complex and particular geological maps differ in details. The main differences between individual maps in the vicinity of Nečtiny are in the position of the Proterozoic rocks.

The basement of the NEC seismic station is formed by the Proterozoic phyllites (however not plotted in Figure 4.13). Carboniferous arkoses and conglomerates, however, form outcrops in the near vicinity. The contact of Carboniferous rocks and Proterozoic phyllites was supposed to be resolved by a seismic profile.

The profile was oriented in the direction from west to east, coordinates increasing eastwards, measured with three-component geophones with a spacing of 6 metres. The source of seismic waves was a sledgehammer (vertical strikes to a metal plate).

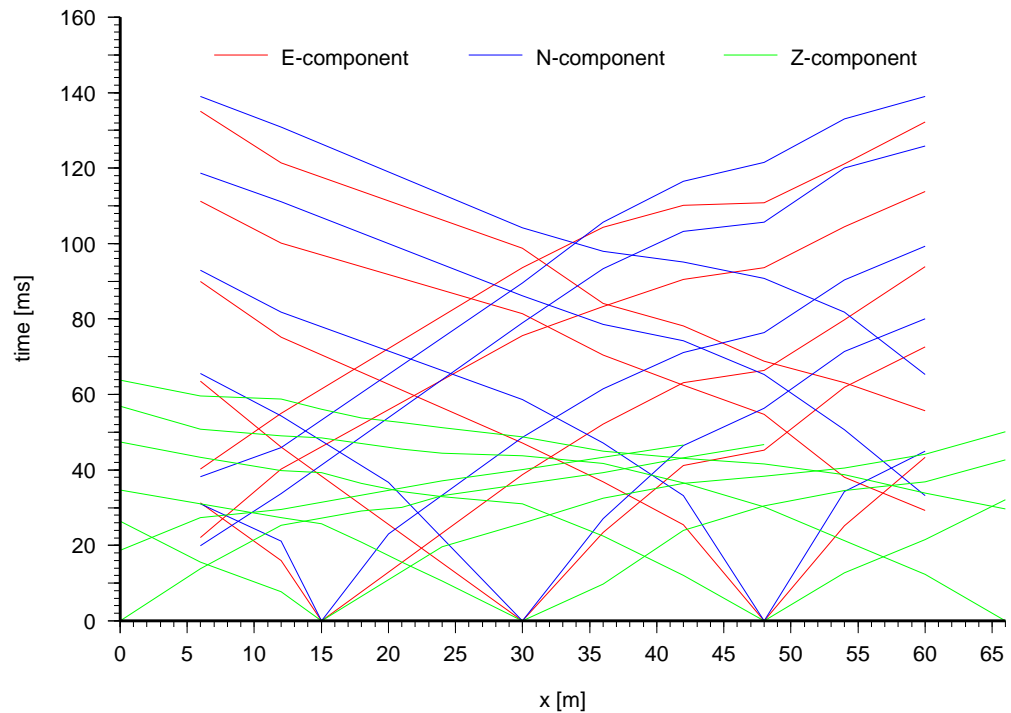


Figure 4.14: curves for individual components, plotted for comparison. The horizontal E-component (that is supposed to represent SH-waves) is perpendicular to the profile, horizontal N-component (that should represent SV-waves) is parallel to the profile. The vertical component is denoted as Z (representing P-waves). The S-wave onset of the first and last geophones from the spread at the location was not determined; instead, an average from three neighbouring seismograms was used.

As the phyllites are strongly weathered, they create gradient environment rather than a soil and bedrock layer. Hence, the travel time data had to be processed by means of seismic tomography, even though the ray coverage was not ideal. As a partial compensation for poor ray coverage, the tomographical inversion process was carried out very carefully, comparing results for different starting models and settings – e.g., different starting models should produce comparable final models.

The P-wave data from the vertical geophone component were processed by picking the first onset; then, the first arrival travel time tomography was applied (to compute the travel time tomography, the Plotrefa tomography program from the Geometrics, Inc. was used).

Figure 4.16 shows the resulting P-wave velocity cross-section. The velocity profile shows a strong vertical gradient with no obvious layering. The lateral variation of velocities is negligible; the change in homogeneity is the lowered gradient of velocities in the upper right part of the profile – it begins about the x-coordinate 25 propagating to the depth about 463–462 metres at the x-coordinate 60. Then, it is replaced by a gradient of increased velocity. The lowered gradient of velocities might reflect the change in lithology from Proterozoic phyllites to Carboniferous conglomerates and arkoses. The increased velocity gradient in bedrock of Carboniferous sediments is, again, a sign of Proterozoic phyllites. However, the P-wave velocity profile itself is not particularly convincing in this. In this cross-section, no other indices of changes in lithology are detectable. In other words, the information about the P-wave velocity cross-section is rather limited.

On the other hand, from the outcrops of phyllites and Carboniferous sediments it is clear that the contact must be crossed by the profile. Hence, if the phyllites and

Carboniferous sediments have similar P-wave velocities, we have to process the data in some other way. We may benefit from the fact that the phyllites are highly schistose and weathered. The sediments, in contrast, are more compact; so, when the P-wave velocities are similar, then the S-wave velocities should differ.

There were no special S-wave survey carried out on the locality, we took advantage of the three-component records and tried to find onsets of the S-waves. So, because there were no data from a special S-wave source, we had to use records of the P-wave source (hammer strikes) and S-waves generated by the strikes. Now, we use this example to demonstrate the GAS filtering method.

As already mentioned, the S-waves were filtered from three adjacent records; the filtered wave was assigned to the record in the middle. Therefore, the very first and very last record do not have their S-wave determined. The time of the trace in middle was fixed, while the traces on sides were shifted in time to produce an optimal result. The criterions for the filtered S-wave were the following:

1. The time shifts must be “reasonable” – the time shifts of the traces must correspond to the expected travel time curve.
2. The filtered S-wave must be similar to the expected S-wave. Thus, the interpreter must have an idea what the wave should look like; that is, it should be smooth, the amplitudes should fall into certain range, there should be a low amplitude onset followed by a higher amplitude maxima, etc. A synthetic seismograms might be of help here.
3. Finally, the resulting travel time curves must undergo the common “reliability tests” – the reciprocal travel time check, the shape of the travel time curves should be similar (the deviations from the idealised smooth curve should correspond on individual curves), etc.

Both horizontal components (N and E) were processed, which led to two travel time sets for two orthogonal directions. We will consider these directions to represent SV- and SH-waves (Figures 4.14 and 4.16), even if this might not be true in the real 3D media. However, as the whole measurements and interpretation is done in 2D, the available information is not sufficient for more advanced processing anyway.

The S-wave travel time curves were processed in the same manner as travel time curves for the P-wave using the first arrival travel time tomography (Figure 4.15). The resulting velocity cross-sections are plotted in Figure 4.16.

The S-wave velocity profiles show, again, media with a vertical velocity gradient with no obvious layering. However, changes in the velocity gradient are more distinct than in the case of the P-wave section. This changes in velocity gradient probably indicates the change in lithology.

But we may go further and try to compute the P- and S-wave velocity ratios. The velocity ratios are depicted in Figure 4.17.

The most distinct feature of the P/S cross-sections is the very high P/S velocity ratio, exceeding – surprisingly – the value 3. The zone with this high ratio is located in the lower left corner of the profile – in the west. The gradient of the P/S ratios in this zone is very steep, indicating that the velocity of P-waves is increasing very quickly here, while the increase of S-wave velocities is only minor. The high increase of P-wave velocities connected with a scant increase in S-wave velocities is often connected to a presence of groundwater in the media with high content of clay particles. Very likely, it is the case here as well. The weathered phyllites are producing highly clayish media with a gradient of velocities for P-waves that becomes even steeper if groundwater is present. But as the S-waves are not affected by the groundwater, the S-wave velocity gradient should be less steep.

Furthermore, the zone of high P/S velocity ratio is larger than 8 meters in the depth. Going to this depth, we are getting to the same level as the nearby Starý creek

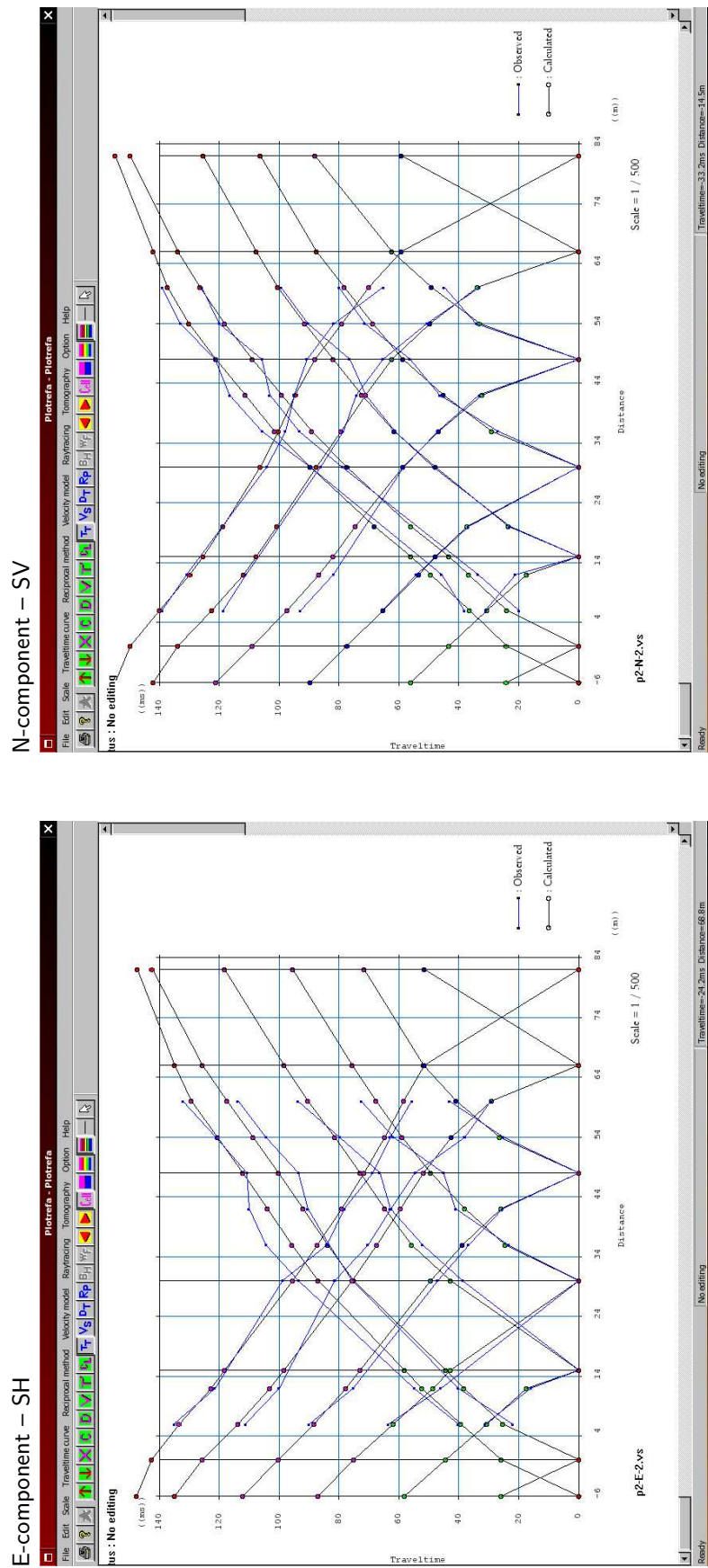


Figure 4.15: Measured and synthetic travel time curves for the horizontal E-component (perpendicular to the profile) and N-component (parallel to the profile). Measured travel time curves are plotted in the blue. The black line shows the synthetic travel time curves for the SH and SV velocity models from Figure 4.16.



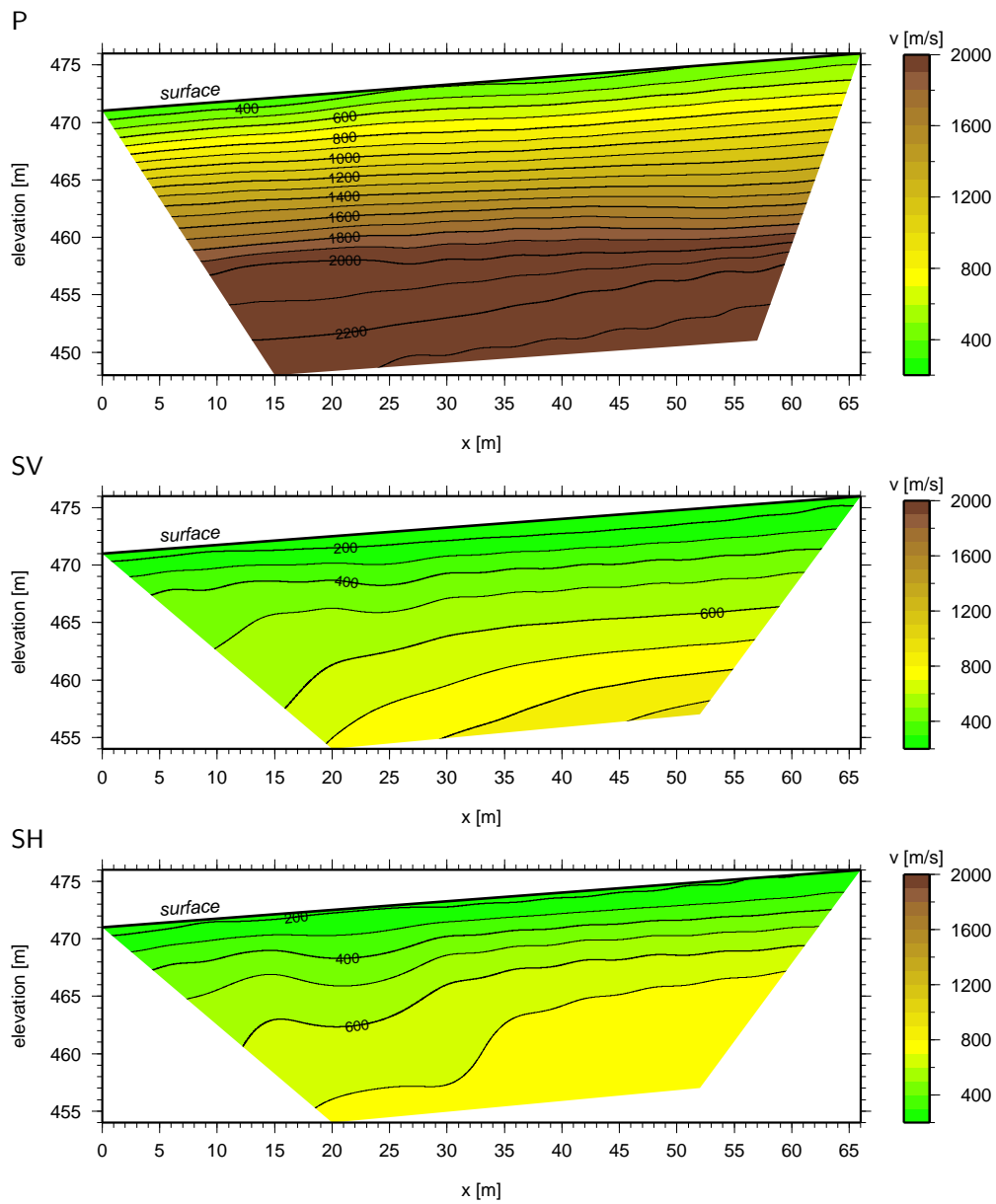


Figure 4.16: Velocities of P, SV and SH waves from the travel time tomography. The onsets of SV and SH waves were determined using the GAS technique from records of P-wave source and horizontal components of geophones.

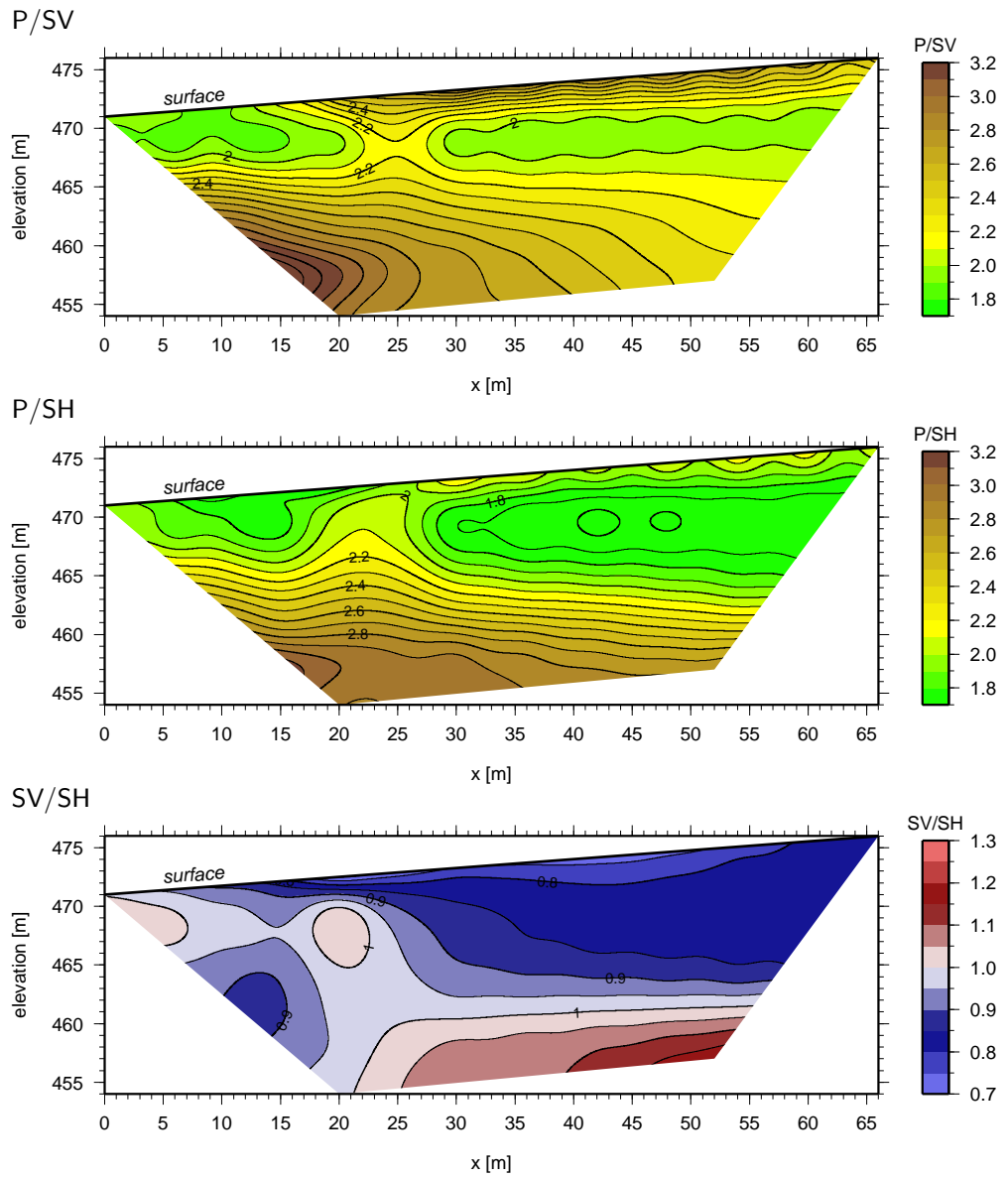


Figure 4.17: Velocity ratios. The high values of the P/S velocity ratio might indicate groundwater. The water table is positioned to the highest P/S velocity gradient. The SV/SH ratio shows anisotropy of the S wave velocities and thus changes in physical properties of the rock massif. The SV-waves are faster up to the X coordinate 42, where the SH-waves becomes the faster one. Hence, the change in lithology or in the angle of bedding can be expected. In this particular case, it is interpreted as a change in lithology from the Proterozoic chlorite-sericite phyllites (on the left) to the Carboniferous arkoses and conglomerates (on the right).

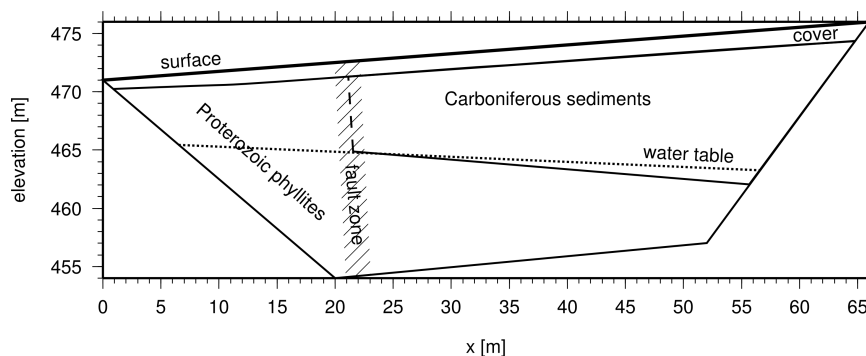


Figure 4.18: Interpretation of cross-sections from Figures 4.16 and 4.17. This interpretation is based mostly on the P/S and SV/SH velocity ratios. The near surface soil and weathered layer is characterised by high P/S ratios. In this layer, the SH-waves are faster than the SV-waves. The groundwater table is placed into very steep gradient of P/S ratios. The phyllites and Carboniferous sediments are differentiated mainly according to their SV/SH ratios. The SV-waves are faster than the SH-waves in phyllites, while this ratio is reversed in the sediments. The zone with increased P/S velocity ratios inside the Proterozoic phyllites is interpreted as a fault zone.

and its river plain. Hence, the groundwater hypothesis should be considered reliable. The water table plotted in Figure 4.18 is placed into the steepest gradient of P/S velocity ratios in a way that should be reasonable on both cross-sections (P/SV and P/SH).

The lithology change is visible on the P/S velocity cross-sections as well. The high P/S ratios down to the depth of about 2 metres might characterise the uppermost layer of soil and highly weathered rocks.

Finally, we are approaching the last cross-section from Figure 4.17. It is the distribution of the SV/SH velocity ratios along the profile. The SV- and SH-waves might travel with different velocities. The difference is connected to the anisotropy of rocks. The anisotropy might be induced by a number of causes. In this case, the parts of the profile where the SV/SH ratios differ (large scale part, where the SH waves are faster and part where the velocities are similar) could be caused by different materials. So, we can split the profile into two sections (Fig. 4.18).

The first one is located at the upper right part of the profile and the SH waves are faster there. The SV/SH ratio is lower than 0.9. Also, in this part, the SV/SH ratio is relatively homogeneous. Very likely, this part is formed by the Carboniferous arkoses and conglomerates.

On the other hand, the second part is located in the west side of the profile in the low x-coordinates and in the most part of the bottom of the whole profile. The SV/SH velocity ratio is oscillating around the value 1: there is no dominant direction of anisotropy. Such a situation is typical either for a homogeneous media or for a media, where the anisotropy is present, but the direction changes quickly. The latter case is probably what happens in this case; this area represents block of the Proterozoic phyllites, which are schistose and closely folded. Moreover, the area inside this block with increased P/S velocity ratios might represent a tectonically disturbed zone – a fault zone. Hence, the block as a whole appears to have only low anisotropy, even though the anisotropy of schistose phyllites should be high.

To determine the anisotropy of the Proterozoic phyllites, Roman Živor (Institute of Geology, Academy of Sciences) kindly measured the anisotropy on samples under rising pressure (0–150 MPa) using the ultrasonic waves. The anisotropy was found to decrease with rising pressure (as can be expected): under the pressure of 150 MPa the anisotropy was 18 %, while when the pressure is low – and thus resembles the

*The anisotropy of rocks is related to their lamination, fracturing, grain shape and orientation, etc. The details are beyond the scope of this paper. For more information, see Stuart Crampton (1985).*

near-surface conditions – it reaches 32 %. The anisotropy in a weathered geological environment can be even higher than on the rock sample.

This field example illustrates a case with a limited amount of information on individual velocity profiles. However, as hopefully proven by this study, when all available information from all the profiles is assembled together, the results might be surprisingly precise. The cross-sections of velocity ratios (Fig. 4.17) provide us with an insight into the subsurface described in far more informative details than the conventional velocity cross-sections. So, the only negative down side of the S-wave extraction is a laborious data processing; that, again, stems from the fact that the S-wave filtration is enormously time consuming.

## 4.4 Conclusion

In this chapter, we investigated and compared two methods of S-wave identification and separation. The first one, method of oriented sources or polarity reversals, is simply a modified classical method. As was concluded, an important drawback of this method is the need of oriented sources. The most common sources of an oriented source – the sledgehammer and a bar – is of a limited usage, as the generated energy is very low. On the other hand, more sophisticated sources – such as vibrators – produce sufficient amount of energy, but they are heavy, clumsy and, not least, expensive. So, this method is suitable in a limited range of cases; it is often used with success in short and shallow profiles.

The second method of S-wave filtration – the GAS method (or, alternatively, a method that would use another (similar) filter) – turned out to be very promising. First of all, as such a method uses conventional P-wave sources as a source of seismic energy, the field work is fast and easy. However, to make this method clearly superior in a serious use, some technical improvements are called for. In particular, it would be great to have an interactive graphical interface such that it would make possible to visualise traces side by side, shift them in time, see results and pick onsets. Without a help of such a software, the filtration is a laborious and iterative (trial and error) task. Yet, the case study showed that once the filtration is carried out successfully, the results could be impressive.



---

## REFRACT3D – computer program for 3D refraction data processing

The REFRACT3D is a computer program, developed as a part of this thesis, for processing of three dimensional refraction data sets. Sources of the REFRACT3D and binary version for Linux can be found on the enclosed CD-ROM. The program is written in Pascal programming language and the GUI (graphical user interface) was developed using the Lazarus<sup>1</sup>.

The current version of REFRACT3D is a development version. Currently only two layer media is supported (layer over the half-space). The system of equations is send to Octave script<sup>2</sup> for solving. It is necessary to use Octave version 2.9.6 or newer, due to the changes in syntax of the `argv` function. The Octave script is used because it is easily possible to select between various computation schemes in Octave. This is very convenient when choosing the right one, but the drawback is, that the Octave scripts run slowly.

Microsoft Windows are not capable of running Octave scripts directly, and therefore current version of REFRACT3D runs only on UNIX-like operating systems. Therefore in future release the Octave script should be removed, enabling REFRACT3D to run also under the MS Windows.

The program is used for computing layered models for a 3D refraction data sets. However, currently is limited to a model of a layer over the half-space. It uses modified time-term method, described in Chapter 1.4. Seismic parameters of subsurface (normal thicknesses of layers and layer velocities) are computed in a regular rectangular grid with arbitrary grid spacing. The inversion process is iterative with small number of iterations. Input and output files are column ASCII files separated by tabs or spaces. Input is a file with  $x$  and  $y$  coordinates of sources and receivers and with first arrival data classified according to the boundary along which the head wave is travelling. Output is a file with  $x$  and  $y$  coordinates of individual grid points with velocities for all layers in the dataset, standard deviations of these velocities, thicknesses of all layers and their standard deviations.

---

<sup>1</sup>Lazarus is an open-source development environment designed to be similar to the Delphi from Borland. It is available for various operating systems and can be downloaded from the Lazarus WWW pages at <http://lazarus.freepascal.org>

<sup>2</sup>Octave is a Matlab-like environment with many ready to use functions for numerical computations. It is available for wide range of operating systems on the <http://www.octave.org>

```

#! /usr/bin/octave -qf
##
## The first line of this file should point to the Octave executable.
## If you have Octave binary in another directory than /usr/bin,
## modify, please, the path. If the "/usr/bin/octave" does not work,
## you may want to try "/usr/local/bin/octave".
##
##
... cut to save space

```

Figure 5.1: Beginning of the `ComputeSVD.m` script. The first line in this script must point to the Octave executable.

## 5.1 REFRACT3D – User’s manual

To start REFRACT3D, move to the directory where the REFRACT3D is installed. Make sure that also the Octave script `ComputeSVD.m` is present. Check, if the path to the Octave executable on the first line of the `ComputeSVD.m` script is correct. Otherwise, you will have to modify it (Fig. 5.1). Then you can start the REFRACT3D by typing `./refract3d` on the command line, or by clicking on it in a graphical commander. The REFRACT3D has a simple graphical user interface (GUI). When it is started, the initial window looks similarly to that one in Figure 5.2. The input file is loaded through the File → Open menu. If the file is read successfully, you will receive a confirmation message on the program’s status bar.

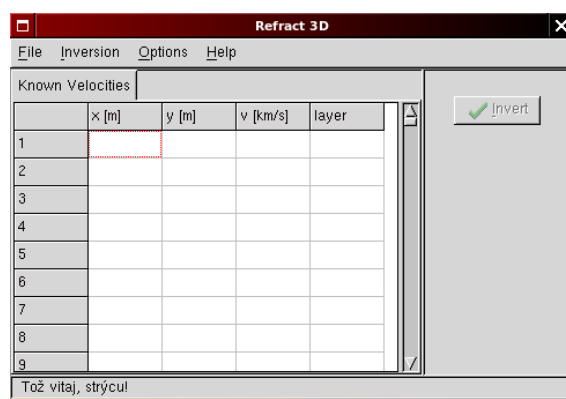


Figure 5.2: Initial window of REFRACT3D.

*The layer velocities are considered to be constant in a vertical direction in every individual layer. This is implied by the simple layered model used. In a real world, the head waves (considered here) are rather refracted waves in the gradient media. In this sense the velocities computed should be called boundary velocities.*

val time (floating point number) and number of layer on top of which the head wave is travelling (integer). The uppermost layer has number 1 and it means that the wave travelling through this layer is a direct wave. The velocity of the uppermost layer is computed from this travel time. Seismic wave refracted on the first interface has a layer number 2 and so on. This block is repeated for every source in the dataset.

The data in the output file (see Fig. 5.4) are written to columns. Number of columns depends on the number of layers in processed dataset. The first line in the file is header, labelling individual columns. The first two columns are  $x$  and  $y$  coordinates of the current grid point (they are labelled  $x$  and  $y$  in the header). The third column contains resolved velocities of a direct wave labelled  $v_0$ . Number of following columns depends on the number of layers included. Velocities of individual layers are labelled  $v_1$ ,  $v_2$ , etc. Corresponding standard deviations are labelled  $std.v_1$ ,  $std.v_2$  and so on. Thicknesses of individual layers are marked  $d_0$ ,  $d_1$ , ..., where the  $d_0$  is the normal

The structure of the input file is strict and does not allow any comments. Numbers are delimited by tabs or spaces. The file consists of blocks, each related to particular source (see Fig. 5.3). Each block begins with a line related to the source. It contains  $x$  and  $y$  coordinates of the source (floating point numbers), followed by the number of first arrivals for current source (integer) and a dummy number 0 to keep the four columns structure. The source line is followed by lines with first arrivals. They consists of  $x$  and  $y$  coordinate of the receiver (floating point numbers), first arri-

```

11 56 12 0          source line – x-coord, y-coord, number of first arrivals, dummy
19 76 18.062195 2   receiver line – x-coord, y-coord, first arrival time, layer number
19 72 17.973307 2   receiver line
19 68 16.782198 2   receiver line
19 64 16.693308 2   receiver line
19 60 15.377755 2   receiver line
19 56 15.431088 2   receiver line
15 56 11.893315 1   receiver line
15 60 13.066648 2   receiver line
15 64 14.435534 2   receiver line
15 68 14.524423 2   receiver line
15 72 15.004422 2   receiver line
15 76 15.57331 2    receiver line
11 60 24 0          source line
27 76 20.266636 2   receiver line
27 72 20.319969 2   receiver line
... cut to save space

```

Figure 5.3: Example of input file for REFRAC3D.

```

x y v0 v1 std_v1 d0 std_d0
11 55 0.336 2.358 0.061 2.017 0.135
11 59 0.266 2.582 0.032 2.321 0.080
11 63 0.265 4.300 0.025 2.375 0.075
11 67 0.316 4.336 0.025 2.570 0.089
11 71 0.340 3.044 0.028 2.391 0.096
... cut to save space

```

Figure 5.4: Example of output file for the two layer media from REFRAC3D.

thickness of the uppermost layer. Standard deviations of thicknesses are marked as `std_d0` and so on until the half-space is reached.

The “known velocities” table in the main window of the program can be used for supplying already known velocities from another type of survey. These velocities then enter the inversion process. However, they are not kept fixed throughout the inversion process. This is an intention, because velocities resolved by different methods are not equal. If the user really wants to keep the velocities fixed, then he must enter them by Octave commands in the `ComputeSVD.m` script. Then he would probably also want to change uncertainties for these values in the covariance matrix. On one hand this is very inconvenient for the user, because dealing directly with the source code may not be trivial. On the other hand it gives more flexibility in specifying probabilities of user supplied values.

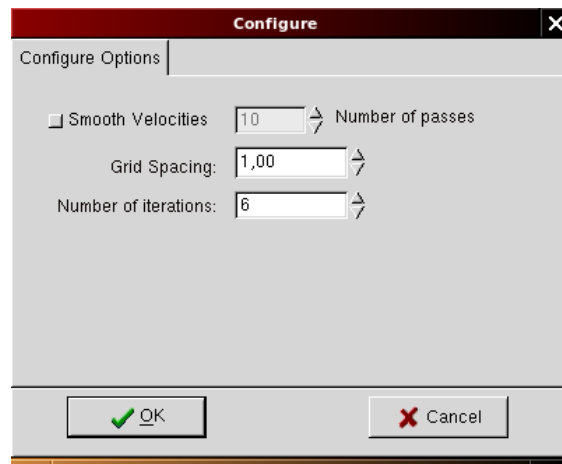


Figure 5.5: Configuration window of REFRAC3D.

Some useful inversion parameters can be specified using the Options → Configure menu (Fig. 5.5). The “Smooth Velocities” checkbox can be used, if it is desired to smo-

oth computed velocities between individual iterations. Smoothing is done by averaging in moving window. It is possible to specify number of smoothing passes.

The “Grid Spacing” field defines the size of the inversion cells in metres. The cells may have an arbitrary size. The best cell size for each particular dataset is usually obtained by trial and error method. If the cell size is too large, then the resulting depths and velocities lack details. Too small cell size will produce ill determined system of equations and no reasonable results should be expected. The rule of thumb is that the cell size should be comparable with the source and receiver step of the survey.

When all of these parameters are set correctly, it is possible to run the inversion by clicking on the “Invert” button. The program sorts all the travel times and finds which sources are identical with receivers. This is a valuable piece of information for the inversion process reducing ambiguities in the receiver and source depths. According to the equation 1.5 a change in the depth beneath the receiver  $h_r$  can be compensated with a change in the depth beneath the source  $h_s$ . This affects all source-receiver pairs in the data set. However, when the depth beneath the particular receiver is set to be equal to the depth beneath the particular source, this ambiguity is resolved. It is a good idea to plan the field survey layout with respect to this limitation.

When the iteration process is finished, you can save resolved depths, velocities and appropriate standard deviations using the File → Save menu entry.

## 5.2 REFRAC3D – how does it work?

The user manual finished with pressing the “Invert” button. Now, we can look under the hood and describe the technical details.

When the corresponding sources and receivers are found, the lengths of rays in individual cells are computed and the matrix of coefficients  $\mathbf{A}$  is assembled and written to the file. The file is called `MatA.csv` and is located in the same directory as the REFRAC3D. The vector of right-hand sides is written to the file `VectB.csv` and both of these files are read by the `ComputeSVD.m` script.

The only role of the `ComputeSVD.m` script is to solve the system of equations and to compute uncertainties of individual unknowns. Solution of the system of linear equations is done by the singular value decomposition method and the Moore-Penrose pseudoinverse (generalised inverse, pseudoinverse) technique.

The singular value decomposition (SVD) is a well known technique of solving systems of linear equations, suitable when the system is ill determined. The SVD algorithm was described e.g. by the Press *et al.* in their book (Press *et al.* 1994). The singular value decomposition of a matrix  $\mathbf{A}$  is:

$$\mathbf{A} = \mathbf{U}\mathbf{W}\mathbf{V}^T \quad (5.1)$$

and the inverse of a matrix  $\mathbf{A}$  is

$$\mathbf{A}^{-1} = \mathbf{U}\mathbf{W}^{-1}\mathbf{V}^T, \quad (5.2)$$

where  $\mathbf{W}^{-1}$  is an inverse matrix to  $\mathbf{W}$ :

$$\mathbf{W}^{-1} = \text{diag} \left( \frac{1}{w_i} \right). \quad (5.3)$$

The pseudoinverse is closely related to the SVD and the pseudoinverse matrix can be considered analogous to the inverse matrix. Pseudoinverse of a matrix  $\mathbf{W}$  is a matrix  $\mathbf{W}^I$ :

$$\mathbf{W}^I = \text{diag} (p_i), \quad (5.4)$$

where

$$\begin{aligned} p_i &= \frac{1}{w_i} & \text{for } w_i \neq 0, \\ p_i &= 0 & \text{for } w_i = 0 \end{aligned}$$

```

vel_prior    = 2;      # default (initial) value of velocities (a priori
                        # information)
vel_uncert   = 0.1;    # standard deviation of initial value of velocities
depth_prior  = 2;      # default (initial) value of depths (a priori
                        # information)
depth_uncert = 1;      # standard deviation of initial value of depths
data_uncert  = 0.1;    # standard deviation of travel time errors
min_vel      = 1.5;    # minimal velocity allowed in model (if smaller number
                        # than min_vel is encountered, then the value
                        # of vel_prior is used)
max_vel      = 6;      # maximal velocity allowed in model
min_depth    = 0.2;    # minimal depth allowed in model
max_depth    = 5;      # maximal depth allowed in model
tol          = 0.001;  # the smallest singular value allowed in SVD

```

Figure 5.6: Default values of user-adjustable parameters in `ComputeSVD.m` script

and a matrix  $\mathbf{A}^+$  is the pseudoinverse of a matrix  $\mathbf{A}$ :

$$\mathbf{A}^+ = \mathbf{U}\mathbf{W}^I\mathbf{V}^T. \quad (5.5)$$

The script solves the equations and writes computed depths, velocities and their standard deviations to files `VectX.csv`, `VectX_std.csv` and `VectXX.csv`. `VectXX.csv` file is used as an *a priori* information for next iteration. Therefore before running the inversion make sure that no file with this name is present in the REFRAC3D directory. The files `VectX.csv` and `VectXX.csv` are identical, the latter one is used only for supplying *a priori* information for successive iterations, but may also be used as a start-up point when additional iteration is desired, or for supplying more complex *a priori* information for first iteration. The file is an ASCII file with one column of floating-point numbers. These are depths of every cell of all refractors and slownesses in all cells of every refractor.

`VectX.csv` and `VectX_std.csv` contains resolved depths and slownesses, whilst the latter one also includes appropriate standard deviations. These files are read by the REFRAC3D, the nonsense resolved values (e.g. the negative ones) are deleted and replaced with the default ones and new matrix of coefficients is computed. This process is repeated until the desired number of iterations is reached. The RMS (root mean squared error) of travel times is written on the status bar and to the standard output.

The inversion process needs an *a priori* information about the geological media in order to stabilise the inversion process. However it is not much sensitive to slightly wrong values of *a priori* information. In a case of a good ray coverage, any values which make sense should be sufficient. If the user would like to change the default values, it can be done by editing appropriate lines in the `ComputeSVD.m` script. The lines defining values of important parameters are on the beginning of the file and are well commented, so defining of new values should be easily done also by the non-programmers (see Fig. 5.6).

The program comes with a sample dataset for testing. The data are from the archaeological survey of the Děvín Castle (see Chapter 2). This dataset is on the CD-ROM in the `refract3d` directory in the file `devin.csv`. It is a complete input file for the `refract3d` with the layer numbering already assigned.





---

## Conclusions

The aim of this text was to describe newly developed methods of seismic data processing.

The 3D shallow seismic refraction is a method which is currently finding its way into the routine geophysical prospection but is not commonly used yet. Currently, most of the data processing is carried out via the seismic tomography technique. However, seismic tomography, as has already been discussed, has also its limitations – the resolved velocity profiles are very smooth due to the inversion process, and the often used gradient model of the subsurface brings problems with boundary positioning. Even if the versions of tomography enabling simultaneous inversion of depths and velocities do exist, they suffer from smoothing. They work well for large-scale geological models but fail in detailed near-surface high-resolution prospection.

All these problems led us to develop a new version of well-known time-term method. The original time-term method by Scheidegger and Willmore (1957) was modified to handle lateral variations of velocities in highly heterogeneous media. The advantage of the time-term method over the tomography is in the higher resolution of depths and velocities of interfaces enabled by a simple linear inversion of data. The drawback is that the time-term method cannot handle gradient models, and hence its usage is limited to media where velocities are constant in the vertical direction in individual layers. In media with a small gradient of velocities, it still might give reasonable results, but the interpreter must be aware of possible errors in depths and velocities.

The REFRAC3D computer program, written as a part of this thesis, uses the modified time-term method to resolve the depth of the layer interfaces and lateral distribution of velocities from the set of travel time picks. Data sets from two localities, processed by means of this program, are presented here and compared with the results of conventional travel time tomography. In the case of archaeological prospection at the Děvín Castle, the time-term method yielded better results than the tomography method. The resulting depths and velocities from the time-term method were much more detailed than the velocity distribution from the tomography.

In contrast, processing of data from the measurement at the Ostaš seismic station suggested that more valuable is the velocity model from seismic tomography. The tomographical model enables studying of changes in fracture system with depth, while the time-term model shows fractures only in one horizontal plane.


These results suggest that both methods are to be used simultaneously (if possible) because they perfectly complement each other.

The S-wave identification techniques, we have developed, might be beneficial in the hydrogeology and engineering geology prospecting, where the saturation with fluids or the elastic parameters are of vital interest.

The first described method, the polarity reversals, brings, over its original version, also the possibility of distinguishing SV- and SH-waves. However, it still requires a special S-wave source. This restricts its use to short and shallow profiles in the case that horizontal hammer strikes serve as a source due to the limited energy produced by the strikes. Or, when using more powerful sources, like vibrators, the limitations are placed by the clumsy and expensive vibrators.

The second method, the filtration of S-waves based on the similarity of waveforms on the neighbouring records, might be more promising. It benefits from the fact that conventional sources of P-waves produce also a sufficient amount of S-waves. This method enables filtering out the P-waves while leaving S-waves on the records. The drawback is that the filtering is a laborious task. However, the results are better than was originally expected. In the future, this method needs extensive testing, which would lead to some attempts of at least partial automation, to ease and speed up the whole task. Currently, the filtration process is so time-consuming that it may not be acceptable for a common usage. But a significant improvement in speed can be also achieved by a graphical interactive filtering tool, with interactively changeable filtration options and a possibility to see the results for the whole dataset.





---

## List of symbols

$\alpha$  ... coefficient of absorption

$\theta$  ... critical angle

$\mu$  ... shear modulus

$\sigma$  ... Poisson's ratio

$\varphi$  ... dip of the interface

$\mathbf{C}$  ... covariance matrix

$d$  ... thickness of layer

$E$  ... Young's modulus of elasticity

$F$  ... force

$F()$  ... Fourier transform

$h$  ... depth to the interface

$t$  ... time

$v$  ... velocity





---

## Computer programs used in this work

**GMT** (Generic Mapping Tools) is a collection of tools for plotting graphs and maps. Most of the graphs and maps in this text were created by means of the GMT programs. The GMT was written by Paul Wessel and Walter Smith and is available as a source code from <http://gmt.soest.hawaii.edu/>. The target operating system is Unix.

**FAST** is a program for first arrival seismic travel time tomography. The program was written by Colin Zelt and runs under Unix operating systems. It is available as a source code from <http://www.geophysics.rice.edu/departement/faculty/zelt/fast.html>.

**Plotrefa** is a part of the SeisImager/2D Refraction Data Analysis Software by Geometrics. It enables processing of seismic refraction data by means of the travel time tomography, time-term method and reciprocal method. It is available as an executable binary for MS Windows operating systems. The trial version can be downloaded from <http://www.geometrics.com/seismographs/SeisSoft/seissoft.html>.

**PStomo\_eq** is a program for joint P- and S-wave first arrival seismic travel time tomography for control sources and local earthquakes. It was written by Ari Tryggvason and is available as a source code from <http://www.geofys.uu.se/at/software.html>. The target operating system is Unix.

**REFRACT3D** is a program for computing depths and seismic velocities of layer boundaries from 3D seismic refraction measurements by means of the modified time-term method (Section 1.4). It was written by Jan Valenta. The target platform is Linux. The program is available from the CD-ROM enclosed to this text as an executable binary as well as the source code.

**Seismic Un\*x** is a collection of tools for seismic data processing. It is focused mainly on the 2D seismic reflection method. The program is written by Cohen and Stockwell (2007) and the target platform is Unix. The program is available as a source code from <http://www.cwp.mines.edu/cwpcodes/index.html>.

**T<sub>E</sub>X** is a high quality typesetting system. It was originally designed by Donald Knuth, but number of its incarnations are available today. One of these (L<sup>A</sup>T<sub>E</sub>X) was used to typeset this text. The T<sub>E</sub>X is available for download as a source code and binaries for numerous platforms from <http://www.tug.org>.





---

## References:

- Aki, K. and Richards, P. G., 1980. *Quantitative seismology*. W. H. Freeman and Company, New York, U. S. A.
- Bates, C. R. and Phillips, D. R., 2000. Multi-component seismic surveying for near surface investigations: examples from central Wyoming and southern England, *Journal of Applied Geophysics*, 44, 257–273.
- Brož, M., 2000. Detection of the origin time and seismic ground motion of quarry blasts, *Acta Montana, ser. A*, 16 (118), 17–24.
- Cho, W. H. and Spencer, T. W., 1992. Estimation of polarization and slowness in mixed wavefields. *Geophysics*, 57, 805–814.
- Cohen, J. K. and Stockwell, Jr. J. W., 2007. CWP/SU: Seismic Un\*x Release No. 40: an open source software package for seismic research and processing, Center for Wave Phenomena, Colorado School of Mines.
- Crampin, S., 1985. Evaluation of anisotropy by shear-wave splitting, *Geophysics*, 50, 142–152.
- Crampin, S., 1999. Calculable fluid–rock interactions, *Journal of the Geological Society, London*, 156, 501–514.
- Dankbaar, J. W. M., 1985. Separation of P- and S-waves. *Geophysical Prospecting*, 33, 970–986.
- Durdík, T., 1999. *Ilustrovaná encyklopedie českých hradů*. Libri, Prague, 111–112 (in Czech).
- Flinn, E. A., 1965. Signal analysis using rectilinearity and direction of particle motion. *Proceedings of the IEEE*, 12, 1874–1876.
- Gaždová, R. and Vilhelm, J., 2006. Stanovení disperzní křivky z úderového a vibračního měření v mělkém seismickém průzkumu. Sborník vědeckých prací VŠB-TUO, Řada stavební, VŠB-Technická univerzita Ostrava, 77–88 (in Czech).
- Hagedoorn, J. G., 1959. The plus-minus method of interpreting seismic refraction sections. *Geophysical Prospecting*, 7, 158–181.

- Hearn, T. M. and Clayton, R. W., 1986. Lateral velocity variations in southern California. I. Results for the upper crust from Pg waves. *Bulletin of the Seismological Society of America*, 76, 495–509.
- Hobro, J. W. D., 1999. *Three-dimensional tomographic inversion of combined reflection and refraction seismic travel-time data*. Ph.D. Thesis, Department of Earth Sciences, University of Cambridge.  
<http://bullard.esc.cam.ac.uk/~hobro/thesis/index.html>
- Hole, J. A. 1992. Nonlinear High-Resolution Three-Dimensional Seismic Travel Time Tomography. *Journal of Geophysical Research*, 97, 6553–6562.
- Hole, J. A., Clowes, R. M. and Ellis, R. M., 1992: Interface Inversion Using Broad-side Seismic Refraction Data and Three-Dimensional Travel Time Calculations. *Journal of Geophysical Research*, 97, 3417–3429.
- Hole, J. A. and Zelt, B. C., 1995. 3-D finite difference reflection traveltimes. *Geophysical Journal International*, 121, 427–434.
- Holmes, G. M., Crampin, S. and Young, R. P., 2000. Seismic anisotropy in granite at the Underground Research Laboratory, Manitoba, *Geophysical Prospecting*, 48, 415–435.
- Kolínský, P. and Brokešová, J., 2007. The Western Bohemia Uppermost Crust Shear Wave Velocities from Love Wave Dispersion. *Journal of Seismology*, 11, 101–120.
- Kopecký, L., 1984. Základní mapa ČSSR 11-42 Manětín, Ústřední ústav geologický, Prague.
- Málek, J., Kolínský, P., Štrunc, J. and Valenta, J., 2007. Generalized average of signals (GAS) – a new method for detection of very weak waves in seismograms. *Acta Geodynamica et Geomaterialia*, Vol. 4, No. 3, 1–6.
- Palmer, D., 1980. *The Generalized Reciprocal Method of Seismic Refraction Interpretation*. Society of Exploration Geophysicists, Tulsa, Oklahoma.
- Palmer, D., 2001. A simple approach to 3D shallow refraction seismology. Extended abstract, ASEG 15<sup>th</sup> Geophysical Conference and Exhibition, August 2001, Brisbane.
- Perelberg, A. I. and Hornbostel, S. C., 1994. Applications of seismic polarization analysis. *Geophysics*, 59, 119–130.
- Press, W. H., Teukolsky, S. A., Vetterling, W. T. and Flannery, B. P., 1994. *Numerical Recipes in FORTRAN: The Art of Scientific Computing*. Cambridge University Press, second edition.
- Příkryl, R., Vilhelm, J., Lokajíček, T., Pros, Z. and Klíma, K., 2004. Correlation of field seismic refraction data with 3-D laboratory ultrasonic sounding data during exploration of a dimension stone deposit. *Journal of Applied Geophysics*, 56, 59–72.
- Ritzwoller, M. H., Shapiro, N. M., Levshin, A. L. and Leahy, G. M., 2001. Crustal and Upper mantle Structure beneath Antarctica and Surrounding Oceans. *Journal of Geophysical Research*, vol. 106, no. 12, 30645–30670.
- Richwalski, S., Roy-Chowdhury, K. and Mond, J. C., 2000. Practical aspects of wavefield separation of two component surface seismic data based on polarization and slowness estimates. *Geophysical Prospecting*, 48, 697–722.

- Samouëlian, A., Richard, G., Cousin, I., Guérin, R., Bruand, A. and Tabbagh, A., 2004. Three-dimensional crack monitoring by electrical resistivity measurement, *European Journal of Soil Science* 55, 751–762.
- Scheidegger, A. E. and Willmore, P. L., 1957. The use of a least squares method for the interpretation of data from seismic surveys. *Geophysics*, 22, 9–21.
- Schenk, V. and Růžek, B., 1981. In situ experiment on shear waves generation and determination of elastic properties of soils. *Travaux Géophysiques*, XXIX, 71–102.
- Schimmel, M., 1999. Phase Cross-Correlations: Design, Comparison and Applications. *Bulletin of the Seismological Society of America*, 89, 5, 1366–1378.
- Schimmel, M. and Gallart, J., 2003. The use of instantaneous polarization attributes for seismic signal detection and image enhancement. *Geophysical Journal International*, 155, 653–558.
- Schimmel, M. and Paulssen, H., 1997. Noise reduction and detection of weak, coherent signals through phase weighted stacks, *Geophysical Research Letters*, 130, 497–505.
- Sedláček, A., 2000. *Hrady, zámky a tvrze Království českého*, vol. 8. The first electronic edition, Jiří Čížek–ViGo agency, Prague, 295–297 (in Czech).
- Sheriff, R. E., 1984. *Encyclopedic Dictionary of Exploration Geophysics*. Second Edition. Society of Exploration Geophysics, Tulsa, Oklahoma.
- Sheriff, R. E., 1996. Understanding the Fresnel Zone. Geophysical Corner. *AAPG Explorer*, October 1996.
- Sheriff, R. E. and Geldart, L. P., 1995. *Exploration Seismology*. Second Edition. Cambridge University Press, Cambridge.
- Tabbagh, J., Samouëlian, A., Tabbagh, A. and Cousin, I., 2007. Numerical modelling of direct current electrical resistivity for the characterisation of cracks in soils, *Journal of Applied Geophysics*, 62, 313–323.
- Tarantola, A., 2005. *Inverse Problem Theory*. Society for Industrial and Applied Mathematics, Philadelphia.
- Thore, D. P. and Juliard, C., 1999. Fresnel zone effect on seismic velocity resolution. *Geophysics*, 64, 593–603.
- Tryggvason, A. and Bergman, B., 2006. A travel time reciprocity inaccuracy in the time3d finite difference algorithm by Podvin & Lecomte. *Geophysical Journal International*, 165, 432–435.
- Tryggvason, A. and Linde, N., 2006. Local earthquake (LE) tomography with joint inversion for P- and S-wave velocities using structural constraints. *Geophysical Research Letters*, 33, L07303.
- Tryggvason, A., Rögnvaldsson, S. Th. and Flovenz, Ó. G., 2002. Three-dimensional imaging of the P- and S-wave velocity structure and earthquake locations beneath Southwest Iceland. *Geophysical Journal International*, 151, 848–866.
- Turesson, A., 2007. A comparison of methods for the analysis of compressional, shear, and surface wave seismic data, and determination of the shear modulus. *Journal of Applied Geophysics*, 61, 83–91.

- Valenta, J. and Dohnal, J., 2007. 3D seismic travel time surveying – a comparison of the time-term method and tomography (an example from an archaeological site). *Journal of Applied Geophysics*, 63, 46–58.
- Valenta J. and Málek J., 2006. Anisotropy of seismic waves in the uppermost part of the Earth crust. *Acta Research Reports*, 15, 7–13.
- Vavryčuk, V., 2005. Focal mechanisms in anisotropic media. *Geophysical Journal International*, 161, 334–346.
- Vavryčuk, V., Hrubcová, A., Brož, M., Málek, J. and ALP 2002 Working Group, 2004. Azimuthal variation of Pg velocity in the Moldanubian, Czech Republic: Observations based on a multi-azimuthal common-shot experiment. *Tectonophysics*, 387, 189–203.
- Villaseñor, A., Ritzwoller, M. H., Levshin, A. L., Barmin, M. P., Engdahl, E. R., Spakman, W. and Trampert, J., 2001. Shear Velocity Structure of Central Eurasia from Inversion of Surface wave Velocities. *Physics of the Earth and Planetary Interiors*, vol. 123, 169–184.
- Yoshizawa, K. and Kennett, B. L. N., 2002. Determination of the influence zone for surface wave paths. *Geophysical Journal International*, 149, 440–453.
- Zelt, C. A. and Barton, P. J., 1998. Three dimensional seismic refraction tomography: A comparison of two methods applied to data from the Faeroe Basin. *Journal of Geophysical Research*, 103, 7187–7210.





---

# Contents

<b>Summary</b>	<b>7</b>
<b>Foreword</b>	<b>9</b>
<b>1 Processing and interpretation of shallow seismic refraction data</b>	<b>11</b>
1.1 The ray approximation and the Fresnel zone . . . . .	12
1.2 Layer-based methods of seismic refraction data processing . . . . .	13
1.2.1 Reciprocal methods . . . . .	14
1.3 Seismic tomography . . . . .	16
1.3.1 Forward modelling . . . . .	17
1.3.2 The inversion . . . . .	19
1.4 Time-term method . . . . .	21
1.4.1 Realistic or straight raypaths? . . . . .	22
<b>2 Comparison of the time-term method and tomography – a field example from the Děvín Castle</b>	<b>27</b>
2.1 History, geological and geophysical settings . . . . .	28
2.2 Data acquisition . . . . .	29
2.3 Processing of 3D data sets . . . . .	29
2.3.1 Time-term method . . . . .	30
2.3.2 Comparison of results of time-term and plus-minus methods . . .	30
2.3.3 Tomography method . . . . .	36
2.4 Archaeological interpretation . . . . .	37
2.5 Comparison of time-term method and tomography . . . . .	38
<b>3 Fracture detection with 3D seismic refraction – Ostaš Hill</b>	<b>43</b>
3.1 Study area . . . . .	44
3.2 Data acquisition and processing . . . . .	44
3.3 Interpretation . . . . .	45
3.4 Conclusion . . . . .	49
<b>4 Determination of S-waves</b>	<b>51</b>
4.1 Oriented sources – SH and SV-wave separation . . . . .	53
4.2 Generalised average for identification of S waves . . . . .	57
4.2.1 Generalised average of signals (GAS) . . . . .	58

4.2.2	Generalised average as a noise filter . . . . .	60
4.2.3	Generalised average as a wave type filter . . . . .	60
4.3	Field example – Nečtiny . . . . .	69
4.4	Conclusion . . . . .	76
<b>5</b>	<b>REFRACT3D – computer program for 3D refraction data processing</b>	<b>77</b>
5.1	REFRACT3D – User’s manual . . . . .	78
5.2	REFRACT3D – how does it work? . . . . .	80
	<b>Conclusions</b>	<b>83</b>
	<b>List of symbols</b>	<b>85</b>
	<b>Computer programs used in this work</b>	<b>87</b>
	<b>References</b>	<b>89</b>